Reconstruction of temporal variation of Asian dust provenances in silt and clay fractions in Japan Sea sediments since 10 Ma based on a quantification of each source contribution using a statistical end-member decomposition of powder X-ray diffraction profiles

（日本海堆積物の粒度別粉末 X 線回折プロファイルの統計的端成分分解に基づくアジア起源風成塵供給源別定量とその時代変化の復元）

北海道大学大学院環境科学院
地球圏科学専攻

李 梅花

Abstract

Japan sea sediments consist of various detrital materials of eolian and riverine origin. Understanding the provenance of eolian dust is vital for reconstructing the variability of wind patterns and monsoons in the past. A total of 180 samples were collected from the Hole 1425D, which had 370 m in length and 9.69 Ma geological age. Grain size separation was conducted to evaluate the mineral composition in silt (>4 μm) and clay (<4 μm) fractions by X-ray diffractometer (XRD). The mineral composition suggests the source variabilities in silt and clay fractions, which could be interpreted as provenance shifts occurring in 8 and 2.7 Ma.

Parallel factor analysis (PARAFAC) was applied to decompose X-ray diffractograms into individual subcomponents to identify the sources and quantify their contributions. A six-end-member PARAFAC model was established, and 3 Asian dust sources, Taklimakan (EM1), Gobi (EM2) and Ordos (EM5); a riverine source from the Japanese islands (EM3); and two biogenic sources, diatomaceous (EM4) and Opal-CT (EM6), were identified, and their contributions were quantified. Based on the provenance unmixing by PARAFAC, new and complete eolian accumulation rates from Taklimakan, Gobi and Ordos were reconstructed at Integrated Ocean Drilling Program (IODP) Site U1425 in the Japan Sea. In the late Miocene, the high mass accumulation rate (MAR) of riverine input from the Japan Islands reflected a strong summer monsoon during 9.7-8 Ma. Provenance shift occurred between 8 and 7 Ma from riverine source to eolian for a short period, which implied that Asian aridification was intensified at about 8 Ma, coinciding with the late Miocene cooling. Eolian flux

increased dramatically in Pleistocene to the maximum of 3.1 g/cm^2/kyr, and the Gobi Desert, Taklimakan Desert and Ordos Plateau were the three main contributors of eolian flux to the Japan Sea.

The contribution of Taklimakan source to the Japan Sea ranged from 10 to 50% and the dust flux increased gradually in the Pleistocene to the highest of 1.67 g/cm^2/kyr at 0.29 Ma. Lower flux occurred in the Late Miocene to Pliocene of <0.5 g/cm^2/kyr. MAR of Taklimakan eolian in silt fraction was generally higher than clay fraction. The contribution of Gobi dust to the Japan Sea has ranged from 20-60% since 10 Ma. The highest MAR of 1.7 g/cm^2/kyr occurred in 0.96 Ma and the lowest in Pliocene. MAR of Gobi dust in clay fraction was higher than silt fraction from 9.24 to 0.73 Ma. The results show that Taklimakan dust is dominated by the silt fraction, while Gobi dust is dominated by the clay fraction, and they are controlled by the relative contributions of different pathways of dust transport, such as the westerly winds and East Asian winter monsoon (EAWM).

Clay-size dust from the Gobi Desert increased during three periods, late Miocene global cooling (LMGC), intensification of Northern Hemisphere Glaciation (iNHG), and mid-Pleistocene Transition (MPT), which reflected increased EAWM winds associated with global cooling and glaciation. Taklimakan became the major dust contributor to the Japan Sea sediments during the warmer climate periods in the latest Miocene to early Pliocene and the Late Pleistocene, where westerly wind activity dominated eolian transport. Dust from the Ordos Plateau increased greatly from 0.95-0.85 Ma due to enhanced Asian aridification since 2 Ma in Northwest China.

Contents

List of Figure

List of Tables

List of Appendix

Chapter 1. Introduction

Dust is transported by wind as a large-scale movement of air which is sensitive to global climate changes. Eolian sedimentation in the North Pacific Ocean has been studied to evaluate the change in Earth's climate and wind circulation in the Cenozoic (e.g., LL44-GPC-3, Ocean Drilling Program (ODP) Sites 885/886 and 576/578; Leinen and Heath, 1981; Janecek, 1984). Westerlies and East Asian monsoons have prevailed in Asia since the early Miocene (Sun and Wang, 2005; Guo et al., 2008; Caves et al., 2015; Tada et al., 2016), in which East Asian summer monsoon (EASM) precipitation controls riverine detritus input to marine sediments and dust availability in desert areas, while the East Asian winter monsoon (EAWM) and westerly winds control dust transportation from Asian desert sources to marine sinks. Major climate changes in the late Cenozoic were accompanied by pronounced changes in the pattern and intensity of atmospheric circulation (Lamb and Woodroffe, 1970). An increase in ice sheets during the Northern Hemisphere Glaciation intensified the EAWM (Ding et al., 1995) in northern China. The latitudinal position of westerlies migrated equatorward by ~3-5° during the Last Glacial Maximum (Ono and Irino, 2004), while it was weakened and more poleward during the warm Pliocene (Abell et al., 2021). Currently, westerlies are migrating poleward in response to global warming (Yang et al., 2020). Accordingly, the interplay and response of atmospheric circulation to global climate changes are important factors for predicting future climate, and the reconstruction of past flux and grain size of dust accumulated in the downwind areas from inland deserts to the East

Asian region could allow us to understand the mechanisms modulating activities of westerlies and EAWM winds.

1.1 Eolian transportation paths at present

According to the 40 years of meteorological observation report in China, there are two dominant regions of dust storm events in the Central Asia deserts (Sun et al., 2001). One is the Taklimakan Desert in the Tarim Basin in western China and the other is Gobi deserts in southern Mongolia and the adjoining deserts in northern China. The two regions are under two different wind circulation systems prevailing in Eurasia (Sun 2008). In the northern Asia of Gobi and Mongolia areas, the surface wind system is mainly controlled by the pressure gradient between the Siberia-Mongolian High, which results in strong northwest winds (Winter Monsoon) in the spring season (Sun et al., 2001). Asian dust is carried by this low-level wind to a medium distance of 500-3,000 km of the Chinese Loess Plateau, Korea, Japan and SE China (Figure 1.11).

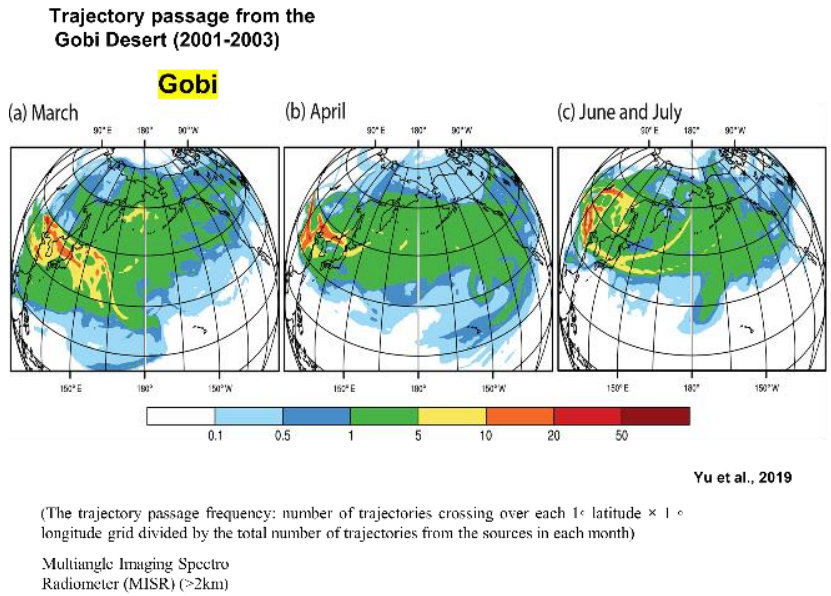

FIGURE 1.11 Trajectory passage of dust from the Gobi Desert (2001–2003) (Yu et al., 2019).

On the other hand, in the middle to high topography of Tarim and Qaidam basins, the atmospheric circulation is high-level Westerly Jet dominated (Sun et al., 2001). Westerly winds are responsible for the long-range transport dust (>5000 km) which crosses over the Japan Sea, North Pacific Ocean and America (Sun et al., 2001) (Figure 1.12). The peak of dust activation and transportation in spring over the Gobi Desert and in both spring and summer over the Taklamakan Desert.

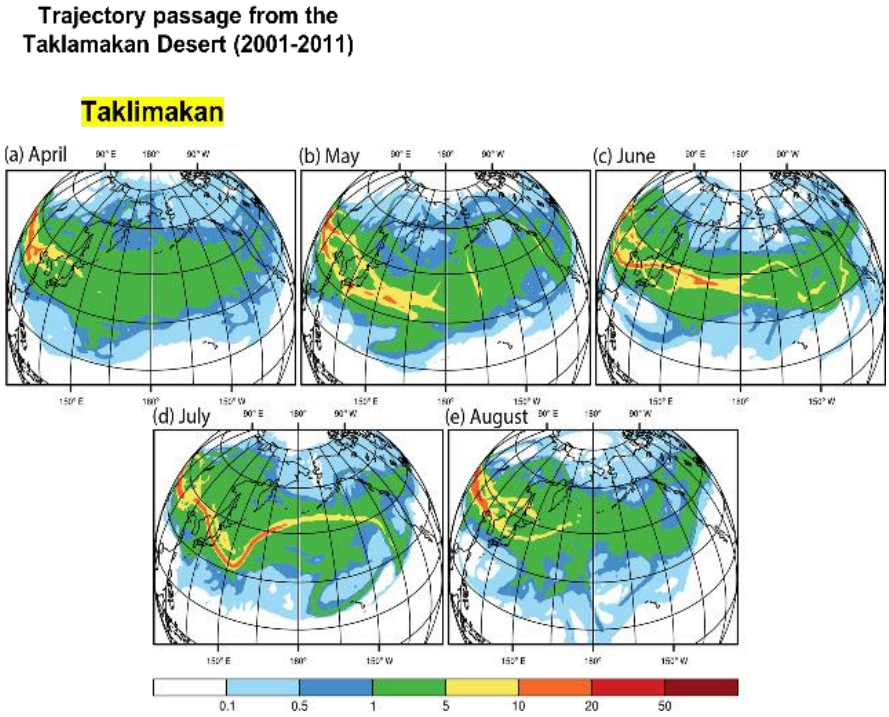

FIGURE 1.12 Trajectory passage of dust from the Taklimakan desert (2001–2003) (Yu et al., 2019).

1.2 Previous studies of eolian dust

Composition and flux of dust components could record the dust transportation mode and contribution from desert source materials, which could be well preserved in the sediments of the Japan Sea located at the eastern edge of East Asia on the main pathway of westerlies and under the influence of monsoon climate. Previous studies conducted at ODP Site 797 and IODP Site U1430 (Irino and Tada, 2000; Shen et al.,

2017; Anderson et al., 2020) in the Japan Sea presented the history of dust provenance change from the late Miocene to Quaternary. Although the relative contributions of dust to the Japan Sea sediments from different regions of Asian deserts have been intensely investigated, their association with the wind circulations of westerly, EAWM and the EASM are still poorly understood. It also remains unclear how the EASM and aridity have evolved over time in the inland deserts. The long-term aridification of inland Asia might have been associated with an uplift of the Himalayan-Tibetan complex in the Cenozoic (Guo et al., 2008; Zhang et al., 2022), while the aridity change and evolution of EASM and EAWM, as well as the latitudinal position of the westerly jet during the late Cenozoic are still controversial (Shen et al., 2017; Fan et al., 2006; Yang et al., 2017a; Yang Y. et al., 2021).

1.3 Objective

Examination of temporal and spatial variations of eolian deposits from different dust source regions could provide critical information on the response of westerlies and monsoonal fluctuations to the global climate change in late Cenozoic and the potential driving factors for these consequences, which are potentially relevant to our future climate change. Numerous Asian dust provenance studies are primarily based on the comparison of mineralogy (Leinen and Heath, 1981; Arnold et al., 1995; Biscaye, 1965) which can effectively reveal the mineral composition of parent rock in the dust sources region that controls the relative proportions of different minerals in the material carried by the wind. The mineralogical change in a specific eolian source region occurs over tens of millions of years time scale (Leinen and Heath, 1981; Prospero and Bonatti,

1969) providing a stable and significant feature to reconstruct the past atmospheric activity. Although the mineralogical composition is an effective proxy for eolian provenance study, the precise quantification of contribution from different sources is still challenging.

In this paper, we tried to solve the problems in quantification of dust contribution from different sources, their grain size dependences during the transport process, and climatic influences on dust sources and the transportation processes. For these purposes, parallel factor (PARAFAC) analysis was applied to mineral datasets in the silt and clay fractions of Japan Sea sediments to identify dust subcomponents from the complex mixture of materials, which enabled us to distinguish the variability of effects from the atmospheric circulation of westerlies, EAWM, and aridity changes in the dust source region for the last 10 million years.

Chapter 2. Site setting, stratigraphy, and sample selection

2.1 Integrated Ocean Drilling Program (IODP) Site U1425

A total of 180 samples were collected from IODP Site U1425 (39°29.44′N, 134°26.55′E) (Figure 2.11), which is situated on the terrace of the Yamato Bank in the center of the Japan Sea. The higher topographic setting of the site minimizes the influence of turbidites, and slow sedimentation is ideal for detecting eolian dust (Tada et al., 2015).

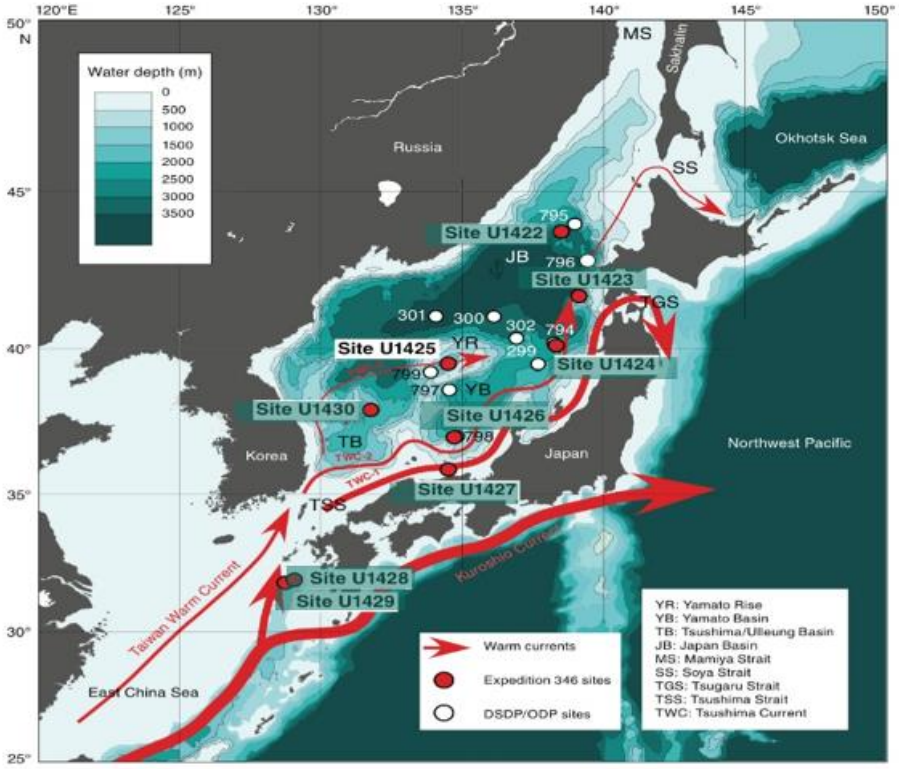

FIGURE 2.11 Location map of IODP Site U1425.

The sediment at Site U1425 is defined by three lithologic units (Tada et al., 2015). Unit I has an age from the Late Pliocene (2.7 Ma) to Holocene and consists of a higher proportion of terrigenous materials of clay and silty clay with small amounts of diatom-bearing clay. The most distinguishing sedimentary feature in this unit is the alternating bedding of dark and light intervals. Unit II has an age from the late Miocene

(7.4 Ma) to late Pliocene (2.7 Ma) and is mostly composed of a mixture of fine-grained clay minerals and biosiliceous components of diatom-rich clay, which indicates high biological productivity in this unit. Unit III, covering 7.4-9.7 Ma in this study, consists of clay, diatom-rich clay, diatom ooze, and siliceous claystone and has relatively higher terrigenous content in the sediment than Unit II. Volcaniclastic materials in this core represent a minor component of the sediments in general (Tada et al., 2015).

The age model for this site was established based on an integration of datums suggested by three age models by Tada et al. (2018), Kurokawa et al. (2019) and Kamikuri et al. (2017). From 0-1.45 Ma, we follow the age model of U1424, where the gamma-ray attenuation (GRA) density profile was tuned with LR04 (Lisiecki and Raymo, 2005), and the age was projected to U1425 using the correlation of dark-light sedimentary cycles by Tada et al. (2018). From 1.5-9.21 Ma, an age model orbitally tuned with long (405 ky) and short (100 ky) eccentricity cycles by Kurokawa et al. (2019) was used. From 9.22-9.69 Ma, biostratigraphic age controls by Kamikuri et al. (2017) were adopted (Figure 2.12).

Samples at Hole D of Site U1425 from the top to ~370 m CCSF-D_Patched_rev20170309 (revised core splice depth below sea floor; Irino et al., 2018), covering 9.6 Ma, where the average sample resolution was approximately 53 ky. Stratigraphic positions of samples collected from the interval out of the splice were projected to the corresponding stratigraphic position in Hole B by examining the core photograph. Details about the samples used, such as projected stratigraphic positions on the splice, revised core splice depth below the sea floor (m CCSF-

D_Patched_rev20170309), estimated ages, and the related sedimentation rates are shown in Table S1.

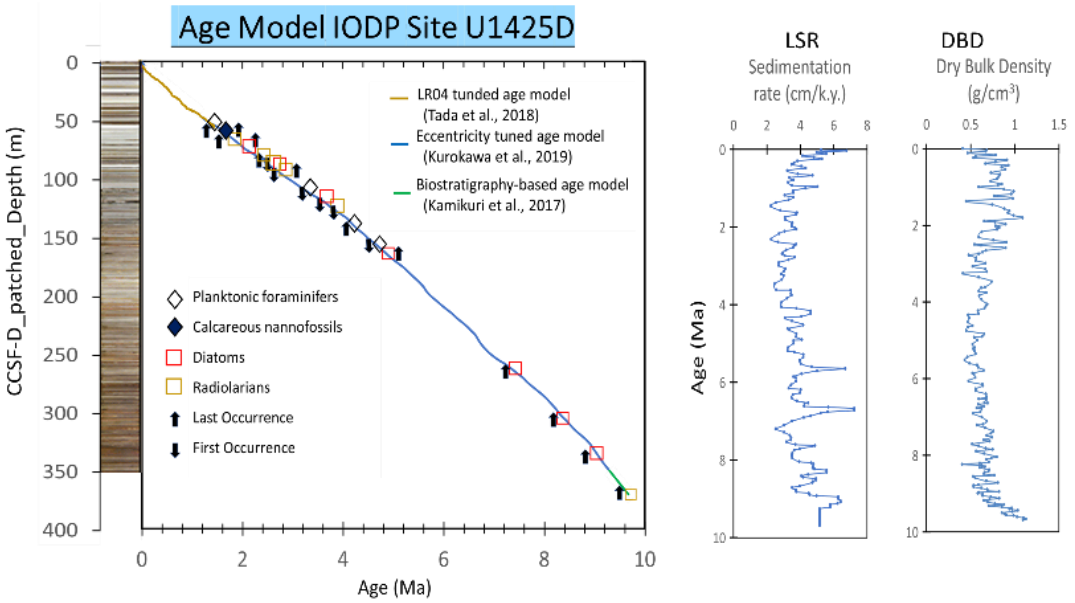

FIGURE 2.12 Age-depth relationship for the IODP Site U1425 sediment sequence. The age model for this site was established based on an integration of datums suggested by Tada et al. (2018), Kurokawa et al. (2019), and Kamikuri et al. (2017).

2.2 Potential source materials

The main sediment sources of the Japan Sea are the eolian dust from Central Asian deserts and riverine input from the nearby Japan islands (Shen et al., 2017). Asian dust is mainly emitted from the ten deserts and sandy lands in Central Asia, such as the Mongolian Gobi Desert, Gurbantuggut Desert, Taklimakan Desert, Qaidam Basin, Badain Juran Desert, Tengger Desert, Hobq Desert, and Mu Us sandy land, according to the meteorological observations (Sun et al., 2001; Wang et al., 2008). The detritus sources of these ten deserts are nearby mountains and underlying bedrock in the three major regions of the Northern Tibetan Plateau (NTP), the Central Asian Orogen (CAO), and the Ordos Plateau in North China which have been formed by tectonic activities in central to northern Eurasia since the Mesozoic (Chen et al., 2007). NTP contains Tarim

Craton and Qaidam Craton that provide clastic particles to the Taklimakan desert from the mountains of Kunlun Shan, Pamirs and Altun (Rittner et al., 2016). CAO contains the Junggar Craton and Siberian Plate, which supplied detritus to the Gobi and Mongolian deserts from the Gobi-Altai, Hangai Mountains, and Tianshan Mountains (north) (Chen et al., 2007; Sun et al., 2018). The Ordos Plateau is situated in the North China Craton delivering detrital materials to the eastern Mu Us Sandy land, Hobq Desert, and Ulan Buh Desert, although their contributions to the total Asian dust emissions are limited (Figure 2.21; Sun et al., 2018).

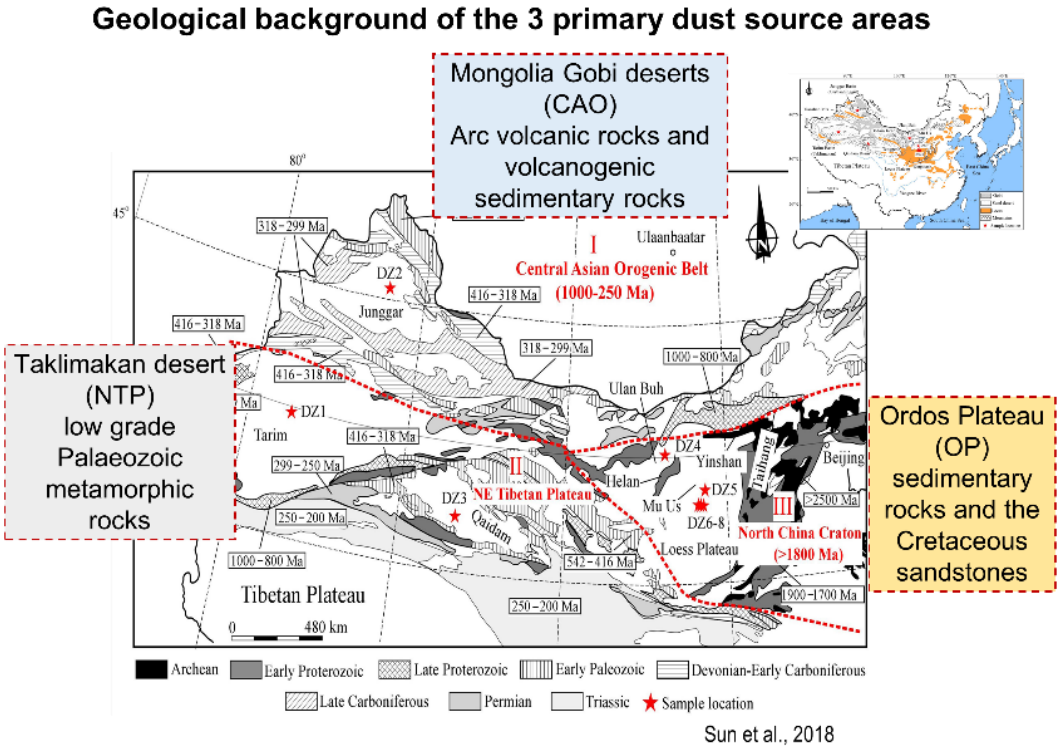

FIGURE 2.21 The three main dust source regions in the Northern Tibetan Plateau (NTP), Central Asian Orogen (CAO) and Ordos Plateau (Chen et al., 2007; Sun et al., 2018) in Central Asia and their geological background.

Despite that NTP and CAO are regional metamorphic mountain ranges, the combination of rock types and nature are different. Taklimakan desert is situated on the Tarim Craton in the NTP region, which consists of marine shale and sandstone in the

basin (Anonymous, 1991). The Tarim sandstone mainly derived from the interior of the Tarim Craton, which is dominated by monocrystalline quartz (Figure 2.22; Carroll et al., 1995). In contrast to the Tarim Basin, volcanic rocks and volcanogenic sedimentary rocks dominate in the Junggar Basin and these sandstones bear the compositional imprint of arc volcanics with felsic composition and plagioclase feldspar (Figure 2.22; Carroll et al., 1995). The East Gobi Basin was formed by extension and intracontinental rifting during the late Mesozoic, while the basement rock in southern Mongolia consists of volcanic islands with composition from lithic- and plagioclase feldspar-rich volcanic detritus to quartz and feldspar-rich granitic material (Watson et al., 1987; Johnson et al., 2001; Davidson, 2005). The distinctive features of the mineralogical composition in the two regions are inherited from the parent rocks which provide a stable and significant property for provenance study (Figure 2.22).

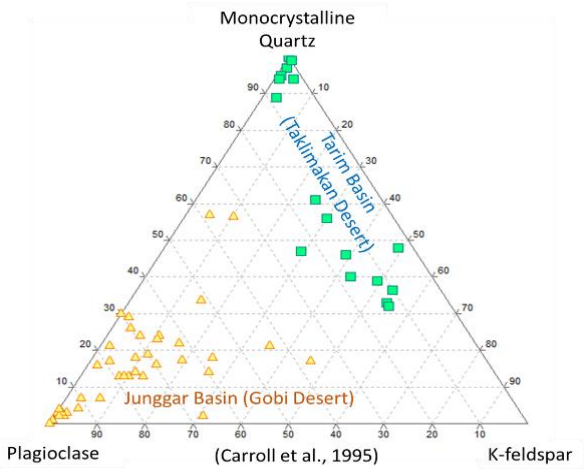

FIGURE 2.22 Ternary diagram of mineral composition of monocrystalline quartz, plagioclase and K-feldspar in the Tarim Basin and Junggar Basin (Gobi) according to Carroll et al. (1995).

Quartz, K-feldspar and muscovite are resistant to chemical weathering (Berner and Berner, 1996), while plagioclase will be partially weathered in the annual precipitation over 700 mm (Jeong et al., 2011). However, plagioclase (albite) is stable

and unchanged in the semi-arid and arid environments which rainfall is less than 500 mm. Because dust source regions in inland Asia such as Junggar Basin, Gobi, Mongolia and Tarim Basin underwent prolonged semi-arid to arid environments from the early Miocene to the present (Guo et al., 2008; Zhang et al., 2022), primary detrital minerals such as quartz, K-feldspar, and plagioclase (albite) could be altered insignificantly under such dry environment. The long-term resistivity of minerals under arid conditions well exemplified in L1 and L2 loess layers in the Chinese Loess Plateau (CLP) (Jeong et al., 2011).

To determine the provenance of the detrital end-members in U1425 sediments, we collected loess and desert materials from the three primary dust source areas of the Tarim Basin near the NTP, Tian Shan Mountains, Mongolian and Gobi Deserts in the CAO, Hobq, Inner Mongolia, and Mu Us Deserts on the Ordos Plateau (Isozaki et al., 2020; Nagashima et al., 2017; Sun et al. 2007) and neritic sediments close to the Japanese coast to serve as a riverine supply from the Japanese islands (Figure 2.23). The list of source samples from the Taklimakan Desert, Mongolian Gobi Desert, Ordos Plateau and Japanese islands is shown in Table S2.

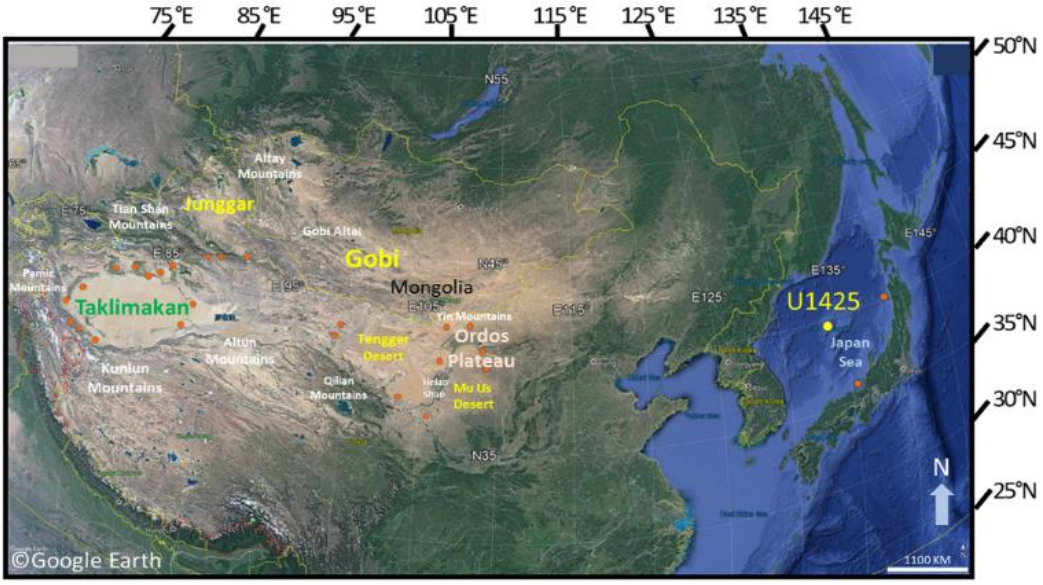

FIGURE 2.23 Sampling sites of the potential dust source materials from deserts in the three main dust source regions in the Northern Tibetan Plateau (NTP), Central Asian Orogen (CAO) and Ordos Plateau in Central Asia and neritic sediments from Japan Islands (orange dots).

Chapter 3. Analytical methods

3.1 Grain-size separation

To distinguish possible transport modes of detrital subcomponents such as westerlies, low-level wind during the winter monsoon, and river suspension and to eliminate mineralogical fractionation during sorting, it was necessary to measure compositional variability for various grain-size fractions within sediments. Nagashima et al. (2007) pointed out that eolian dust dominates the silt fraction of hemipelagic sediments in the Japan Sea, while riverine input is in the clay fraction. Therefore, we decided to separate sediment samples into different size fractions of silt (>4 μm) and clay (<4 μm). Grain-size separation was conducted by the repeated pipette method (Krumbein and Pettijohn, 1938).

3.2 Powder X-ray diffraction (XRD) Analysis

The mineral composition was analyzed for both silt (>4 μm) and clay (<4 μm) fractions, as well as potential source materials by using a powder XRD method. A powder sample mounted on a glass holder was scanned from 2° to 40° 2θ by 1° 2θ/min at 40 kV and 20 mA using CuKα radiation, where the diffraction intensity (counts per second: cps) was recorded with a 0.02° 2θ step. Identification of major and clay minerals was performed according to the position of diagnostic peaks of these minerals on the XRD diffractograms (Figure 3.21; quartz 20.8°, illite 8.8°, chlorite 25.2°, kaolinite 24.2°, smectite maximum between 5 and 8°, K-feldspar 27.5°, anorthite 27.8°, and albite 28.0°). Since the 26.6° peak of quartz may overlap strong reflection of illite,

the 20.8° peak was used as the relative measure of quartz abundance (Biscaye, 1965). The reproducibility of these measurements is better than 5%.

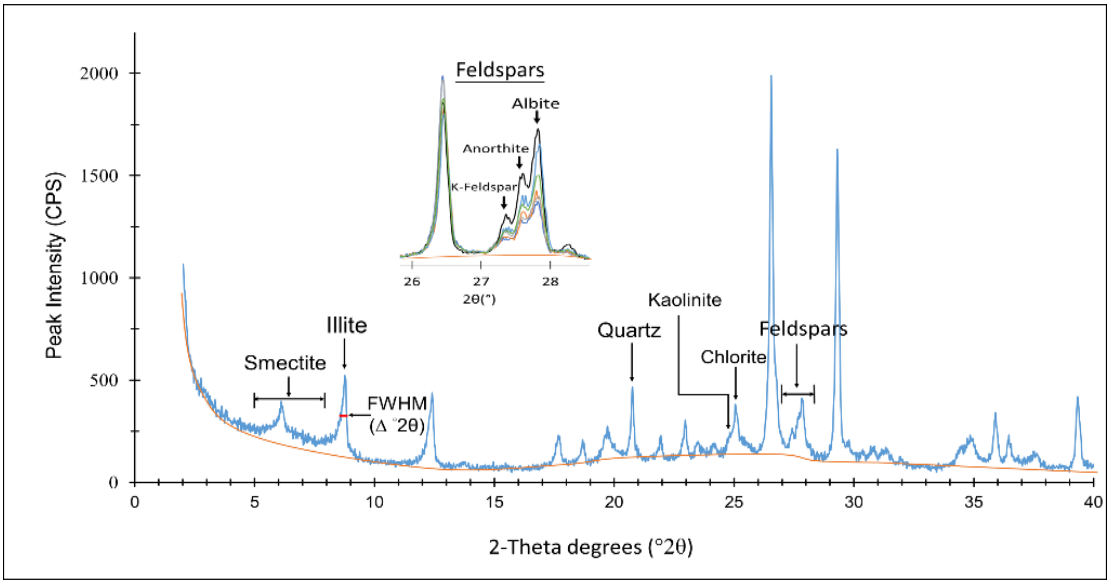

FIGURE 3.21 X-ray diffraction (XRD) spectra for a typical sample from IODP Site U1425. Identification of minerals was performed according to the position of their diagnostic peaks on the XRD diffractogram.

Illite crystallinity and illite chemical Index

Illite crystallinity and the chemical index of illite were also examined. The illite crystallinity was examined as a half-height width (FWHM) (Δ °2θ) of the 10 Å (8.8°) peak on the XRD diffractograms (Figure 3.21). This is a measure of the crystallite size of illite and is often used to trace the possible source regions in marine sediments (Petschick et al., 1996). Higher values indicate poor crystallinities, and low values indicate well-developed crystallinities (Ehrmann, 1998). According to the Kübler index (1964), the illite crystallinity value is useful to determine what type of metamorphic conditions existed when a rock was formed. The illite chemistry was inferred from the ratio of 5 Å/10 Å peak areas on the XRD diagrams. Values above 0.4 are found in Al-rich illites (muscovite) formed by strong hydrolysis, while ratios below 0.4 represent

(Fe, Mg)-rich illites (biotite) characterizing for physically eroded/unweathered rocks (Ehrmann, 1998).

3.3 Measurement of diatomaceous content

Biogenic silica content (bioSiO_2) was estimated from the calibration curve with the height of diatomaceous hump between 16 and 32.5° on the XRD diagrams (Figure 3.31 (a)). A calibration curve was prepared from known mixtures of nearly pure diatom and diatom-free sediment in varying proportions to give a series of mixtures containing 0 to 90 percent diatomaceous and the samples were X-rayed. The height of the counting from XRD with the known amount of opal in the sediment was plotted as calibration curves (Figure 3.31(b)). The amounts of diatomaceous content in silt and clay fractions were calculated by this correlation:

diatomaceous content (%) = hight of 32.5° hump (cps) – 1.6831) / 3.9661.

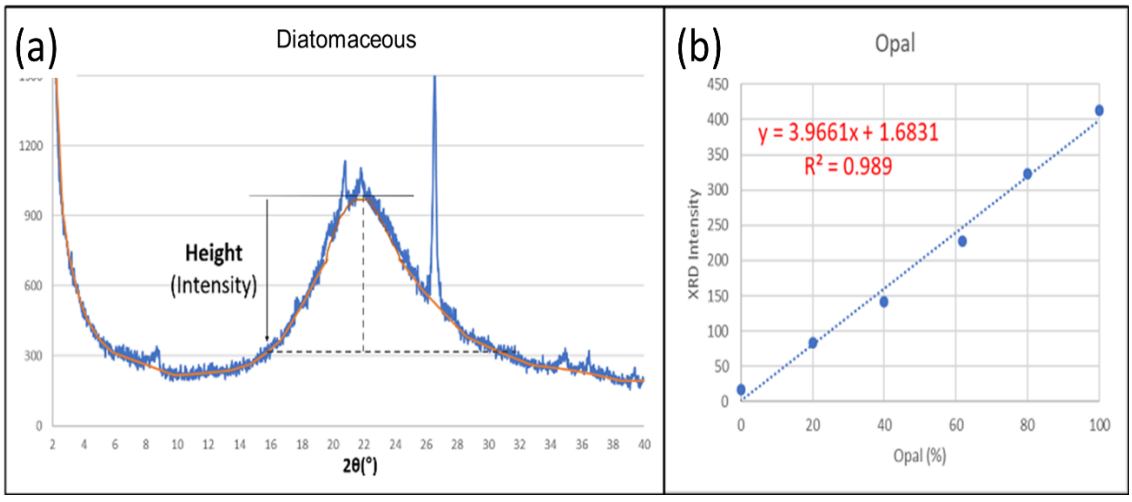

FIGURE 3.31 (a) Measurement of intensity (height) of diatomaceous content. (b) Calibration curve for determination of diatomaceous content.

3.4 Mass Accumulation Rate (MAR) Calculations

The MAR (g/cm^2/ky) for each detrital subcomponent was calculated using the dry bulk density (DBD) and linear sedimentation rate (LSR). DBD is defined as the mass (weight) of the dry solids divided by the total volume of the wet sample (Dadey et al., 1992). DBD (g/cm^3) was estimated from wet bulk density (WBD) assuming constant grain density (GD) and pore water density by Equation (1). As a measure of WBD for each sample, shipboard gamma-ray attenuation (GRA) density was used, which represented the WBD of the entire core and was measured for every 2.5 cm interval for all sediment core sequences (Tada et al., 2015). To maintain consistency between wet bulk density directly determined by shipboard "moisture and density (MAD)" measurements (Tada et al., 2015), we first calibrated GRA-based WBD (WBD_{GRA}) to MAD-based WBD (WBD_{MAD}) using a correlation between them, such as WBD_{MAD} = 0.12901 + 0.89581 * WBD_{GRA} (S.E.= ±0.10). A GD of 2.59±0.15 (g/cm^3) averaged for all MAD measurements for the U1425 samples was assumed for all samples. The pore water density was assumed to be 1.024 g/cm^3, as used in the MAD calculation (Tada et al., 2015).

$$\mathrm{DBD} = \frac{\mathrm{WBD} - 1.024}{1 - \frac{1.024}{\mathrm{GD}}} \qquad (1)$$

LSR (cm/ky) was determined from the revised core splice depth below the sea floor (m CCSF-D_Patched_rev20170309) and the integrated age model. MAR (g/cm^2/ky) of each end-member (EM) was calculated by the method of Rea and Janecek (1981) as MAR = fraction of EM * LSR * DBD.

Chapter 4. Application of parallel factor analysis (PARAFAC) to XRD diffractograms

4.1 Theoretical framework

The XRD diffractogram of each sample could be regarded as a linear combination of the diffractograms of subcomponents, such as dust from various sources, riverine input from surrounding lands, biogenic materials, and their diagenetic products. Each diffractogram of the subcomponent and its fraction in the sample should be nonnegative, and the total fraction of subcomponents should be (close to) unity. Parallel factor analysis was applied to decompose XRD diffractograms into those of subcomponents (end-members) and to quantify their contributions using drEEM toolboxes running on MATLAB® software (Murphy et al., 2013). The PARAFAC model was applied to data that were arranged in three-way arrays such as the excitation-emission matrix (EEM) of fluorescent organic matter (fluorescence intensity of sample × excitation wavelength × emission wavelength), where x_{ijk} is the intensity of fluorescence corresponding to the j-th emission wavelength and the k-th excitation wavelength for the i-th sample, and e_{ijk} is the residual representing the variability not accounted for by the model. Assuming the number of end-members is F, the decomposed matrices a_{if}, b_{jf}, and c_{kf} are the factor score (relative contribution of subcomponent in the i-th sample), factor loading spectrum along emission wavelength at a k-th excitation wavelength, and magnification factor at k-th excitation wavelength for f-th end-member, respectively, where a_{if}, b_{jf}, and c_{kf} are non-negative (Murphy et al., 2013).

$$x_{ijk} = \sum_{f=1}^{F} a_{if} b_{jf} c_{kf} + e_{ijk} \qquad (2)$$

The calculation is conducted to obtain an end-member-mixing model that minimizes e_{ijk}. In the case of XRD in this study, the dataset can be regarded as a special case with $k = 1$, where x_{ijk} is the intensity of diffraction at the j-th diffraction angle (2-40° 2θ with 0.02° 2θ interval; $1 \leq j \leq 1900$) for the i-th sample ($1 \leq i \leq 180$).

4.2 Model development

Steps included in PARAFAC analysis are to (1) import and assemble the dataset; (2) preprocess; (3) explore the data and develop preliminary models; (4) develop a final, validated model containing the correct number of components; and (5) export and interpret the results. These steps are well documented in Murphy et al. (2013). Here, the PARAFAC model development was initiated with a series of 2 to 7 components using the XRD diffractograms of the 180 samples and processing with the non-negativity constraint (which has positive values of scores and spectra) and default convergence criterion (0.01) for the outlier tests. Once the modelling constraints and criteria have been decided, the best way to obtain the best solution models for any given number of components is to repeat the modelling and ultimately adopt the model that represents the least-squares (minimum error) solution. When modelling does not produce a stable solution, indicating the model may have too many components or stricter (smaller) convergence criteria is required (Murphy et al., 2013). We applied a stricter convergence criterion of a minimum tolerance of 1×10^{-8} with nonnegativity constrained for the 4-7 components modelling (See Appendix 1). During the model development, no sample or data are removed.

4.3 Determination of the number of end-members

An appropriate model was found to minimize the sum of squares of the residuals (Bro, 1997). In this study, model development was initiated with a series of (F =) 2 to 7 end-members (EMs), which were applied to the 180 XRD profiles of silt and clay fractions with a nonnegativity constraint. Increasing the number of end-members from 2 to 7 reduced the score error and total residual sum of squares (RSS), and a significant decrease in error occurred between the 5- and 6-end-member models. As shown in Figure 4.31(a), for the silt datasets, the 4- and 5-end-member models showed higher RSS and larger score errors from 15-25%, while the 6- and 7-end-member models showed smaller score errors within 10%. On the other hand, some samples had a larger RSS in the 7-end-member model than in the 6-end-member model (Figure 4.31(a)). In the clay datasets, the 4-, 5- and 7-end-member models showed higher RSS and larger score errors than the 6-end-member model, which had the smallest RSS and score errors within 10% (Figure 4.31(b)). Therefore, 6-end-member models were adopted for both silt and clay datasets in this study.

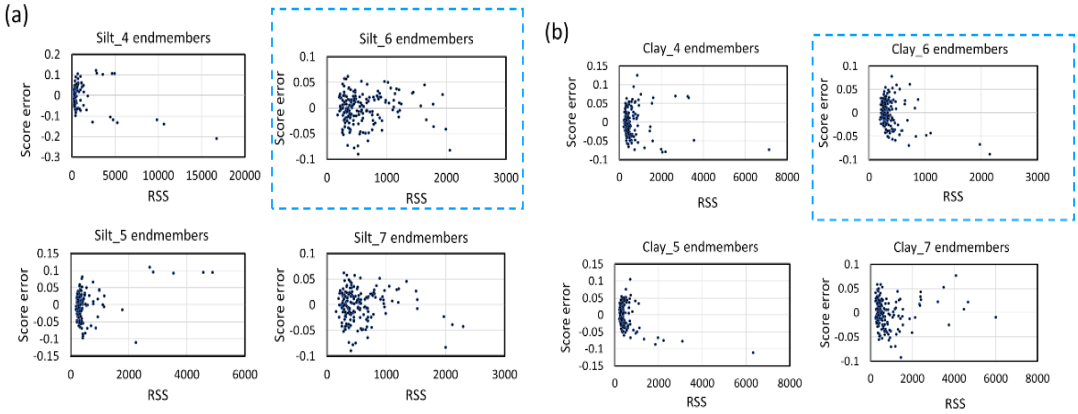

FIGURE 4.31 Residual sum of squares (RSS) and score errors of each sample in (a) silt and (b) clay datasets for the 4 to 7 end-member models calculated by PARAFAC.

4.4 Scaling factor calculations and reproducibility of end-member modelling

After validation of the 6-end-member PARAFAC model, scores (a_{if}) and spectral loadings (b_{jf}) of each end-member were obtained from the model, where c_{kf} was unity in this case (k = 1). Because the total sum of fractions of each end-member should be unity, scaling factors, α_f, were calculated to satisfy $\sum_{f=1}^{6} \alpha_f a_{if} \approx 1$ for all i, where the square sum of residual errors ($1 - \sum_{f=1}^{6} \alpha_f a_{if}$) was minimized. Using α_f, the fraction (absolute contribution) of the f-th end-member for the i-th sample was calculated as $\alpha_f a_{if}$. To obtain the XRD intensity profile of each end-member, outputs of drEEM toolboxes (Murphy et al., 2013) for spectrum loadings (b_{jf}) were first divided by the maximum of b_{jf} in terms of j for each f-th end-member, which was set as b'_{jf}. Then, b'_{jf} was divided by the scaling factor α_f to obtain a "realistic" diffractogram of each end-member.

The 6-end-member PARAFAC was modeled 20 times (Figure 4.41(a) and 4.41(b)) to ensure that the result was stabilized and not a local minimum (Stedmon and Bro, 2008). The 20 repetitions of score calculations of each end-member in the silt and clay datasets are stable and had no large variation (Figure 4.42(a) and 4.42(b)) except the Opal-CT (EM6) in the silt dataset. The content of diatomaceous (EM4) and Opal-CT (EM6) estimated from the PARAFAC Model is compared with the measured content of biogenic from XRD diffractograms at this site (Figure 4.43(a) and 4.43(b)). Both present similar content and temporal distribution.

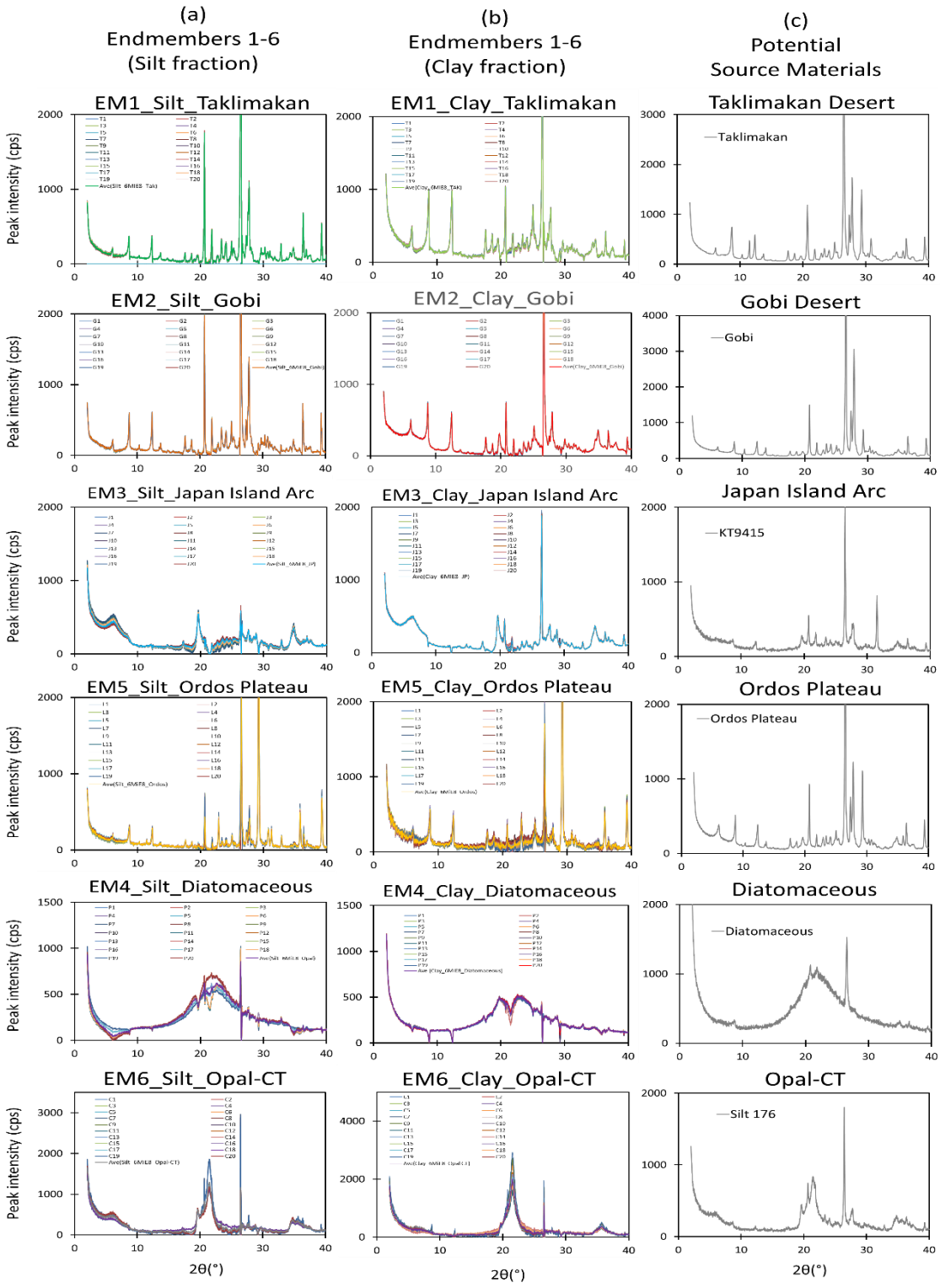

FIGURE 4.41 Summary of the 20 repetitions of spectral loading calculations and their average spectra for each end-member in the (a) silt and (b) clay datasets compared with the X-ray diffractograms of (c) potential source materials. Diffractograms for diatomite collected from the Monterey Formation in California and the sample from IODP U1425D 49H-2, 50 cm are shown as typical diatomaceous (opal-A) sediment and diagenetic form of sediment (opal-CT), respectively.

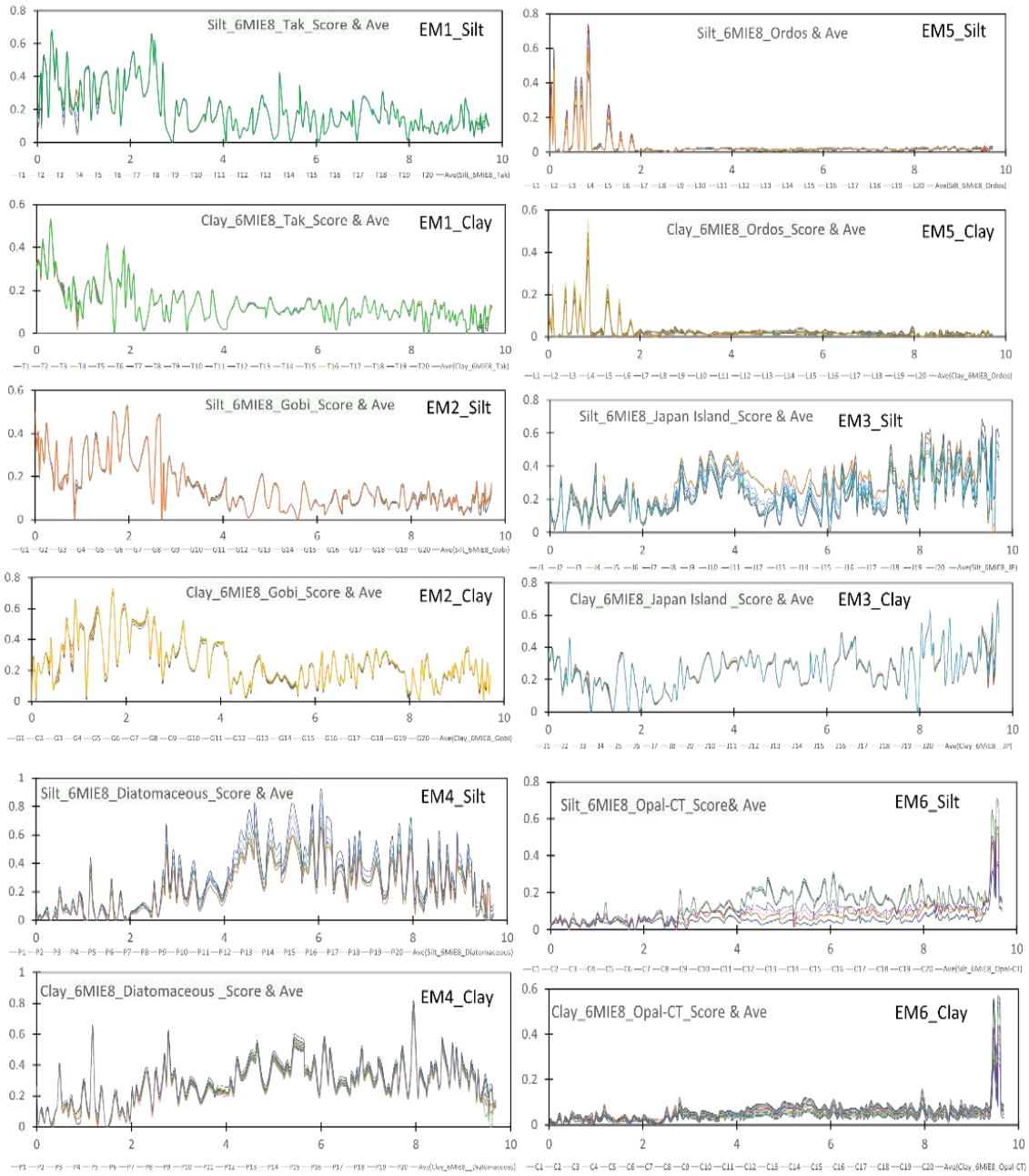

FIGURE 4.42 Summary of the 20 repetitions of score calculations and their average for each end-member in the silt and clay datasets.

Similar solutions with minor differences were reached, which implied that the obtained model was reproducible and reliable and could be used for a direct comparison between the mineral compositions of end-members and potential source materials. Therefore, the result was reported as the average of 20 models. The nonnegativity

constrained 6-end-member model explained 99.57% of the variation in silt datasets and 99.43% in clay datasets.

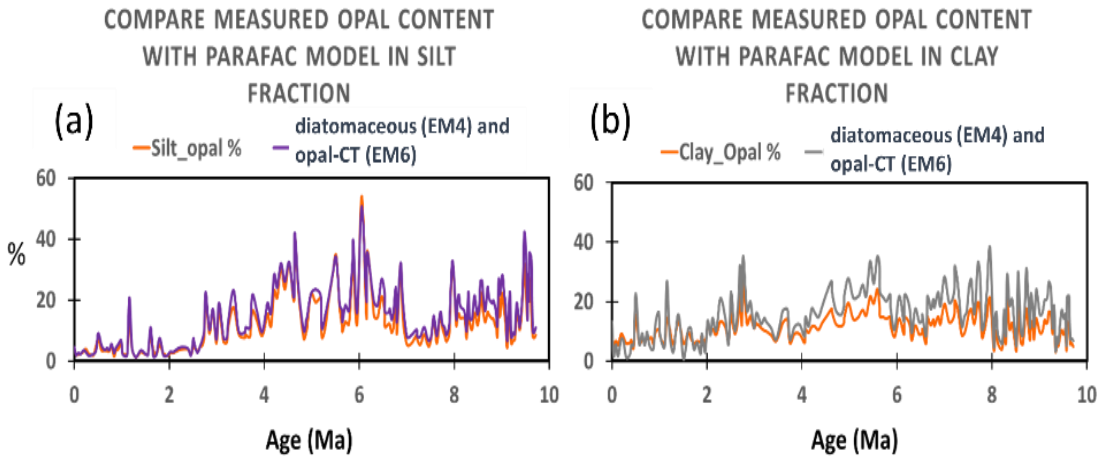

FIGURE 4.43 The total biogenic content of diatomaceous (EM4) and opal-CT (EM6) in silt and clay datasets (purple and grey line) estimated from the PARAFAC Model. They are compared with the measured diatomaceous content (orange line) in the (a) silt and (b) clay fractions.

Chapter 5. Results

5.1 Terrigenous components

The total terrigenous materials at IODP Site U1425 in Japan Sea sediments range from 25% to 82%. In general, the total terrigenous materials are low in Pliocene and higher between 8-9 Ma and after 2.7 Ma. The detrital silt fraction ranged from 3-63% and clay fraction ranged from 11 to 54%. The higher ratios of silt fraction occurred in the late Miocene during 9.6-8 Ma and lowered in 7.6-4 Ma. The higher ratios of clay fraction occurred in 7.6-6.3 Ma and after 2.5 Ma (Figure 5.11).

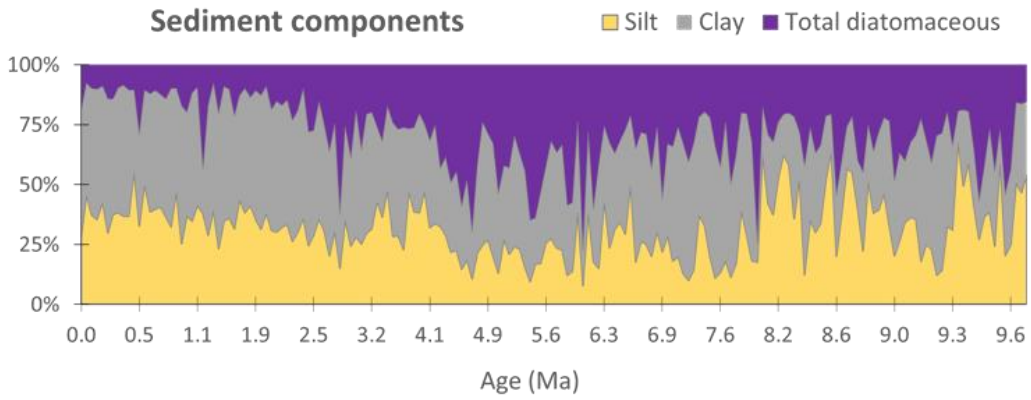

FIGURE 5.11 Temporal variation of sediment components at IODP Site U1425 in Japan Sea.

Lower contents of total terrigenous materials occurred in Pliocene which were associated with higher ratios of biogenic content. The biogenic content ranges from 6 to 68% (Figure 5.11). It is generally high in the late Miocene to Pliocene and especially high content between 5.5-4 Ma which corresponded to the higher abundance of diatoms and other siliceous components (Tada et al., 2015).

Terrigenous minerals from the IODP Site U1425 consists mainly of quartz, feldspar (including albite, anorthite and K-feldspar) and clay minerals (including illite, chlorite, kaolinite and smectite) as well as minor amounts of dolomite and pyrite.

Calcite is sparse throughout the upper 50 m of the core (mostly in the form of foraminifers and nannofossils) (Tada et al., 2015).

5.2 Mineral composition in silt and clay fractions in Japan Sea sediments

The relative content of minerals is inferred from changes in peak intensity (cps) of XRD analysis. Quartz is the most dominant mineral in sediments at this Site in Japan Sea. Quartz and feldspar are primary minerals that are related to parent rock composition.

Quartz has the highest peak intensity, ranging from 200 to 1,400 cps in silt fraction, and from 180 to 600 cps in the clay fraction. The highest quartz intensity occurred in the Pleistocene in silt fraction after 2.6 Ma to the present, and several high intensities were found during late Miocene (7Ma) to Pliocene (3Ma). The abruptly increased in quartz during the Pleistocene may indicate an abrupt increase in eolian dust as quartz is the major mineral component of Asian dust. Quartz intensity of clay fraction is stable from 200 to 400 cps and showed a gentle increase from late Miocene to the present (Figure 5.21).

Feldspars are the second most dominant mineral at this site. Albite and anorthite are the end-members of plagioclase feldspar. Albite is relatively common and important rock-forming mineral associated with the more acid rock type. Albite intensity varied between 100 and 1000 cps in the silt fraction, and below 400 cps in the clay fraction. The temporal distribution of intensity of albite in the silt and clay fractions is similar to quartz (Figure 5.21). Anorthite is a comparatively rare mineral but occurs in the basic

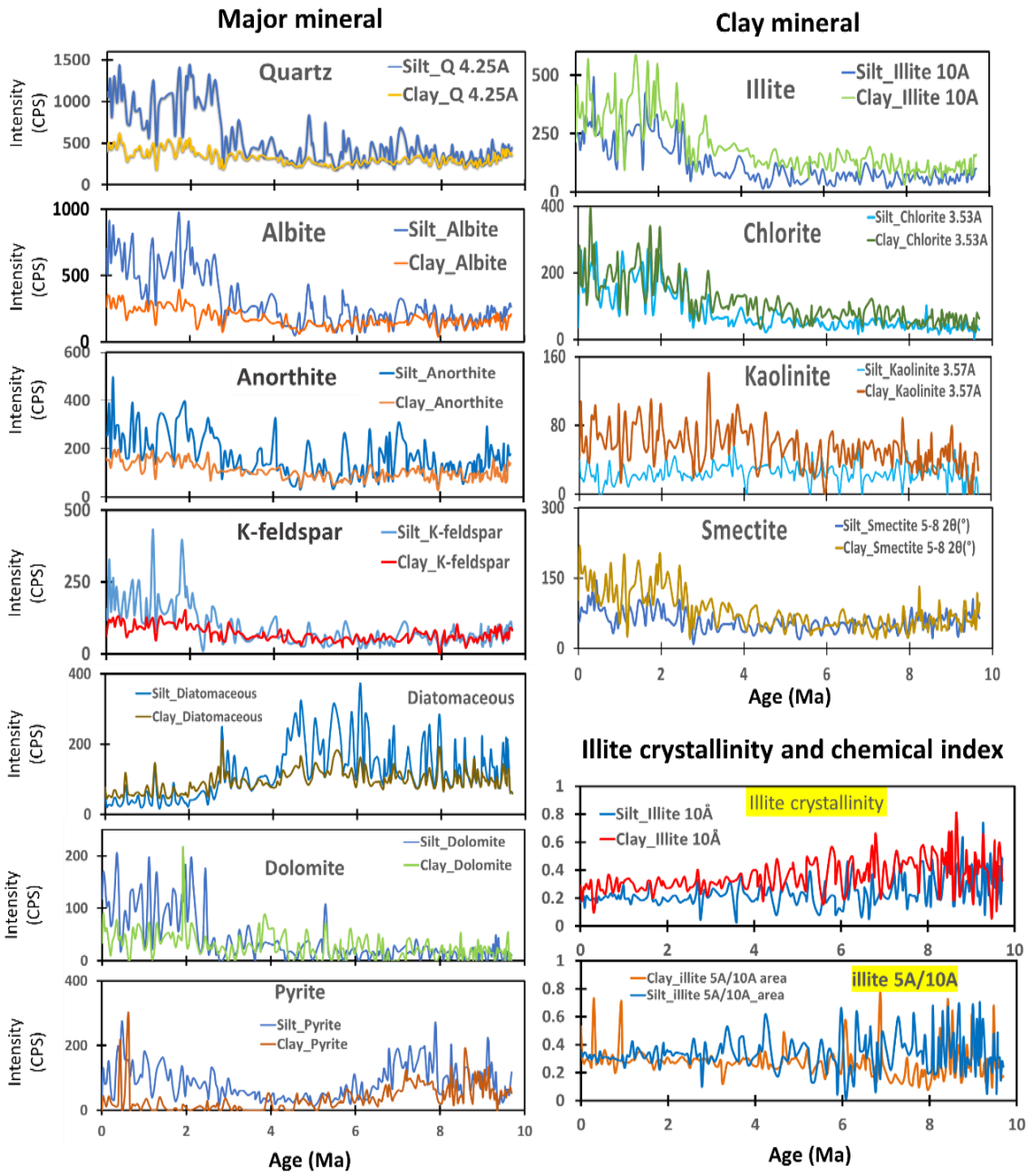

FIGURE 5.21 The temporal variability of mineral abundances of major and clay minerals in silt and clay sediments at IODP Site U1425 in the Japan Sea. Illite crystallinity and chemical index are also plotted with age in the silt and clay fractions.

plutonic rocks of some orogenic calcium-alkaline suites. Anorthite intensity varied between 50 and 500 cps in silt fraction and below 200 cps in clay fraction. In general, quartz and feldspars show higher intensity in the silt fraction than the clay fraction from the late Miocene to the Pleistocene (Figure 5.21).

Potassium-Feldspar (K-feldspar) is another end-member of alkali feldspar minerals which is a common constituent of most granites and other felsic igneous rocks. K-feldspar in silt fraction also showed ab abrupt increase during Pleistocene after 2.1 Ma. Then intensity of K-feldspar in the silt and clay fractions is similar before 7.2 Ma, but slightly increased in the silt fraction since 7 Ma and reached the highest in the Pleistocene (Figure 5.21).

Illite is a ubiquitous terrigenous weathering product, generally associated with cool, dry environments and it is the dominant clay mineral in the Chinese Loess (Sun 2011). Illite is the third most dominant mineral at the site, with the intensity >500 cps during the Pleistocene in the clay fraction. Chlorite is usually indicating the mechanical weathering of terrigenous sediments. The peak intensity of chlorite in the silt and clay fractions are below 400 counts. The temporal distribution of illite and chlorite shows similar pattern in silt and clay fractions. In general, the peak intensity of clay fraction is higher than in the silt faction and both increased abruptly at 3.1 Ma. Illite and chlorite show the highest intensity in the Pleistocene (Figure 5.21).

Kaolinite is a terrigenous weathering product usually associated with strong hydrolysis. The peak intensity of kaolinite in silt and clay fractions are generally low, below 140 cps. The downcore variation of kaolinite is different between silt and clay fractions. The peak intensity of kaolinite in silt fraction is around 50 cps between Miocene to the Pleistocene, while that in clay fraction increased gradually from Miocene to the Pleistocene with a sudden peak at 3.2 Ma with 141 cps (Figure 5.21).

Smectite is produced by continental weathering processes, weathering of volcanogenic material, and authigenic formation in sediments. The peak intensity of smectite in the silt and clay fractions are generally low from 10-100 before Pleistocene and increase to 150 cps after 2.7 Ma (Figure 5.21).

Other minerals composition at Site U1425 in Japan Sea

Authigenic components are oceanic inorganic minerals that precipitate directly from the seawater, for example, dolomite, calcite and pyrite. Dolomite is a common rock-forming mineral. It is similar to the most common carbonate mineral calcite. These two share some similarities in structure and are very closely related chemically. Calcite is chemically $CaCO_3$ (calcium carbonate), dolomite is $CaMg(CO_3)_2$ (calcium-magnesium carbonate). Dolomite intensity is low in the late Miocene to the Pliocene and increases to 200 cps after 2.7 Ma. Pyrite is the most abundant and widespread sulfide mineral (FeS_2) and its relative content in the Japan Sea is high (200 cps) in the late Miocene and the Pleistocene, but low in the Pliocene (Figure 5.21).

Illite crystallinity and Chemistry Index

The illite chemistry index in the silt fraction varies between 0.02 and 0.7, with an average of 0.33. In general, the silt fraction showed a narrow range of the value of 0.3 during the Pleistocene and the very low value of <0.1 was found in some samples during 9.6-9.3 Ma, 6.7-5.9 Ma, and at 2.7 Ma. The illite chemistry index in the clay fraction varies between 0.08 and 0.78, with an average of 0.27, and showed a lower value (<0.3) in some samples during 8-7 Ma and 4.5-1 Ma (Figure 5.21). According to the illite chemistry index, values below 0.4 represent (Fe, Mg)-rich illites (biotite) characterized

for physically eroded and unweathered rocks. The highly crystallized illite and Fe-Mg rich illite in silt fraction at Site U1425 in Japan Sea may be eolian origin (Figure 5.21).

The crystallinity of illite in the silt and clay fraction varies between 0.05–0.74° 2θ and 0.1–0.8° 2θ with average values of about 0.25 and 0.36° 2θ, respectively. The illite crystallinity of the silt fraction showed a lower and narrow range after the Pleistocene with the value of ~0.2° 2θ, while the clay fraction showed a higher value of ~0.3° 2θ during the same period (Figure 5.21). High values indicate poor crystallinities and low values indicate well-developed crystallinities. The very low values of crystallinity were found in some silt fractions at 9.3 Ma and between 6.6 Ma and 2.7 Ma with the value of <0.1◦ 2θ. The highly crystallized nature indicates the illite was not formed at surface temperature and may have originated from a low-temperature metamorphic environment. According to the Kübler index, the illite crystallinity values of <0.25° 2θ range correspond to the metamorphic greenschist facies that formed under the lowest temperatures and pressures usually produced by regional metamorphism (Figure 5.21).

Sources variability of silt and clay fractions

The illite/Quartz (Q), chlorite/Q and kaolinite/Q in silt and clay fractions show different fluctuation patterns. It is possible that the sources of these minerals are different between silt and clay fractions. The difference from 8 Ma where the two fractions show gradual change and the greatest difference occurred at 2.9 Ma (Figure 5.22(a)). The feldspars composition in the clay fraction shows more orthoclase, while the silt fraction contains more anorthite. Anorthite/Albite (An/Ab) range in the clay fraction is narrow from 0.4 to 0.6, while silt fraction shows a wider range from 0.2 to 1

which shows the highest value in the late Miocene and lower values in the Pleistocene and Pliocene. It indicates progressive changes in dust source areas or climatic (erosional) environments (Figure 5.22(b)).

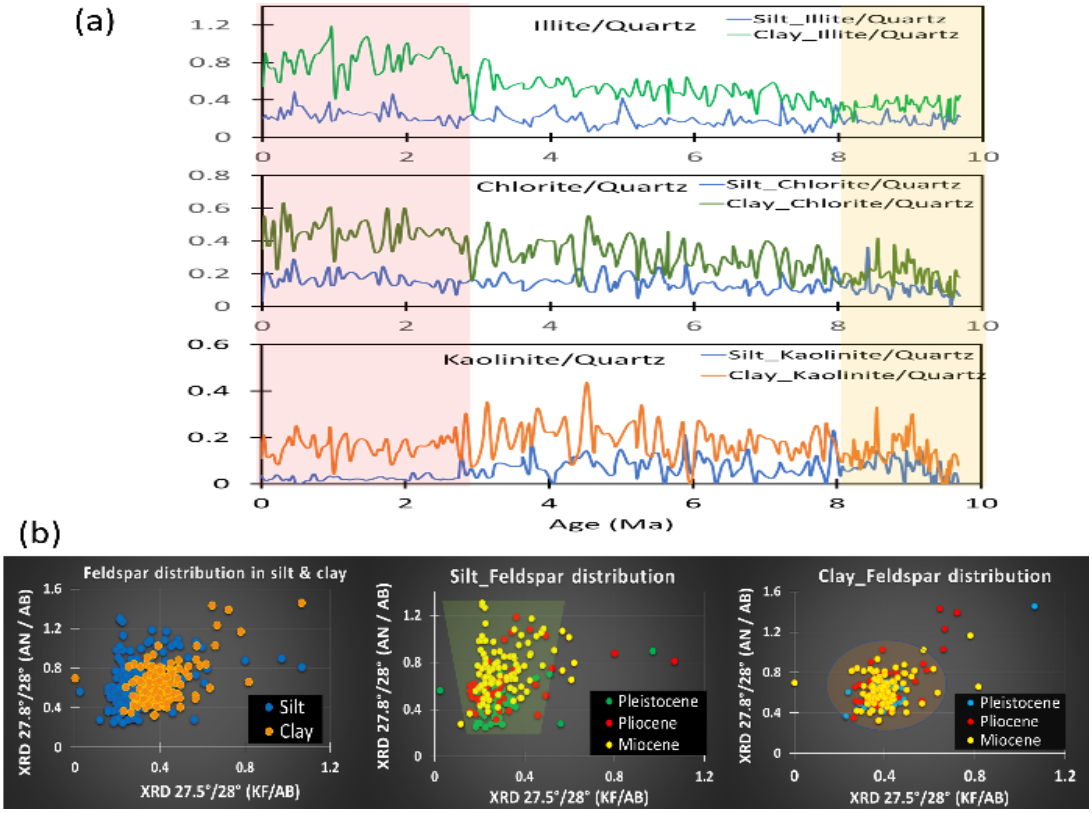

FIGURE 5.22(a) The illite/Quartz (Q), chlorite/Q and kaolinite/Q in silt and clay fractions. Shadings show the sudden increase of the difference between sit and clay fractions in 8Ma and 2.7 Ma. (b) The distribution of feldspar composition in silt and clay fractions. Silt fraction shows a progressive change of dust source areas or climatic (erosional) environments. AN/AB —Anorthite/Albite; KF/AB —K-feldspar/Albite.

Differentiation of Asian eolian and Japanese riverine sources

Quartz, plagioclase and illite were the most abundant minerals in the silt fraction during the Pleistocene, suggesting many dust-derived materials in this period (Table S3). The half-height width (FWHM) of illite in the silt fraction was low (high crystallinity) with a narrow range of approximately 0.2 Δ°2θ in the Pleistocene. According to the Kubler Index (1964), highly crystallized illite (FWHM <0.25) was sourced from regional metamorphic rocks in mountain ranges, such as those on the

northern Tibetan Plateau (NTP) or in the Central Asian Orogen (CAO). Poor illite crystallinity (FWHM >0.4) corresponded to diagenetic rock sources, such as those in the Japan Island arc.

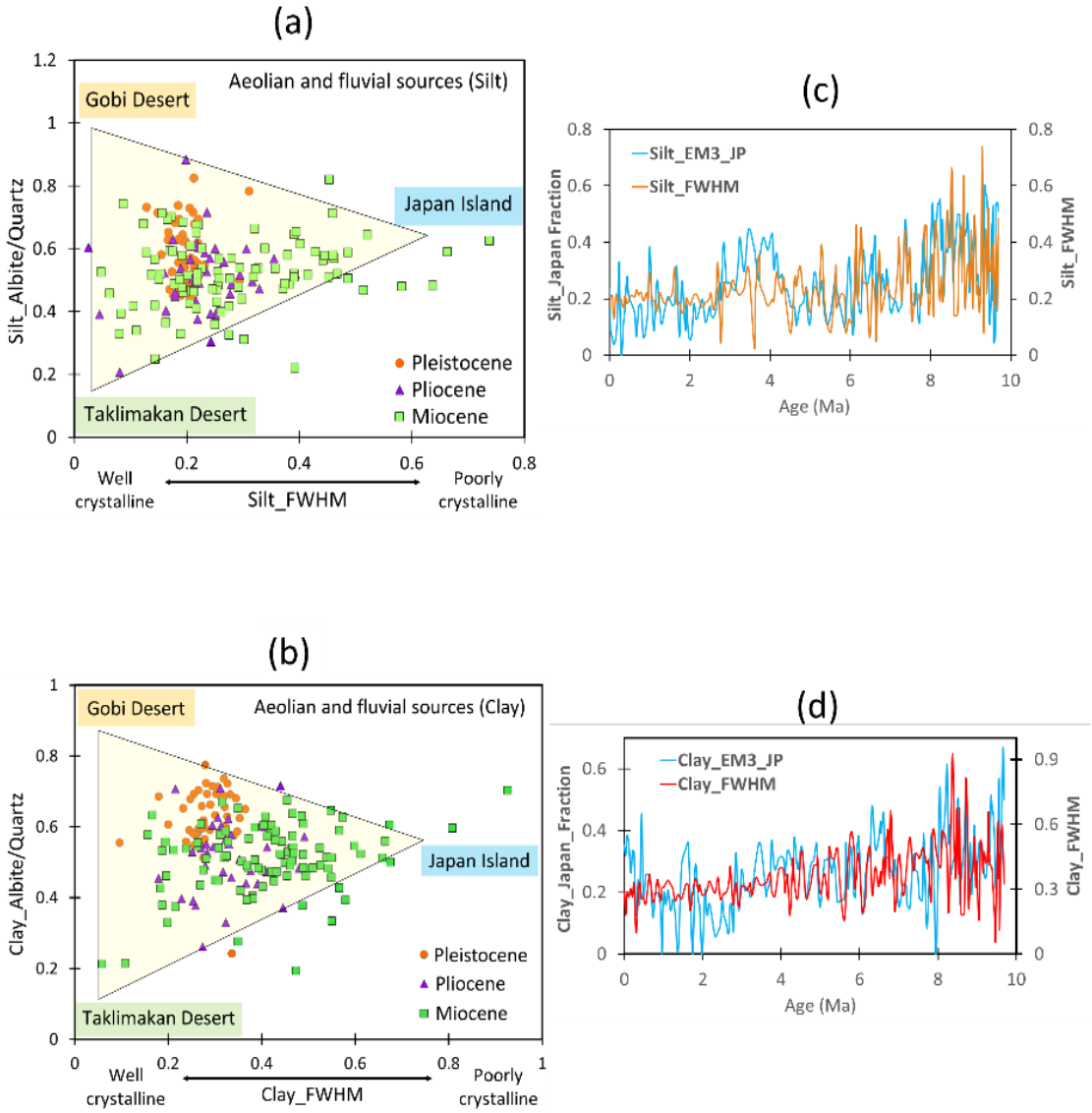

FIGURE 5.23 Differentiation of Asian eolian and Japanese riverine sources based on albite/quartz ratios and illite crystallinity (FWHM values) distributions in (a) silt and (b) clay fractions. Temporal variation of illite crystallinity compared with the contribution of EM3 (Japan Island arc origin) estimated by PARAFAC modelling in the (c) silt and (d) clay fractions.

Based on the mineralogical differences in the Tarim Basin (higher quartz content) and Junggar Basin in the Gobi Desert (higher plagioclase content) (Carroll et al., 1995 [33]) mentioned in above Section 2.2 (Figure 5.23), the distribution of albite (Ab) and

quartz (Q) ratios and illite crystallinity (FWHM) could effectively differentiate dust and riverine sources in silt and clay sediments in the Japan Sea. Taklimakan eolian sediment had the lowest FWHM values and the lowest Ab/Q ratios, and Gobi dust had a low FWHM but a higher Ab/Q ratio. Japanese riverine sediment had the highest FWHM values and higher Ab/Q ratios (Figure 5.23(a)). These interpretations are also applicable to the clay fraction (Figure 5.23(b)). This preliminary identification of the 3 sources is not sufficiently quantitative because of a lack of knowledge about exact mineral ratios for each detrital subcomponent and difficulty in eliminating contributions from biological components. Therefore, the results of more quantitative statistical end-member unmixing by parallel factor analysis (PARAFAC) are examined in the next section.

5.3 Provenance assessment of PARAFAC end-members

To determine the provenance of the 6 EMs in U1425 sediments calculated by PARAFAC, firstly we compared the diffractogram patterns of EMs with those of potential source materials. Figure 4.41 shows that desert source materials from the Taklimakan Desert, Gobi deserts and Ordos Plateau had high intensities of quartz, feldspar, and illite which match well with EM1, EM2, and EM5. Then, characteristic mineral ratios such as Ab/Q and K-felspar (K-fel) /Ab were used to distinguish the source materials (Figure 5.31(a) and 5.31(b)). Namely, Gobi and Ordos dust sources are characterized by higher Ab/Q, while Taklimakan shows lower Ab/Q (Figure 5.31(a)). On the other hand, Ordos materials are characterized by higher K-fel/Ab (Figure 5.31(b)).

Taklimakan materials and EM1 had lower Ab/Q ratios than Gobi materials and EM2 (Figure 5.31(a)). Sandstone in the Tarim Basin is dominated by monocrystalline quartz, which was a typical continental block-recycled orogen provenance of Paleozoic metamorphic rocks in the NTP (Carroll et al., 1995; Jia et al., 1997; Wang et al., 1986), while the Mongolian Gobi is characterized by back-arc basin deposits with plagioclase, feldspar-rich, volcanic detritus (Carroll et al., 1995, Davidson, 2005). Ordos materials and EM5 had high K-fel/Ab ratios (Figure 5.31(b)). The Ordos Plateau is situated in the northern part of the North China Craton, which contains largely undisturbed sedimentary rocks that are Carboniferous to Jurassic in age and Cretaceous sandstones (Kusky and Li, 2003). Therefore, we could attribute EM1, EM2, and EM5 to Taklimakan, Gobi, and Ordos, respectively. Again, it was also confirmed that EM1, EM2 and EM5 exhibited similar XRD diffractogram patterns to those of the desert materials from Taklimakan, Gobi, and Ordos, respectively (Figure 4.41).

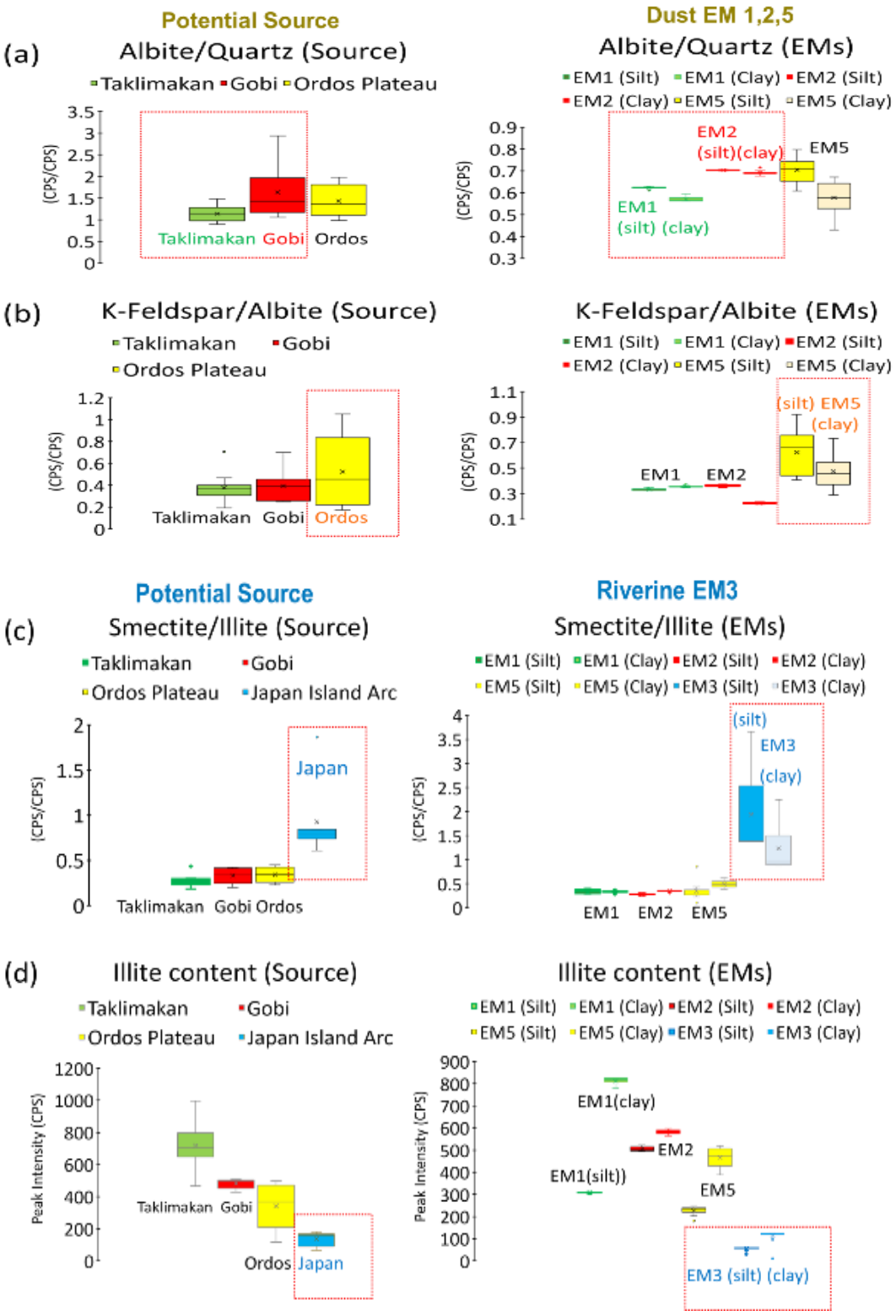

FIGURE 5.31 Summary of the mineral composition of source materials and end-members. Dust source materials from Taklimakan, Gobi and Ordos are compared with EM1, EM2 and EM5 for (a) albite/quartz and (b) K-feldspar/albite ratios. Japanese source materials are compared with EM3 for (c) smectite/illite and (d) illite contents.

Japanese island materials and EM3 had XRD diffractogram patterns different from those of the Asian dust sources and revealed significant peaks of smectite, low illite intensities (Figure 5.31(c) and 5.31(d)) and high anorthite/albite ratios. The Japanese islands are characterized by basaltic volcanic and sedimentary rocks (Nakada et al., 2016). Volcanic rocks often produce smectite by chemical weathering under wet and humid environments on Japanese islands (Liu et al., 2009). An attribution of EM3 to Japanese Island materials could be also justified by the similar temporal variations of illite FWHM and EM3 contribution (Figure 5.31(c) and 5.31(d)). Larger illite FWHM (low crystallinity) is generally associated with higher contribution of EM3 and both profiles show similar trend and critical changes at 8, 6, and 2.7 Ma both for silt and clay fractions. EM4 and EM6 were attributed to biogenic opal and opal-CT subcomponents, respectively (Figure 4.41).

5.4 Contributions and fluxes of end-members

A six-end-member PARAFAC model was established, and 3 Asian dust sources, Taklimakan (EM1), Gobi (EM2) and Ordos (EM5); a riverine source from the Japanese islands (EM3); and two biogenic sources, diatomaceous (EM4) and Opal-CT (EM6), were identified, and their contributions were quantified (Figure 5.41 and Table S4). Sediments at IODP Site U1425 in the Japan Sea indicate that biogenic blooms (EM4+EM6) occurred from the late Miocene to Pliocene. The contribution of Asian dust (EM1+EM2+EM5) to the Japan Sea was low in the late Miocene to Pliocene, at 20-40% (Figure 5.42(b)), and the mass accumulation rate (MAR) ranged from 0.2 to 1.5 g/cm^2/ky but increased dramatically to 70% in the Pleistocene, with a maximum

MAR of 3.1 g/cm^2/ky 0.03 Ma (Figure 5.43(a)). The total Asian dust MAR in this study is similar to previous estimations of 1-3 g/cm^2/ky at ODP Site 797 (Irino and Tada, 2000) and 2-3 g/cm^2/ky at MD01-2407 (Nagashima et al., 2007) in the Japan Sea and is also consistent with the exponential decreasing trend along the eastward transportation of Asian dust (Zhang et al., 2016) during the late Quaternary.

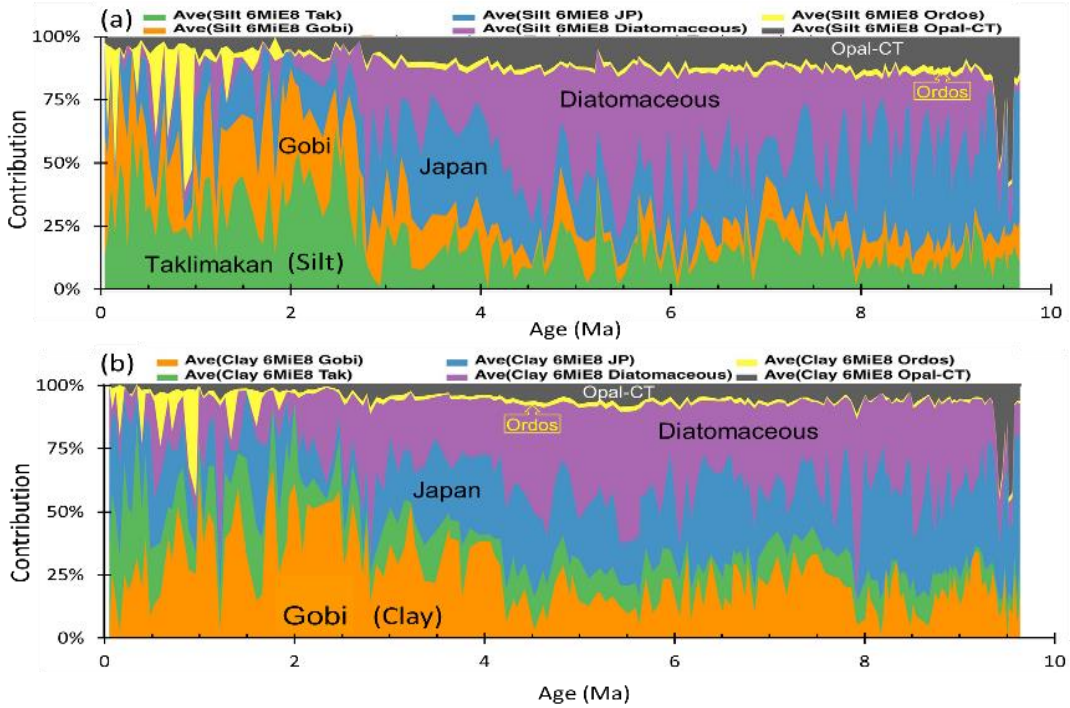

FIGURE 5.41 Temporal variation in the contribution of end-members 1-6 in (a) silt and (b) clay fractions at IODP Site U1425 in the Japan Sea. Green: Taklimakan (EM1), orange: Gobi (EM2), blue: Japanese islands (EM3), yellow: Ordos (EM5), purple: Diatomaceous (EM4), and gray: Opal-CT (EM6).

Taklimakan Desert (TAK: EM1)

The contribution of Taklimakan dust to the Japan Sea ranged from 10-50% (Figure 5.41(a) and 5.41(b)), and the flux increased gradually in the Pleistocene to a maximum of 1.67 g/cm^2/ky at 0.29 Ma, in which both silt and clay fractions had the highest MAR at the same time (Figure 5.43(b) and 5.43(d)). TAK became the main dust contributor to the Japan Sea from 0.5 to 0.16 Ma and 5.6-4 Ma (Figure 5.42(a)). Lower flux

occurred in the late Miocene to Pliocene at <0.5 g/cm^2/ky. The temporal distribution of the Taklimakan dust flux in the silt and clay fractions had a similar trend and maintained a regular ratio between them from the late Miocene to the present, although the silt fraction dominated the total Taklimakan dust fractions (Figure 5.43(d)), which implies that both silt and clay dust were transported at the same time by the same transportation mode of wind.

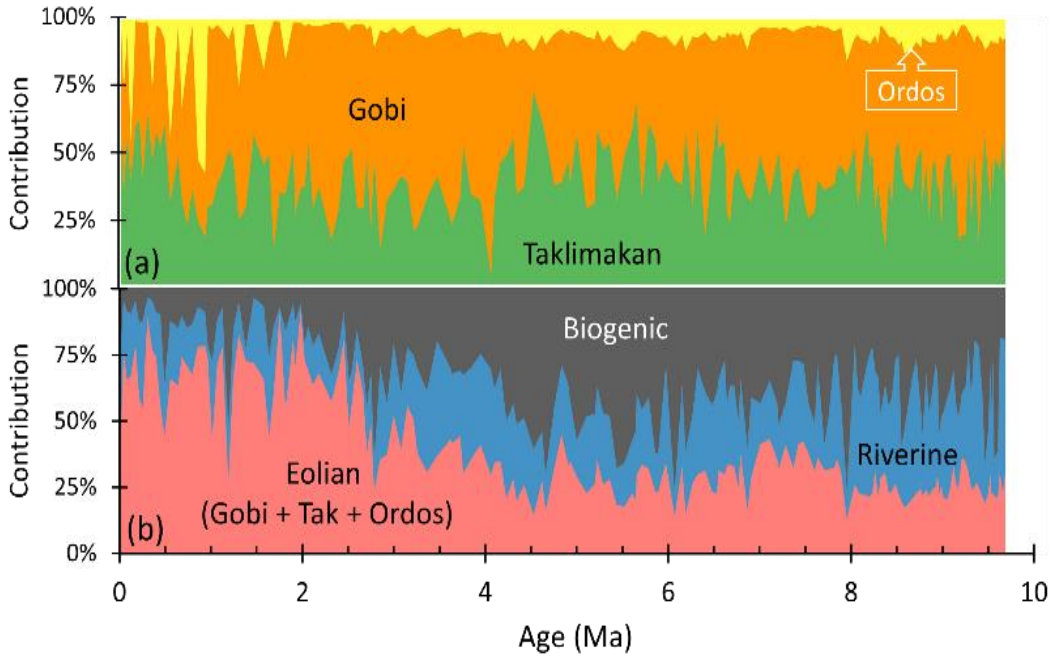

FIGURE 5.42 Relative contribution of end-members (EMs) in sediments at IDOP Site U1425 in the Japan Sea normalized for (a) total Asian dust, including Taklimakan (EM1), Gobi (EM2) and Ordos (EM5), and (b) total sediment subcomponents, including eolian (EM1, EM2, and EM5), riverine (EM3), and biogenic (EM4 and EM6) sediment subcomponents.

Gobi Desert (Gobi: EM2)

The contributions of Gobi dust to the Japan Sea have ranged from 20-50% since 10 Ma (Figure 5.41(a) and 5.41(b)). The highest MAR occurred 0.96 Ma at 1.7 g/cm^2/ky and was the lowest in the Pliocene (Figure 5.43(b)). The clay-sized Gobi dust had a higher flux than the silt-sized fraction from 9.24 to 0.73 Ma. The highest MAR in the clay fraction was 1.56 g/cm^2/ky in 0.96 Ma. The MAR of the silt fraction was

generally low at <0.8 g/cm^2/ky. The temporal variation in Gobi fluxes in silt and clay fractions showed a great difference in pattern and trend, as well as dust quantity (Figure 5.43(c)), which implied that both were transported by different wind circulation from a dust source area to the Japan Sea.

Ordos Plateau (Ordos: EM5)

Ordos dust to the Japan Sea has been significant in the Pleistocene since 2 Ma with a 10-40% contribution (Figure 5.41(a) and 5.41(b)). The highest MAR occurred 0.92 Ma with 1.26 g/cm^2/ky and decreased to 0.83 g/cm^2/ky in the Holocene (Figure 5.43(b)). The silt fraction was dominant with Ordos dust since 1 Ma (Figure 5.43(e)).

Japan Island Arc (Japan: EM3)

The contribution of riverine input from Japanese islands to the Japan Sea was high during the late Miocene at 30-50% and decreased significantly in the Pleistocene (Figure 5.42(b)). The highest MAR was 2.98 g/cm^2/ky, occurring 9.66 Ma but decreased to 0.2-1.2 g/cm^2/ky from 8 Ma to the present, showing minima 8-7, 6-4.5, 2.7-2 and 1.5-0.6 Ma (Figure 5.43(a)).

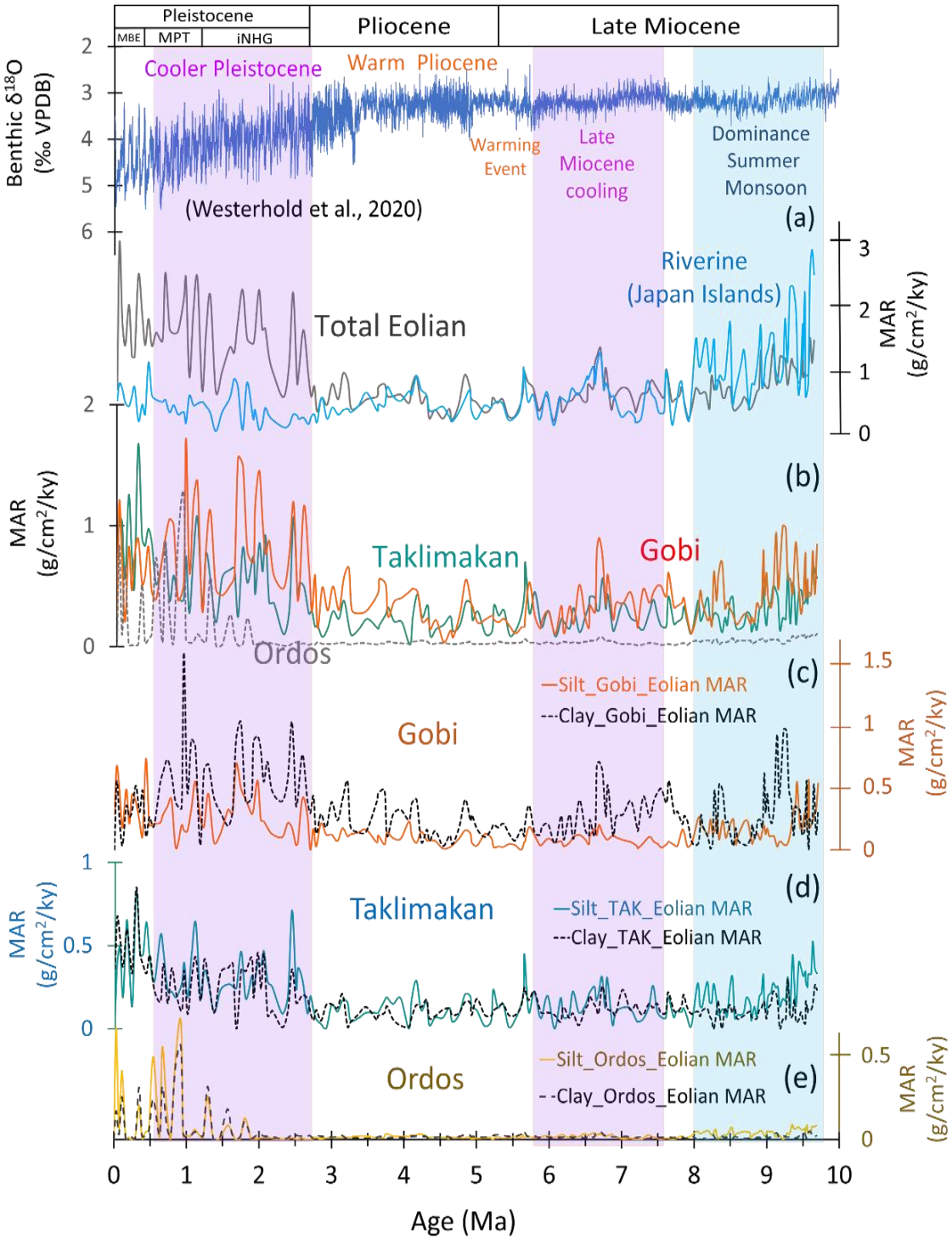

FIGURE 5.43 Temporal variations in eolian mass accumulation rates (MARs) at IODP Site U1425 in the Japan Sea since 10 Ma. (a) Total eolian and riverine materials and (b) total eolian material from Taklimakan, Gobi and Ordos; and dust fluxes in silt and clay fractions for (c) Gobi, (d) Taklimakan, and (e) Ordos. Benthic oxygen isotope data from Westerhold et al. (2020) are also shown at the top for comparison. The purple shading shows late Miocene Global cooling and Northern Hemisphere Glaciation. The blue shading indicates the dominance of the summer monsoon in the late Miocene.

Chapter 6. Discussion

In this research, we found Gobi silt and clay fluxes show significant differences in pattern, trend and quantity, while Taklimakan silt and clay fluxes show a similar trend and maintain a regular ratio from the late Miocene to the Pleistocene. These differences in flux variabilities might be controlled by the different modes of transportation paths from source regions to the Japan Sea during the past 10 Ma.

6.1 Grain-size variation of dust from Taklimakan and Gobi

Figure 5.43(d) shows that Taklimakan dust was generlly dominated by the silt fraction (Silt_TAK) from the late Miocene to the Pleistocene, which may reveal a typical characteristic of a long-range transport of dust from Taklimakan by the westerly wind. The atmospheric circulation in the Tarim Basin is controlled by high-level westerly winds, which are responsible for long-range dust transport (>5000 km) to the Japan Sea and Pacific Ocean (Sun et al., 2001). Desert materials in Taklimakan were entrained to an elevation of >5 km in the troposphere and were transported by rapid and strong westerly winds to downwind areas (Figure 6.11). During transportation, no dust fall was observed in the proximal areas of Chinese loess until it traveled downwind to the Japan Sea (Tsai et al., 2008). Hence, all entrained materials in the deserts were transported directly downwind which is supported by the result of a climate model study in the Asian dust transportation by westerly (Yang et al., 2021). Typical 4 μm far-traveled Asian dust and larger particles (>10 μm) were transported to Canada in April 2001, indicating a strong and rapid westerly jet in the troposphere (Zdanowicz et al., 2007).

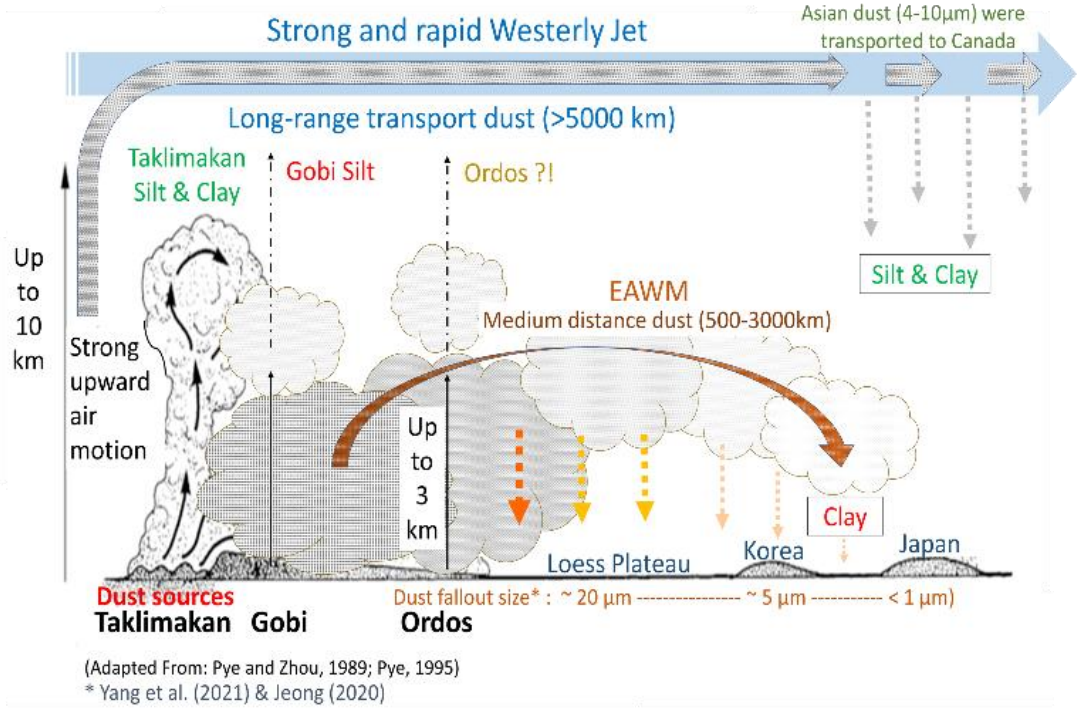

FIGURE 6.11 Schematic figure depicting the two dust transport modes, westerlies and low-level EAWM, as well as their depositional grain-size variations in the Japan Sea (modified from Pye and Zhou, 1989; Pye, 1995). Dust fallout sizes by the EAWM are according to Yang L. et al. (2021) and Jeong (2020).

In the case of Gobi materials, the clay-size fraction (Clay_Gobi) had a higher flux than the silt-size fraction (Silt_Gobi) from 9.24 to 0.73 Ma (Figure 5.43(c)). Because temporal flux variations of silt (Silt_Gobi) and clay (Clay_Gobi) fractions showed very different patterns and trends as well as their magnitude, silt and clay fractions were considered to be transported by different wind circulation modes from Gobi to the Japan Sea. Most desert materials in the Mongolian Gobi were entrained to an elevation of <3 km and carried by EAWM winds with a medium distance (500 to 3000 km) to the Chinese Loess, southeastern China, and the Japan Sea (Sun, 2002). When Gobi dust materials ascend to the highest elevation, the materials begin to descend and cause heavy dust to fall in the proximal region of CLP (Tsai et al., 2008; Sun, 2002). According to Liu (1988), CLP has been subdivided into three zones of sandy loess,

loess, and clayey loess zones from northwest to the south depending upon particle size which were sorted by wind blowing from the desert sources. Jeong et al. (2011) also found coarse silt was progressively replaced by the fine silt and clay from west to eastward on CLP. Coarse particle (5-20 μm) dust could be deposited on CLP (Yang L. et al., 2021), 2-5 μm dust has settled on the Korean Peninsula (Jeong, 2020), and only fine-grained dust (clay) could be suspended further to the Japan Sea and Southeast Asia (Yang et al., 2021; Figure 6.11). Although the effects of weathering should be considered, the gravitational settling during dust transportation by low-level winds of the EAWM is obvious. Therefore, it is reasonable to consider that clay-sized Gobi dust dominated from 9.24 to 0.73 Ma in the Japan Sea was mainly transported by low-level atmospheric circulation by EAWM winds (Figure 5.43 (c)). Figure 6.21 and 6.22 show that cooling events and trends found in the benthic $\delta^{18}O$ record (Westerhold et al., 2020) correspond well with the periods showing the higher flux of Gobi clay, which suggest that EAWM might be enhanced during cooling phase and glacial periods since 10 million years ago.

On the other hand, silt-sized Gobi dust in the Japan Sea revealed a similar MAR pattern and trend as those of Taklimakan dust, implying that coarser Gobi dust (silt) was mainly transported by westerlies to the Japan Sea. Sun (2002) and Tsai et al. (2008) also observed dust storm events in the Mongolian Gobi Deserts in which dust was entrained to the troposphere and transported by westerly winds to the Japan Sea and Pacific Ocean or America.

6.2 Detrital provenance variability in Japan Sea sediments

Late Miocene

High riverine flux from Japanese islands 9.6-8 Ma indicates a strong summer monsoon climate in East Asia, which is consistent with the clay mineral study at Linxia Basin in NE Tibet (Yang et al., 2021). A provenance shift occurred from 8-7 Ma; the Japanese riverine flux decreased to the lowest value, 0.2 g/cm^2/ky, and the eolian flux increased from 7.8-6.6 Ma in the Japan Sea (Figure 5.43(a)). Increase in eolian sedimentation at 8-7 Ma were also confirmed in the Loess Plateau, NE Tibetan Plateau, the Japan Sea and the North Pacific (Shen et al., 2017; Guo et al., 2002; Yang et al., 2017b; Rea et al., 1998).

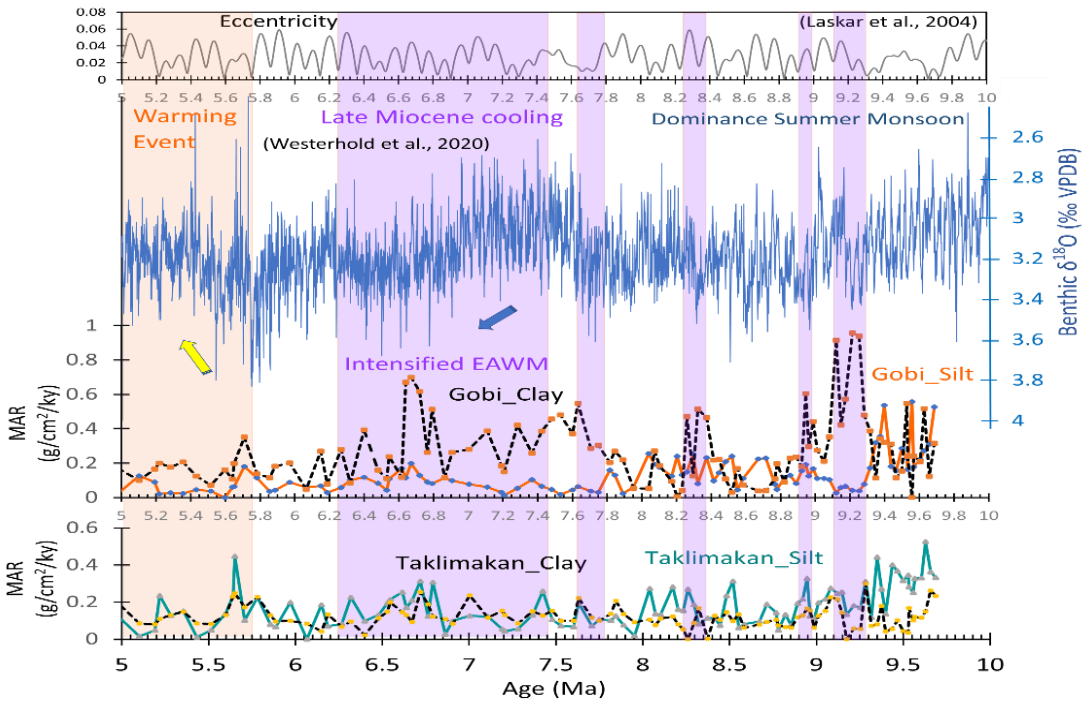

FIGURE 6.21 Dust fluxes in silt and clay fractions of Taklimakan and Gobi dust at IODP Site U1425 compared with benthic oxygen isotope data from Westerhold et al. (2020) and orbital eccentricity (Laskar et al., 2004) from 10 to 5 Ma. Gobi clay was associated with cooling (purple shading), and Taklimakan dust was associated with a warmer climate (orange shading) in the late Miocene to Pliocene. Arrows indicate the change in benthic oxygen isotope data during the late Miocene.

These data imply that Asian aridification approximately 8 Ma coincided with late Miocene global cooling (LMGC) between ~7 and ~5.5 Ma and with a short period of Northern Hemisphere glaciation between 6 and 5.5 Ma (Figure 6.21; Herbert et al., 2016; Holbourn et al., 2018). Eolian flux generally was low but occasionally increased to 1.39 and 1.02 g/cm^2/ky in 6.72 and 5.65 Ma, respectively, suggesting the aridity of the Asian interior and the intensification of the winter monsoon in East Asia (Figure 5.43(a); Matsuzaki et al., 2020). This intensification of the EAWM was also confirmed by the increase of grain size in the eolian deposits on the CLP in 7.4 Ma and 5.3 Ma (Fan et al., 2006).

Pliocene

The Warming Event appeared in the early Pliocene (Holbourn et al., 2018; Ao et al., 2021) after the late Miocene cooling was characterized by very low fluxes of eolian and riverine material, 0.2-1 g/cm^2/ky (Figure 5.43(a)), but had the highest biogenic contributions to the Japan Sea (Figure 5.42(b)). Shifts in dust provenance sources occurred from Gobi to Taklimakan during the warming event in 5.6-4 Ma (Figure 5.42(a)). According to a study by Ao et al. (2021) for eolian records in CLP, this warming event only increased summer monsoon moisture in East Asia, but enhanced aridification by increasing evaporation than precipitation in most parts of Central Asia. The riverine input from Japan islands did not show a prominent increase during the warming period (Figure 5.43(a)), suggesting continuously invariable summer precipitation at the eastern margin of Asia at that time. A gradual increase of eolian

material 3.2 Ma with decrease in biogenic materials followed by sudden cooling 3.3 Ma (Figure 5.42(b) and 6.22).

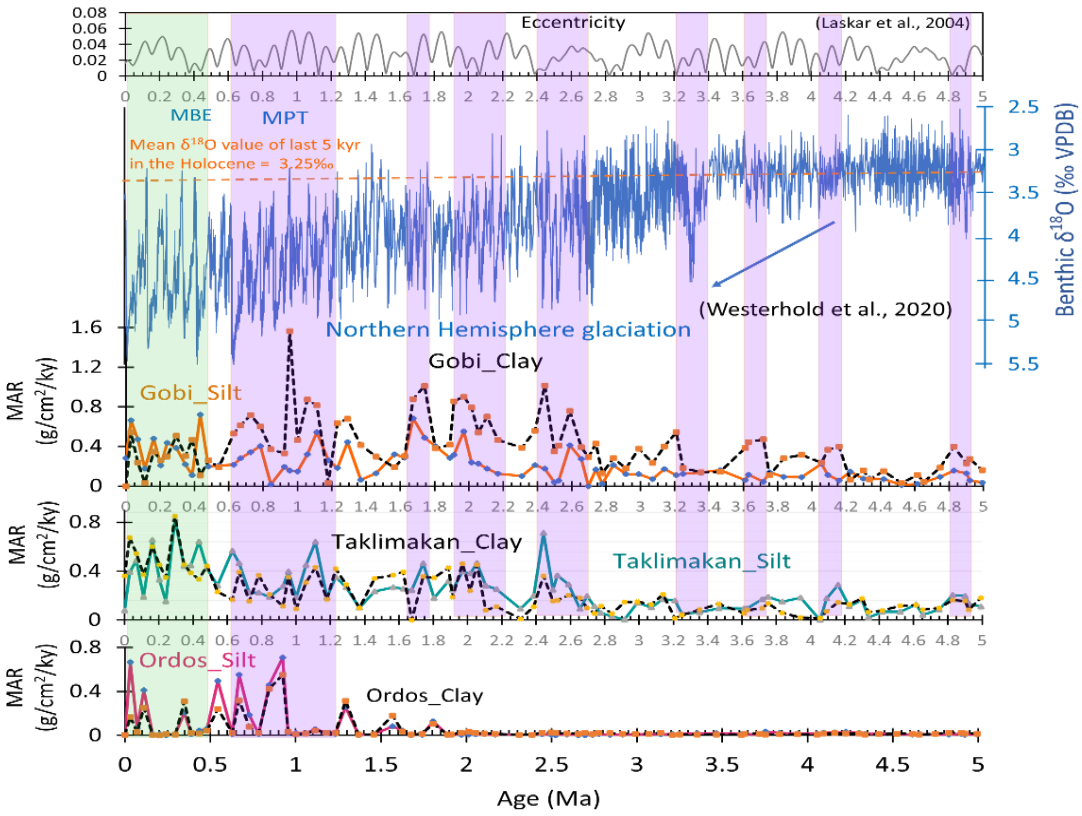

FIGURE 6.22 Dust fluxes in silt and clay fractions of Taklimakan, Gobi, and Ordos dust at IODP Site U1425 compared with benthic oxygen isotope data from Westerhold et al. (2020) and orbital eccentricity (Laskar et al., 2004) from 5 to 0 Ma. Gobi clay was associated with cooling/glaciation (purple shading), and Taklimakan dust was associated with a warmer/interglacial climate (green shading) in the Pliocene to Pleistocene. The orange dashed line is the mean $\delta^{18}O$ for the last 5 kyr in the Holocene (Raymo et al., 2018). The blue arrow indicates the substantial increase in benthic oxygen isotopes during the late Pliocene.

Pleistocene

A substantial increase in eolian MARs to 2.5 g/cm^2/ky occurred after 2.7 Ma (Figure 5.43(a)) in the Japan Sea during the intensified Northern Hemisphere Glaciation (iNHG), which established a cold and dry environment, accelerating sediment erosion in the Central Asian Mountain ranges and strengthening the atmospheric circulation systems in the Northern Hemisphere. Low temperatures during iNHG caused a greater

equator-to-pole temperature gradient and stronger thermal gradients along polar frontal systems (CLIMAP, 1976), resulting in stronger westerlies (Gates, 1976) and intensification of winter monsoon winds.

Gobi was the most significant dust contributor to the Japan Sea in the Early Pleistocene but decreased sharply after 0.95 Ma (Figure 6.22). Ordos dust increased only 0.95-0.85 Ma during the mid-Pleistocene transition (MPT) due to enhanced aridification in Northwest China which is evidenced by Li et al. (2015) for the Ulan Buh Desert and southern Inner Mongolia. The formation of deserts in the Mu Us and southern Inner Mongolia could be as old as the MPT (1.1-0.9 Ma) (Li et al. (2015) resulting in increased dust materials from the Ordos Plateau (Figure 6.22).

Taklimakan became the main dust contributor to the Japan Sea after 0.5 to 0.16 Ma during the Mid-Brunhes Event (MBE) (Figure 5.43(b) and 6.22), which corresponded to a period when Earth eccentricity was close to 0 (Berger, 1978; Laskar et al., 2004), and the benthic $\delta^{18}O$ record shows the largest variation between 3.2 and 5.4‰ in the Pleistocene (Westerhold et al., 2020) (Figure 6.22).

6.3 Implications for atmospheric circulation variability during the past 10 million years

Based on our dust records, we reconstructed the variability of paleoatmospheric circulation of westerly winds by using fluxes from Taklimakan, as well as silt-sized dust from Gobi (Gobi silt). The EAWM was inferred from clay-sized dust from Gobi (Gobi clay). The EASM and aridity changes in East Asia were inferred from Japanese riverine sediments during the last 10 million years (Figure 6.31). Therefore, four paleo

climatic significances were ascertained for the last 10 Ma years in the Japan Sea sediments and described in the following subsections.

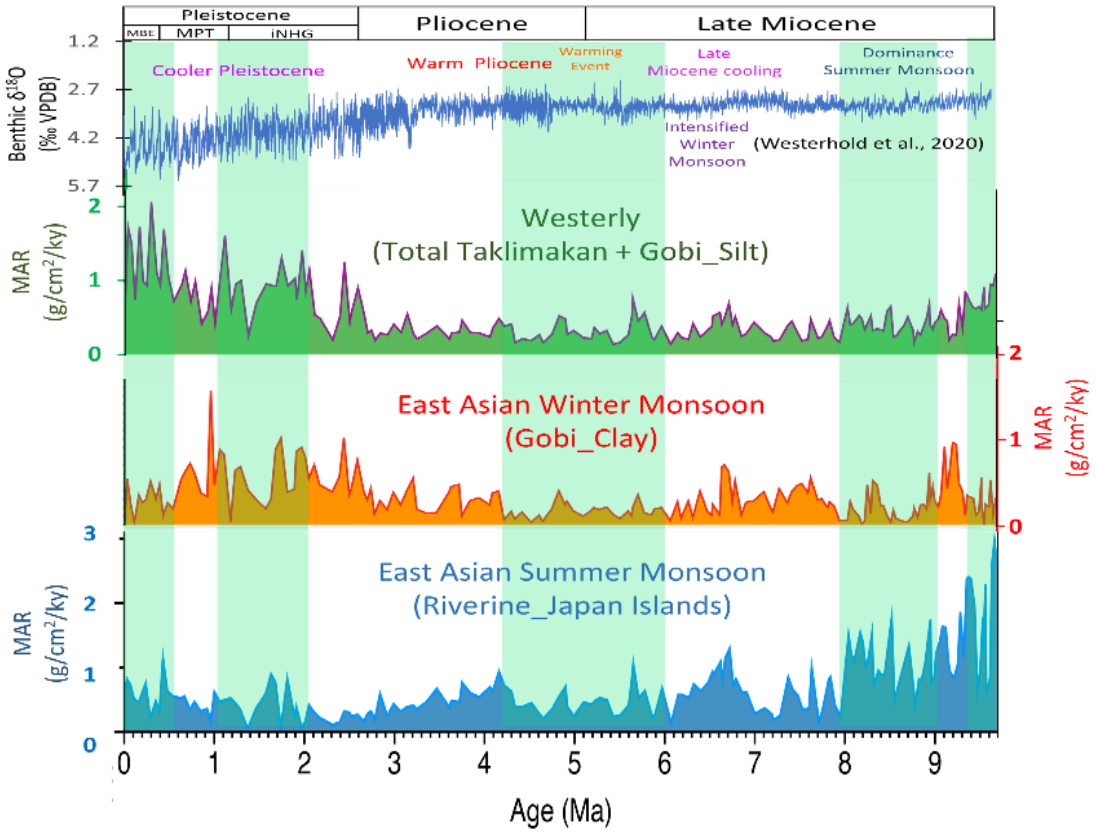

FIGURE 6.31 Variability of paleoatmospheric circulation of westerlies, East Asian winter monsoon (EAWM) and East Asian summer monsoon (EASM) reconstructed from the fluxes of eolian and riverine input to IODP Site U1425 in the Japan Sea since 10 Ma. The green shading shows the dominance of westerly winds. Benthic oxygen isotope data from Westerhold et al. (2020) are also shown at the top for comparison.

Dominance of the EASM 9.6-8 Ma

The dominance of the EASM in East Asia from 9.6-8 Ma suggested warm air and moisture from the southeast, which was inferred from the high Japanese riverine flux record (Figure 6.31). The eolian deposits accumulated on the CLP had a low deposition rate and strong pedogenesis, which revealed intensified precipitation during this period (Sun et al., 2015). In the same period, TAK and Gobi silt dust dominated 9.6-9.4 and 8.9-8 Ma, indicating that westerly winds were strong. In addition, high flux of Gobi

clay 9.3-8.9 Ma suggested that the EAWM winds were enhanced during a less pronounced, late Miocene cooling step ~9.0 Ma (Figure 6.21; Holbourn et al., 2013). The high-frequency fluctuations in dust grain size and dust source materials during this period suggested that unstable atmospheric circulation prevailed in East Asia during the dominance of the EASM in the late Miocene (Figure 6.21).

Increase aridification in inland Asia after 8 Ma

The EASM was strong 9.6-8 Ma, but relatively weak in 8-7, 6-4.5 and 3-2 Ma in the Japan Sea region, which might contradict some CLP records in China which proposed EASM increase in the Miocene–Pliocene climate transition (Ao et al., 2021). The evolution of EASM in East Asia during this period and its controlling mechanisms remain controversial (Wang et al., 2021) and complicated because EASM precipitation also depended on the variation of regional and local environments. The controls on aridification in inland Asia at ~8 Ma might involve the retreat of EASM, global cooling, and the uplift of the Tibetan Plateau. It seems widely accepted that the uplift of the Tibetan Plateau played a significant role in the long-term aridification of inland Central Asia during Cenozoic by modulating the atmospheric circulation and blocking moisture from southeast Asia (Tada et al., 2016; An et al., 2001). Based on a climate modelling study, Zhang et al. (2022) demonstrated the growth of the Tibetan Plateau and the uplift of the northern Tibetan Plateau expanded drylands in central Asia to the north of ~40°N resulting in the same dryland zone at higher latitudes as the present. In the latest Miocene or the Pliocene, the northern and eastern part of the Tibetan Plateau

and adjacent mountain ranges were still uplifted (Zheng et al., 2006) that may have intensified aridity in inland and Central Asia at 8 Ma and afterward.

Global cooling enhances EAWM

The dominance of the EAWM was linked to global cooling, such as LMGC (Figure 6.21), as well as the increase in ice sheets in the Northern Hemisphere, such as iNHG and MPT (Figure 6.22). This observation suggested that global cooling could have strengthened the low-level EAWM winds (Sun et al., 2020) and increased dust emissions from the Mongolian Gobi and northern China deserts to the Japan Sea.

During the late Miocene cooling period, Gobi clay significantly contributed to the total eolian flux in the Japan Sea (Figure 6.21) from 7.8 to 6 Ma, suggesting Asian aridification and intensification of the EAWM. Although this fast late Miocene cooling could be triggered by an abrupt decrease in CO_2 or the uplift of the Tibetan Plateau, the true mechanism is still unclear and under hot debate (Shen et al., 2017; Fan et al., 2006; Yang Y. et al., 2021; Lu et al., 2022). Slight increases in Gobi clay 4, 3.6 and 3.2 Ma (Figure 6.22) suggest progressive global cooling, which was associated with the occurrence of ice-rafted debris (IRD) at the north pole in the late Pliocene until the beginning of the Northern Hemisphere Glaciation (Raymo et al., 2018; Thiede et al., 1998).

During the iNHG, increasing Siberian High activity strengthened the EAWM winds (Ding et al., 1995) in northern China, which increased dust storm events as well as dust transportation from the Gobi and northern China deserts. Gobi clay increased substantially from the late Pliocene to the early Pleistocene until 0.6 Ma (Figure 6.22).

On the other hand, some studies suggested that the strong Siberian High and EAWM forced the westerly winds to migrate southward (Ono and Irino, 2004; Kapp et al., 2011; Pullen et al., 2011) during the strong glacial and cooling periods. Another study on the loess in the Tarim basin suggests that expansion of Northern Hemisphere ice sheets could intensify the strength of the westerly jet and push it southward, which enhanced aridity and intensified dust storm activity in the Tibetan Plateau (Fang et al., 2020). The increase in accumulation of Taklimakan dust and Gobi silt in the Japan Sea indicated a prolonged interval of westerly wind blowing on the inland desert area since the early Pleistocene (Figure 6.22).

Role of westerly for dust transport

During the warmer periods in the Warming Event in the late Miocene to early Pliocene and the Late Pleistocene, weakened cold air masses from the Siberian High could permit a northward migration of westerly winds in an earlier season (Abell et al., 2021; Yang et al., 2017a; Lu et al., 2020). Dust provenance changes from Gobi to TAK 5.8-4.2 Ma (Figure 5.42(a) and 6.31) during the Warming Event revealed the dominance of westerly winds but was characterized by low dust deposition in the Japan Sea.

The influence of westerlies increased gradually, reflecting the increasing fluxes of TAK and Gobi silt from 2.5 to 1.1 Ma and became dominant in the Late Pleistocene from 0.5 Ma to the present. The early northward migration of westerlies increased the duration of westerlies over the Taklimakan Desert and resulted in an increase in the length of season for dust storms and dust transportation from the Taklimakan Desert,

as well as deserts in northern China, to the Japan Sea. A similar situation can currently be observed with a longer dust season from April to August (Schiemann et al., 2009). During the dominance of westerlies, Gobi silt also increased accordingly and had a higher flux than Gobi clay from 0.5 Ma to the present (Figure 6.22).

Under recent global warming conditions, the dominance of westerly winds is obvious, which calls our attention to the influence on the regional and local climate. Extreme weather events such as heat waves and large storms are likely to become more frequent or more intense in the coming future. Although the behaviors of regional climate and weather are complicated to understand and forecast, long-term global climate changes in the past, such as the warming in the Pliocene or the dominance of the summer monsoon in the late Miocene, may provide the basis to solve the riddle and the problems that we are facing now or will face in the future.

Chapter 7. Conclusions

This work provides empirical evidence for the major changes in paleoatmospheric circulation of westerlies, the EAWM and aridity changes in the dust source region since 10 Ma using a sediment sequence from IODP Site U1425 in the Japan Sea. Mineralogical analyses of the sediment at IODP Site U1425 effectively established a proxy for the eolian provenance study. The mineral compositions could distinguish the detrital sources, such as dust from Taklimakan and Gobi and riverine input from the Japanese islands.

In order to solve the problems in eolian provenance, we applied PARAFAC end-member modelling, which is a powerful analytical tool to quantitatively differentiate eolian dust sources, such as those in Taklimakan, Gobi, and the Ordos Plateau, as well as the other subcomponents in the sediment. New dust records of Gobi, Taklimakan and Ordos source changes in the silt and clay fractions resolved the transport process and distinguished the effects of climatic intervention on dust transportation changes in the past.

There are four paleo climatic significances for the last 10 Ma years in the Japan Sea sediments. The dominance of the EAWM was linked to the LMGC, iNHG and MPT associated with global cooling and the increase in ice sheets in the Northern Hemisphere, which strengthened the low-level EAWM winds and increased the deposition of fine clay dust from Mongolian Gobi. In contrast, during the dominance of westerlies in the warmer periods during the Warming Event in the late Miocene to early Pliocene, as well as in the late Pleistocene, early seasonal northward migration of

westerlies prolonged the duration of westerlies over the inland desert area, which resulted in the deposition of coarser silt-sized eolian dust from the Taklimakan and Gobi Deserts.

The EASM was strong 9.6-8 Ma, while it showed fluctuation at moderate intensity after 8 Ma to the Pleistocene in the Japan Sea region. Stepwise Asian aridification occurred 8, 6, and 2 Ma and finally induced desertification in the Ordos Plateau area. A significant increase in Ordos dust contribution to the Japan Sea in the Late Pleistocene was related to the increase in aridity in Inner Mongolia and the Ordos Plateau since 2 Ma, and the enhanced aridification 1.5-0.6 Ma induced desertification in southern Inner Mongolia during the MPT.

Acknowledgments

I would like to express my sincere thanks to my supervisor Dr. Tomohisa Irino for the support and guidance of this research, and all participants of IODP Exp. 346 for their efforts to provide high-quality continuous sediment records from the Japan Sea. I also thank Profs. Atsuko Sugimoto, Masanobu Yamamoto and Youhei Yamashita for their valuable advice throughout this study. Profs. Ryuji Tada, Hongbo Zheng, Youbin Sun, and Hitoshi Hasegawa kindly permitted us to use their loess and desert samples.

References

Abell, J.T., Winckler, G., Anderson, R.F., and Herbert, T.D., 2021, Poleward and weakened westerlies during Pliocene warmth: Nature, v. 589, p.70-75.

An, Z., Kutzbach, J., Prell, W., et al., 2001, Evolution of Asian monsoons and phased uplift of the Himalaya–Tibetan plateau since Late Miocene times: Nature, v. 411, p. 62–66, https://doi.org/10.1038/35075035.

Anderson, C. H., Murray, R. W., Dunlea, A. G., Giosan, L., Kinsley, C. W., McGee, D., and Tada, R., 2020, Aeolian delivery to Ulleung Basin, Korea (Japan Sea), during development of the East Asian Monsoon through the last 12 Ma: Geological Magazine, v. 157, p. 806-817, https://doi.org/10.1017/S001675681900013X

Anonymous, 1991, Petroleum geology of the Tarim basin, Science Press (seven volumes), Beijing.

Ao, H., Rohling, E. J., Zhang, R., et al., 2021, Global warming-induced Asian hydrological climate transition across the Miocene–Pliocene boundary: Nature Communications, v. 12.

Arnold, E., Leinen, M., and King, J., 1995, Paleoenvironmental variation based on the mineralogy and rock-magnetic properties of sediment from Sites 885 and 886 in: Proceedings of the Ocean Drilling Program, Scientific Results, Ocean Drilling Program, p. 231–245.

Berger, A., 1978, Long term variations of daily insolation and Quaternary climatic changes: Journal of Atmospheric Science, v. 35, p. 2362-2367.

Berger, W.H., and Jansen, E., 1994, Mid-Pleistocene climate shift: the Nansen connection: in Johannessen OM, Muench RD, Overland JE (eds) The polar oceans and their role in shaping the global environment, p. 295–311, American Geophysical Union, Washington, https://doi.org/10.1029/GM085p0295.

Berner, E. K., and Berner, R. A., 1996, Global Environment—Water, Air, and Geochemical Cycles, Prentice Hall, New Jersey.

Biscaye, P. E., 1965, Mineralogy and Sedimentation of Recent Deep-Sea Clay in the Atlantic Ocean and Adjacent Seas and Oceans: GSA Bulletin, v. 76, p. 803–832.

Bro, R., 1997, PARAFAC. Tutorial and applications: Chemometrics and Intelligent Laboratory Systems, v. 38, p. 149-171.

Carroll, A.R., Graham, S.A., Hendrix, M.S., Ying, D., and Zhou, D., 1995, Late Paleozoic tectonic amalgamation of northwestern China: Sedimentary record of the northern Tarim, northwestern Turpan, and southern Junggar basins: Geological Society of America Bulletin, v. 107, p. 571–594.

Caves, J.K., et al., 2015, Role of the westerlies in Central Asia climate over the Cenozoic: Earth and Planetary Science Letters, v. 428, p. 33–43.

Chen, J., Li, G., Yang, J., et al., 2007, Nd and Sr isotopic characteristics of Chinese deserts: Implications for the provenances of Asian dust: Geochimica et Cosmochimica Acta, v. 71, p. 3904-3914, https://doi.org/10.1016/j.gca.2007.04.033.

CLIMAP Project Members, 1976, The surface of the ice-age earth: Science, v. 191, p. 123-137.

Dadey, K. A., Janecek, T., and Klaus, A., 1992, Dry-bulk density: Its use and determination: Proceedings of the Ocean Drilling Program, Scientific Results, v. 126.

Davidson, S.C., 2005, Sedimentation History and Provenance Analysis of a Late Mesozoic Rifting Event at Tavan Har, East Gobi, Mongolia: Frontiers, The Interdisciplinary Journal of Study Abroad, p. 91-122.

Ding, Z., Liu T., Rutter N. W. et al., 1995, Ice-Volume Forcing of East Asian Winter Monsoon Variations in the Past 800,000 Years: Quaternary Research, v. 44, no. 2, p. 149-159.

Ehrmann, W., 1998, Implications of late Eocene to early Miocene clay mineral assemblages in McMurdo Sound (Ross Sea, Antarctica) on paleoclimate and ice dynamics: Palaeogeography, Palaeoclimatology, Palaeoecology, v. 139, p. 213-231.

Fan, M., Song, C., Dettman, D.L., Fang X., and Xu, X., 2006, Intensification of the Asian winter monsoon after 7.4 Ma: Grain-size evidence from the Linxia Basin, northeastern Tibetan Plateau 13.1 Ma to 4.3 Ma: Earth and Planetary Science Letters, v. 248, p. 186-197, https://doi.org/10.1016/j.epsl.2006.05.025.

Fang, X., An, Z., Clemens, S. C., et al., 2020, The 3.6-Ma aridity and westerlies history over midlatitude Asia linked with global climatic cooling: Earth, Atmospheric, and Planetary Sciences, v. 117 (40),

https://doi.org/10.1073/pnas.1922710117.

Gates, W. L., 1976, Modelling the ice-age climate: Science, v. 191, p. 1138-1144.

Guo, Z. T., Sun, B., Zhang, Z. S., Peng, S. Z., Xiao, G. Q. et al., 2008, A major reorganization of Asian climate by the early Miocene: Climate of the Past, v. 4, p. 153–174, https://doi.org/10.5194/cp-4-153-2008.

Guo, Z. T., Ruddiman, W. F., Hao, Q. Z., et al., 2002, Onset of Asian desertification by 22 Myr ago inferred from loess deposit in China: Nature, v. 416, p. 159–163.

Herbert, T.D., Lawrence, K.T., Tzanova, A., Peterson, L.C., Caballero-Gill, R., and Kelly, C.S., 2016, Late Miocene global cooling and the rise of modern ecosystems: Nature Geoscience, v. 9, p. 843–847, https://doi .org/10.1038/NGEO2813.

Holbourn, A., Kuhnt, W., Clemens, S., et al., 2013, Middle to Late Miocene stepwise climate cooling: evidence from a high-resolution deep water isotope curve spanning 8 million years: Paleoceanography, v. 28, p. 688–699.

Holbourn, A.E., Kuhnt, W., Clemens, S.C., Kochhann, K.G., Jöhnck, J., Lübbers, J., and Andersen, N., 2018, Late Miocene climate cooling and intensification of southeast Asian winter monsoon: Nature Communications, v. 9, 1584, https://doi.org/10.1038/s41467-018-03950-1.

Irino, T., and Tada, R., 2000, Quantification of aeolian dust (Kosa) contribution to the Japan Sea sediments and its variation during the last 200 ky: Geochemical Journal, v. 34, p. 59-93.

Irino, T., Tada, R., Ikehara, K., Sagawa, T., Karasuda, A., Kurokawa, S., Seki, A., and Lu, S., 2018, Construction of perfectly continuous records of physical properties for dark-light sediment sequences collected from the Japan Sea during Integrated Ocean Drilling Program Expedition 346 and their potential utilities as paleoceanographic studies: Progress in Earth and Planetary Science, v. 5, 23, https://doi .org/10.1186/s40645-018-0176-7.

Isozaki, Y., Tada, R., Sun, Y., et al., 2020, Origin of aeolian dust emitted from the Tarim Basin based on the ESR signal intensity and crystallinity index of quartz: the recycling system of fine detrital material within the basin: Geological Magazine, v. 157, p. 707-718.

Janecek, T. R., 1984, Eolian Sedimentation in the Northwest Pacific Ocean: A Preliminary Examination of the data from Deep Sea Drilling Project Sites 576 and 578," in Initial Reports, G. R. Heath, L. H. Burckle et al., Eds., DSDP, v. 86, p. 589-603, Washington.

Jansen, J.H.F., Kuijpers, A., Troelstra, S.R., 1986, A mid-Brunhes climatic event: long term changes in global atmosphere and ocean circulation, Science, v. 232, p. 619–622, https://doi.org/10.1126/science.232.4750.619.

Jeong, G.Y., Hillier, S., and Kemp, R.A., 2011, Changes in mineralogy of loess–paleosol sections across the Chinese Loess Plateau: Quaternary Research, v. 75, p. 245–255.

Jeong, G.Y., 2020, Mineralogy and geochemistry of Asian dust: dependence on migration path, fractionation, and reactions with polluted air: Atmospheric

Chemistry and Physics, v. 20, p. 7411–7428, https://doi.org/10.5194/acp-20-7411-2020.

Jia, C., Wei, G., Wang, L., Jia, D., and Guo, Z., 1997, Tectonic Characteristics and Petroleum, Tarim Basin, China: Petroleum Industry Press, Beijing (in Chinese with English abstract).

Johnson, C. L., Webb, L. E., Graham, S. A., Hendrix M. S., and Badarch, G., 2001, Sedimentary and structural records of late Mesozoic high-strain extension and strain partitioning, East Gobi basin, southern Mongolia, in Hendrix.

Kamikuri, S., Itaki, T., Motoyama, I., and Matsuzaki, M.K., 2017, Radiolarian biostratigraphy from middle Miocene to late Pleistocene in the Japan Sea: Paleontological Research, v. 21, p. 397–421, https:// doi .org /10 .2517 /2017PR001.

Kapp, P., Pelletier, J. D., Rohrmann A., et al., 2011, Wind erosion in the Qaidam basin, Central Asia: Implications for tectonics, paleoclimate, and the source of the Loess Plateau: The Geological Society of America Today, v. 21, p. 4–10.

Krumbein, W. C., and Pettijohn, F. J., 1938, Manual of sedimentary Petrography: Appleton-Century-Crofts, Inc., New York.

Kübler, B., 1964, Les argiles, indicateurs de métamorphisme: Review Institute Francais du Pétrole, v. 19, p. 1093–1112.

Kurokawa, S., Tada, R., Matsuzaki, K.M., Irino, T., and Johanna, L., 2019, Cyclostratigraphy of the late Miocene to Pliocene sediments at IODP sites U1425 and U1430 in the Japan Sea and paleoceanographic implications:

Progress in Earth and Planetary Science, v. 6, 2, https://doi.org/10.1186/s40645-018-0250-1.

Kusky T. M., and Li, J., 2003, Paleoproterozoic tectonic evolution of the North China Craton: Journal of Asian Earth Sciences, v. 22, p. 383-397.

Lamb, H. H., and Woodroffe A., 1970, Atmospheric circulation during the last ice age: Quaternary Research, v. 1, p. 29-58.

Laskar, J., Robutel, P., Joutel. F., Gastineau. M., Correia. ACM., and Levrard, B., 2004, A long term numerical solution for the insolation quantities of the Earth: Astron Astrophys, v. 428, p. 261–285, https://doi.org/10.1051/0004-6361:20041335.

Leinen, M., and Heath, G.R., 1981, Sedimentary indicators of atmospheric activity in the northern hemisphere during the Cenozoic: Palaeogeography, Palaeoclimatology, Palaeoecology, v. 36, p. 1-21.

Li, G., Jin, M., Chen, X., et al., 2015, Environmental changes in the Ulan Buh Desert, southern Inner Mongolia, China since the middle Pleistocene based on sedimentology, chronology and proxy indexes: Quaternary Science Reviews, v. 128, p. 69-80, http://dx.doi.org/10.1016/j.quascirev.2015.09.010.

Liu, T. S., 1988, Loess in China, China Ocean Press, Springer-Verlag, Berlin.

Liu, Z., Zhao, Y., Colin, C., et al., 2009, Chemical weathering in Luzon, Philippines from clay mineralogy and major-element geochemistry of river sediments: Applied Geochemistry, v. 24, 11, p. 2195-2205.

Lisiecki, L.E., and Raymo, M.E., 2005, A Pliocene-Pleistocene stack of 57 globally

distributed benthic $\delta^{18}O$ records: Paleoceanography, v. 20, PA1003, https://doi.org/10.1029/2004PA001071.

Lu, H., Malusà, M.G., Zhang, Z., Guo, L., et al., 2022, Syntectonic sediment recycling controls eolian deposition in eastern Asia since ~8 Ma: Geophysical Research Letters, v. 49, https://doi. org/10.1029/2021GL096789.

Lu, Y., Dewald, N., Koutsodendris, A., Kaboth-Bahr, S., Rösler, W., Fang, X., et al., 2020, Sedimentological evidence for pronounced glacial-interglacial climate fluctuations in NE Tibet in the latest Pliocene to early Pleistocene: Paleoceanography and Paleoclimatology, v. 35, https://doi.org/10.1029/2020PA003864

Matsuzaki, K.M., Suzuki, N., and Tada, R., 2020, An intensified East Asian winter monsoon in the Japan Sea between 7.9 and 6.6 Ma: Geology, v. 48, p. 919–923, https://doi.org/10.1130/G47393.1

Murphy, K.R., Stedmon, C.A., Graeber, D., and Bro, R., 2013, Fluorescence spectroscopy and multi-way techniques: PARAFAC, Analytical Methods, v. 5, p. 6557–6566.

Nakada, S., Yamamoto, T., and Maeno, F., 2016, The geology of Japan: The Geological Society, London.

Nagashima, K., Tada, R., Matsui, H., Irino, T., Tani, A. and Toyoda, S., 2007, Orbital- and millennial-scale variations in Asian dust transport path to the Japan Sea: Palaeogeography, Palaeoclimatology, Palaeoecology, v. 247, p. 144-161, https://doi.org/10.1016/j.palaeo.2006.11.027.

Nagashima, K., Tada, R., Tani A., et al., 2007, Contribution of Aeolian dust in Japan Sea sediments estimated from ESR signal intensity and crystallinity of quartz: Geochemistry Geophysics Geosystem, v. 8, no. 2.

Nagashima, K., Nishido, H., Kayama M., et al., 2017, Composition of Asian dust from cathodoluminescence spectral analysis of single quartz grains: Geology, v. 45, p. 879-882.

Ono, Y., and Irino, T., 2004, Southern migration of westerlies in the Northern Hemisphere PEP II transect during the Last Glacial Maximum: Quaternary International, v. 118–119, p. 13–22.

Petschick, R., Kuhn G., and Gingele, F., 1996, Clay mineral distribution in surface sediments of the South Atlantic: Maine Geology, v. 130, p. 203-229.

Prospero, J. M., and Bonatti, E., 1969, Continental dust in the atmosphere of the Eastern Equatorial Pacific: Geophysical Research Letters, v. 74, p. 3362-3371, doi:10.1029/JC074i013p03362.

Pullen, A., Kapp, P., McCallister, A. T., et al., 2011, Qaidam Basin and northern Tibetan Plateau as dust sources for the Chinese Loess Plateau and paleoclimatic implications: Geology, v. 39, p. 1031–1034.

Pye, K., and Zhou, L. P., 1989, Late Pleistocene and Holocene aeolian dust deposition in North China and the Northwest Pacific Ocean: Palaeogeography Palaeoclimatology and Palaeoecology, v. 73, p. 11-23.

Pye, K., 1995, The nature, origin and accumulation of loess: Quaternary Science Reviews, v. 14, p. 653-667.

Raymo, M. E., Kozdon, R., Evans, D., et al., 2018, The accuracy of mid-Pliocene $\delta^{18}O$-based ice volume and sea level reconstructions: Earth-Science Reviews, v. 177, p. 291-302.

Rea, D.K., and Janecek, T.R., 1981, Mass-accumulation rates of the non-authigenic inorganic crystalline (eolian) component of deep-sea sediments from the western mid-Pacific Mountains, Deep Sea Drilling Project Site 463, in Initial Reports, J. Thiede, T.L. Vallier et al., Eds, DSDP, v. 62, p. 653-659, Washington.

Rea, D.K., Snoeckx, H., and Joseph, L.H., 1998, Late Cenozoic eolian deposition in the North Pacific: Asian drying, Tibetan uplift, and cooling of the Northern Hemisphere: Paleoceanography, v. 13, p. 215–224, https://doi.org/10.1029/98PA00123.

Rittner, M., Vermeesch, P., Carter, A., Bird, A., et al., 2016, The provenance of Taklamakan desert sand: Earth and Planetary Science Letters, v. 437, p. 127-137, https://doi.org/10.1016/j.epsl.2015.12.036.

Schiemann, R., Lüthi, D., and Schär, C., 2009, Seasonality and interannual variability of the Westerly Jet in the Tibetan Plateau region: Journal of Climate, v. 22, p. 2940–2957, DOI: 10.1175/2008JCLI2625.1.

Shen, X., Wan, S., France-Lanord, C., Clift, P.D., Tada R., et al., 2017, History of Asian eolian input to the Sea of Japan since 15 Ma: Links to Tibetan uplift or global cooling?: Earth and Planetary Science Letters, v. 474, p. 296-308, https://doi.org/10.1016/j.epsl.2017.06.053.

Stedmon, C. A., and Bro, R., 2008, Characterizing dissolved organic matter fluorescence with parallel factor analysis: a tutorial: Limnology and Oceanography, v. 6, p. 572-579.

Sun, J., Zhang, M., and Liu, T., 2001, Spatial and temporal characteristics of dust storms in China and its surrounding regions, 1960-1999: Relations to sources area and climate: Journal of Geophysical Research, v. 106, p. 10,325-10,333.

Sun, J., 2002, Provenance of loess material and formation of loess deposits on the Chinese Loess Plateau: Earth and Planetary Science Letters, v. 203, p. 845–859.

Sun, J., Ding, Z., Xia, X., Sun, M., and Windley, B.F., 2018, Detrital zircon evidence for the ternary sources of the Chinese Loess Plateau: Journal of Asian Earth Sciences, v. 155, p. 21-34, https://doi.org/10.1016/j.jseaes.2017.10.012.

Sun X., and Wang P., 2005, How old is the Asian monsoon system?-Palaeobotanical records from China: Palaeogeography, Palaeoclimatology, Palaeoecology, v. 222, p. 181–222, doi:10.1016/j.palaeo.2005.03.005.

Sun, Y., Tada, R., Chen J., et al., 2007, Distinguishing the sources of Asian dust based on electron spin resonance signal intensity and crystallinity of quartz: Atmospheric Environment, v. 41, p. 8537-8548.

Sun, Y., Ma, L., Bloemendal, J., Clemens, S., Qiang, X., and An, Z., 2015, Miocene climate change on the Chinese Loess Plateau: Possible links to the growth of the northern Tibetan Plateau and global cooling: Geochemistry, Geophysics, Geosystems, v. 16, p. 2097–2108.

Sun, Y., Yan, Y., Nie, J., Li, G., Shia, Z., Qiang, X., Chang, H., and An, Z., 2020, Source-to-sink fluctuations of Asian aeolian deposits since the late Oligocene: Earth-Science Reviews, v. 200, 102963.

Tada, R., Murray, R.W., Alvarez-Zarikian, C., and the Expedition 346 Scientists, 2015, Proceedings of Integrated Ocean Drilling Program, volume 346, College 233 Station, TX (Integrated Ocean Drilling Program). https://doi.org/10.2204/iodp.proc.346.106.2015

Tada, R., Zheng H., and Clift P. D., 2016, Evolution and variability of the Asian monsoon and its potential linkage with uplift of the Himalaya and Tibetan plateau: Progress in Earth and Planetary Science, v. 3, no. 4.

Tada, R., Irino, T., Ikehara, K., Karasuda, A., Sugisaki, S., Xuan, C., Sagawa, T., Itaki, T., Kubota, Y., Lu, S., Seki, A., Murray, R.W., Alvarez-Zarikian, C., Anderson, W.T., and Expedition 346 Scientists, 2018, High-resolution and high-precision correlation of dark and light layers in the Quaternary hemipelagic sediments of the Japan Sea recovered during IODP Expedition 346: Progress in Earth and Planetary Science, v. 5, 19, https://doi: 10.1186/s40645-018-0167-8.

Thiede, J., Winkler, A., Wolf-Welling T., et al., 1998, Late Cenozoic history of the polar North Atlantic: Results from ocean drilling: Quaternary Science Reviews, v. 17, pp. 185-208.

Tsai, F., Chen, George T. J., Liu, T.H., Lin, W.D., and Tu, J.Y., 2008, Characterizing the transport pathways of Asian dust: Journal of Geophysical Research, v.

113, D17311, https://doi:10.1029/2007JD009674.

Wang, M. Y., et al., 2021, Late Miocene-Pliocene Asian summer monsoon variability linked to both tropical Pacific temperature and Walker Circulation: Earth and Planetary Science Letters, v. 561.

Wang, Y. Q., Zhang, X. Y., Gong, S.L., Zhou C. H., et al., 2008, Surface observation of sand and dust storm in East Asia and its application in CUACE/Dust: Atmospheric Chemistry and Physics, l. 8, p. 545–553, https://doi.org/10.5194/acp-8-545-2008.

Wang, Z., Wu, J., Lu, X., Zhang J., and Liu, C., 1986, An outline on the tectonic evolution of the Tian Shan of China: Bulletin of the Institute of Geology, Chinese Academy of Geological Sciences, v, 15, p. 81-92 (in Chinese with English abstract).

Watson, M. P., Hayward, A. B., Parkinson, D.N., and Zhang, ZH. M., 1987, Plate tectonic history, basin development and petroleum source rock deposition onshore China: Marine and Petroleum Geology, v. 4, p. 205–225.

Westerhold et al., 2020, An astronomically dated record of Earth's climate and its predictability over the last 66 million years: Science, v. 369, p.1383–1387.

Yang, L., Shi, Z., Sun, H., et al., 2021, Distinct effects of winter monsoon and westerly circulation on dust aerosol transport over East Asia: Theoretical and Applied Climatology, v. 144, p. 1031–1042, https://doi.org/10.1007/s00704-021-03579-z.

Yang, Y., Yang, R., Li, X., et al., 2017a, Glacial-interglacial climate change on the

northeastern Tibetan Plateau over the last 600kyr: Palaeogeography, Palaeoclimatology, Palaeoecology, v. 476, p. 181-191, https://doi.org/10.1016/j.palaeo.2017.04.007.

Yang, Y., Galy, A., Fang, X., et al., 2017b, Eolian dust forcing of river chemistry on the northeastern Tibetan Plateau since 8 Ma: Earth and Planetary Science Letters, v. 464, p. 200-210, https://doi.org/10.1016/j.epsl.2017.02.009.

Yang, Y., Ye, C., Galy, A., et al., 2021, Monsoon enhanced silicate weathering as a new atmospheric CO_2 consumption mechanism contributing to fast late Miocene global cooling: Paleoceanography and Paleoclimatology, v. 36, https://doi. org/10.1029/2020PA004008.

Yu, Y., Kalashnikova, O. V., Garay, M.J., and Notaro, M., 2019, Climatology of Asian dust activation and transport potential based on MISR satellite observations and trajectory analysis: Atmospheric Chemistry Physic, v. 19, p. 363–378, https://doi.org/10.5194/acp-19-363-2019.

Zdanowicz, C., Hall, G., Vaive, J., Amelin, Y., Percival, J., Girard, I., Biscaye, P., and Bory, A., 2007, Asian dustfall in the St. Elias Mountains, Yukon, Canada: Geochimica et Cosmochimica Acta, v. 70, p. 3493–3507.

Zhang, R., Zhang, Z., Jiang, D., Ramstein, G., Dupont-Nivet, G., and Li, X., 2022, Tibetan Plateau made central Asian drylands move northward, concentrate in narrow latitudinal bands, and increase in intensity during the Cenozoic: Geophysical Research Letters, v. 49, https://doi.org/10.1029/2021GL093718.

Zhang, W., Chen, J., Ji, J., and Li, G., 2016, Evolving flux of Asian dust in the North

Pacific Ocean since the late Oligocene: Aeolian Research, v. 23, p. 11-20, https://doi.org/10.1016/j.aeolia.2016.09.004.

Zheng, D., Zhang, P.Z., Wan, J., Yuan, D., et al., 2006, Rapid exhumation at ~8 Ma on the Liupan Shan thrust fault from apatite fission-track thermochronology: Implications for growth of the northeastern Tibetan Plateau margin: Earth and Planetary Science Letters, v. 248, p. 198-208, https://doi.org/10.1016/j.epsl.2006.05.023.

Table caption

Table S1: List of samples used in this study. Sample numbers with stars (*) indicate that the sample was out of the splice. Since all samples were collected from IODP Site 1425 Hole D, the stratigraphic position of the sample out of the splice was projected to the corresponding horizon on the splice based on the core photograph, and the revised core splice depth below the sea floor (m CCSF-D_Patched_rev20170309) was calculated. Linear sedimentation rates (cm/ky) and dry bulk density (g/cm^3) at each sample horizon are also shown.

Table S2: List of potential detrital source materials from the Taklimakan Desert, Mongolian Gobi Desert, Ordos Plateau, and Japanese islands.

Table S3: Peak intensities (cps) of minerals, illite FWHM (Δ °2θ) and illite chemical index ratio of 5 Å/10 Å peak areas identified by powder X-ray diffraction (XRD) in the silt and clay fractions.

Table S4: Contents (%) of silt (>4 μm) and clay (<4 μm) in dry sediment sample, and contribution (%) of each end-member in silt and clay fractions estimated by PARAFAC modelling. End-member contributions are expressed as the average and standard deviation of 20 times trial of PARAFAC calculation.

List of Appendix

Appendix 1: The PARAFAC modelling steps, matrix calculation and RSS comparison.

Table S1: List of samples used in this study. Sample numbers with stars (*) indicate that the sample was out of the splice. Since all samples were collected from IODP Site 1425 Hole D, the stratigraphic position of the sample out of the splice was projected to the corresponding horizon on the splice based on the core photograph, and the revised core splice depth below the sea floor (m CCSF-D_Patched_rev20170309) was calculated. Linear sedimentation rates (cm/ky) and dry bulk density (g/cm^3) at each sample horizon are also shown.

Sample Number	Exp	Site	Hole	Core	Type	Sect	Offset (cm)	Projected sample position in splice					CCSF-D_Patched (m) (Irino et al. 2018)	Age (Ma)	Sedimentation rates (cm/ky)	Dry bulk density (g/cm^3)
Based on the age-depth model of Tada et al. (2018) for the Pleistocene (0-1.45 Ma)																
								Hole	Core	Type	Sect	Offset (cm)				
1	346	U1425	D	1	H	1	2						0.020	0.000	5.233	0.407
2	346	U1425	D	1	H	2	57						2.070	0.031	6.759	0.683
3*	346	U1425	D	1	H	3	101	B	1	H	3	101	4.012	0.070	4.971	0.670
4*	346	U1425	D	2	H	1	1	B	1	H	5	26	6.262	0.110	5.545	0.465
5	346	U1425	D	2	H	2	54						8.405	0.162	4.113	0.784
6	346	U1425	D	2	H	3	100						10.365	0.203	4.804	0.555
7	346	U1425	D	2	H	5	0						12.365	0.241	5.285	0.529
8	346	U1425	D	2	H	6	52						14.385	0.294	3.818	0.910
9*	346	U1425	D	3	H	1	88	B	2	H	5	94	16.296	0.347	3.614	0.781
10*	346	U1425	D	3	H	2	50	B	2	H	6	83	17.686	0.387	3.467	0.667
11	346	U1425	D	3	H	3	101						19.602	0.434	4.046	0.927
12	346	U1425	D	3	H	5	1						21.602	0.481	4.315	0.849
13*	346	U1425	D	3	H	6	50	B	3	H	3	71	23.594	0.543	3.204	0.893
14*	346	U1425	D	4	H	1	18	B	3	H	5	102	26.904	0.629	3.836	0.727
15	346	U1425	D	4	H	2	51						28.738	0.668	4.722	0.831
16	346	U1425	D	4	H	3	100						30.728	0.728	3.332	0.816
17	346	U1425	D	4	H	5	0						32.728	0.783	3.588	0.797
18	346	U1425	D	4	H	6	51						34.738	0.845	3.253	0.724
19*	346	U1425	D	5	H	1	28	B	4	H	5	138	37.475	0.924	3.490	0.852
20*	346	U1425	D	5	H	2	50	B	4	H	7	15	39.055	0.955	5.031	0.809
21	346	U1425	D	5	H	3	100						41.057	1.002	4.295	0.590
22	346	U1425	D	5	H	5	0						43.057	1.058	3.570	0.875
23	346	U1425	D	5	H	6	50						45.057	1.114	3.562	0.987
24*	346	U1425	D	6	H	1	0	B	5	H	5	106	47.056	1.179	3.049	0.958
25	346	U1425	D	6	H	2	50						48.950	1.232	3.576	0.766
26	346	U1425	D	6	H	3	100						50.940	1.293	3.301	0.976
27*	346	U1425	D	6	H	5	0	B	6	H	2	20	52.887	1.369	2.535	0.446
28*	346	U1425	D	6	H	6	50	B	6	H	3	66	54.847	1.458	2.221	0.742
Based on the age-depth model of Kurokawa et al. (2019) for the Pleistocene-late Miocene (1.5-9.21 Ma)																
29*	346	U1425	D	7	H	1	0	B	6	H	5	69	57.877	1.566	2.789	0.880
30*	346	U1425	D	7	H	2	50	B	6	H	6	142	60.107	1.625	3.795	0.938
31	346	U1425	D	7	H	3	100						61.983	1.675	3.735	0.920
32	346	U1425	D	7	H	5	4						64.023	1.742	3.072	0.985
33	346	U1425	D	7	H	6	50						65.983	1.805	3.093	1.086
34*	346	U1425	D	8	H	1	100	B	7	H	6	18	68.945	1.889	3.527	0.653
35*	346	U1425	D	8	H	2	50	B	7	H	6	100	69.765	1.913	3.482	0.775
36	346	U1425	D	8	H	3	101						71.776	1.970	3.475	0.896
37	346	U1425	D	8	H	5	2						73.396	2.015	3.666	0.781
38*	346	U1425	D	8	H	6	50	B	8	H	2	148	74.896	2.055	3.759	0.824
39#	346	U1425	D	9	H	1	0	#	Slump							0.798
40#	346	U1425	D	9	H	2	50	#	Slump							0.625
41*	346	U1425	D	9	H	3	101	B	8	H	7	14	81.316	2.309	2.242	0.591
42	346	U1425	D	9	H	5	1						83.345	2.385	2.655	0.755
43*	346	U1425	D	9	H	6	50	B	9	H	3	1	85.511	2.443	3.737	0.904
44*	346	U1425	D	10	H	1	100	B	9	H	4	50	87.501	2.499	3.600	0.542
45	346	U1425	D	10	H	2	51						88.417	2.524	3.559	0.616
46	346	U1425	D	10	H	3	101						90.417	2.588	3.139	0.896
47	346	U1425	D	10	H	5	1						92.417	2.656	2.957	0.673
48	346	U1425	D	10	H	6	51						93.597	2.697	2.892	0.634
49*	346	U1425	D	11	H	1	30	B	10	H	5	10	94.903	2.739	3.058	0.590
50*	346	U1425	D	11	H	2	50	B	10	H	5	147	96.273	2.777	3.659	0.475

51	346	U1425	D	11	H	3	101						98.413	2.842	3.281	0.561
52	346	U1425	D	11	H	5	1						100.413	2.916	2.706	0.555
53	346	U1425	D	11	H	6	51						102.413	2.990	2.706	0.668
54*	346	U1425	D	12	H	1	0	B	11	H	4	130	104.918	3.071	3.098	0.521
55	346	U1425	D	12	H	2	51						106.995	3.140	3.000	0.665
56	346	U1425	D	12	H	3	96						108.945	3.209	2.838	0.683
57	346	U1425	D	13	X	1	51						110.159	3.249	2.992	0.410
58	346	U1425	D	13	X	3	51						113.159	3.353	2.881	0.588
59*	346	U1425	D	13	X	5	50	B	14	H	4	10	115.902	3.465	2.454	0.736
60*	346	U1425	D	13	X	7	50	B	14	H	6	83	119.632	3.612	2.543	0.661
61*	346	U1425	D	14	H	1	50	B	14	H	6	144	120.242	3.630	3.407	0.619
62	346	U1425	D	14	H	3	50						123.268	3.718	3.432	0.591
63*	346	U1425	D	15	H	1	50	B	17	H	2	85	124.461	3.752	3.462	0.675
64	346	U1425	D	15	H	3	50						127.130	3.836	3.191	0.595
65	346	U1425	D	15	H	5	50						130.130	3.941	2.864	0.622
66*	346	U1425	D	15	H	7	50	B	19	H	1	58	133.419	4.056	2.856	0.687
67	346	U1425	D	16	H	1	50						134.821	4.093	3.760	0.673
68	346	U1425	D	16	H	3	53						137.871	4.159	4.615	0.658
69	346	U1425	D	16	H	5	53						140.871	4.224	4.615	0.581
70*	346	U1425	D	16	H	7	50	B	21	H	2	29	143.958	4.300	4.061	0.588
71*	346	U1425	D	18	H	1	50	B	21	H	2	140	145.068	4.336	3.067	0.470
72*	346	U1425	D	18	H	3	50	B	21	H	4	123	147.898	4.418	3.487	0.483
73	346	U1425	D	18	H	5	50						152.274	4.523	4.161	0.467
74*	346	U1425	D	18	H	7	50	B	22	H	2	102	155.248	4.615	3.233	0.521
75*	346	U1425	D	19	H	1	50	B	22	H	3	82	156.548	4.654	3.346	0.470
76	346	U1425	D	19	H	3	50						160.099	4.748	3.755	0.449
77	346	U1425	D	19	H	5	50						163.099	4.828	3.738	0.653
78*	346	U1425	D	19	H	7	50	B	23	H	3	50	166.068	4.901	4.083	0.628
79*	346	U1425	D	20	H	1	50	B	23	H	3	123	166.798	4.922	3.584	0.538
80*	346	U1425	D	20	H	3	50	B	23	H	5	80	169.368	4.993	3.584	0.575
81	346	U1425	D	20	H	5	51						172.902	5.101	3.267	0.521
82*	346	U1425	D	20	H	7	50	B	24	H	2	140	175.800	5.191	3.231	0.544
83*	346	U1425	D	21	H	1	70	B	24	H	3	90	176.800	5.219	3.629	0.527
84	346	U1425	D	21	H	3	50						179.491	5.283	4.174	0.544
85	346	U1425	D	21	H	5	50						182.491	5.355	4.162	0.555
86*	346	U1425	D	22	H	1	50	B	25	H	3	10	185.540	5.432	3.950	0.461
87*	346	U1425	D	22	H	3	50	B	25	H	5	40	188.840	5.515	4.011	0.432
88	346	U1425	D	22	H	5	51						192.749	5.598	4.674	0.486
89*	346	U1425	D	22	H	7	50	B	26	H	2	60	195.605	5.641	6.684	0.572
90*	346	U1425	D	23	H	1	50	B	26	H	2	120	196.205	5.650	6.684	0.572
91	346	U1425	D	23	H	3	50						199.085	5.708	4.994	0.585
92	346	U1425	D	23	H	5	50						202.085	5.782	4.056	0.647
93*	346	U1425	D	23	H	7	50	B	27	H	2	115	204.732	5.856	3.573	0.520
94*	346	U1425	D	24	H	1	50	B	27	H	3	80	205.882	5.887	3.728	0.536
95*	346	U1425	D	24	H	3	50	B	27	H	5	90	208.982	5.970	3.722	0.551
96	346	U1425	D	24	H	5	51						212.306	6.066	3.444	0.474
97*	346	U1425	D	24	H	7	54	B	28	H	2	117	215.048	6.149	3.300	0.631
98*	346	U1425	D	25	H	1	50	B	28	H	3	116	216.538	6.186	4.022	0.638
99	346	U1425	D	25	H	3	50						219.683	6.266	3.964	0.555
100*	346	U1425	D	26	X	1	50	B	29	H	1	40	221.573	6.319	3.541	0.555
101*	346	U1425	D	26	X	3	50	B	29	H	3	20	224.373	6.400	3.467	0.671
102*	346	U1425	D	26	X	5	50	B	29	H	5	20	227.373	6.479	3.794	0.678
103*	346	U1425	D	26	X	7	50	B	29	H	6	100	229.673	6.531	4.460	0.590
104	346	U1425	D	27	H	1	50						230.266	6.545	4.240	0.677
105	346	U1425	D	27	H	3	50						233.266	6.616	4.216	0.655
106*	346	U1425	D	28	H	1	50	B	30	H	3	70	234.612	6.639	5.666	0.690
107*	346	U1425	D	28	H	3	51	B	30	H	5	0	236.912	6.671	7.217	0.585
108	346	U1425	D	28	H	5	51						240.338	6.719	7.217	0.652
109	346	U1425	D	28	H	7	50						242.828	6.763	5.621	0.566
110	346	U1425	D	29	H	1	50						244.270	6.791	5.204	0.624
111*	346	U1425	D	29	H	3	50	B	33	H	2	130	247.622	6.863	4.616	0.607
112*	346	U1425	D	30	H	1	50	B	33	H	4	10	249.422	6.906	4.198	0.527
113*	346	U1425	D	30	H	3	50	B	33	H	6	50	252.822	7.004	3.486	0.625
114	346	U1425	D	30	H	5	51						255.979	7.109	3.012	0.683
115*	346	U1425	D	30	H	7	50	B	34	H	3	80	258.059	7.191	2.533	0.638

116*	346	U1425	D	31	H	1	0	B	34	H	3	120	258.459	7.207	2.507	0.567
117*	346	U1425	D	31	H	2	50	B	34	H	5	48	260.739	7.283	3.010	0.662
118	346	U1425	D	31	H	3	100						263.551	7.366	3.365	0.755
119	346	U1425	D	31	H	5	0						265.551	7.424	3.442	0.729
120*	346	U1425	D	31	H	6	50	B	35	H	3	70	267.448	7.479	3.432	0.680
121*	346	U1425	D	32	H	1	50	B	35	H	4	80	269.048	7.530	3.167	0.741
122	346	U1425	D	32	H	2	51						271.676	7.601	3.706	0.646
123	346	U1425	D	32	H	3	50						273.166	7.631	4.875	0.714
124	346	U1425	D	32	H	5	49						276.156	7.707	3.948	0.514
125	346	U1425	D	32	H	6	51						277.676	7.749	3.625	0.588
126*	346	U1425	D	33	H	1	50	B	37	H	1	110	280.040	7.816	3.518	0.668
127*	346	U1425	D	33	H	2	50	B	37	H	2	60	281.040	7.845	3.515	0.748
128*	346	U1425	D	33	H	4	50	B	37	H	3	70	282.640	7.891	3.484	0.558
129*	346	U1425	D	35	H	1	6	B	38	H	2	10	284.781	7.952	3.511	0.652
130	346	U1425	D	35	H	2	50						288.239	8.040	3.925	0.795
131	346	U1425	D	35	H	3	54						289.779	8.073	4.644	0.733
132*	346	U1425	D	36	H	1	50	B	39	H	2	120	291.166	8.102	4.778	0.675
133	346	U1425	D	36	H	2	50						294.486	8.172	4.746	0.705
134	346	U1425	D	36	H	3	50						295.986	8.204	4.723	0.603
135	346	U1425	D	37	H	1	0						297.407	8.233	4.841	0.401
136	346	U1425	D	37	H	2	51						298.928	8.260	5.570	0.625
137	346	U1425	D	37	H	4	50						300.908	8.296	5.570	0.661
138	346	U1425	D	37	H	5	50						302.408	8.323	5.570	0.603
139	346	U1425	D	37	H	7	54						304.628	8.373	4.451	0.708
140*	346	U1425	D	38	H	1	50	B	42	H	2	110	306.292	8.414	4.050	0.702
141	346	U1425	D	38	H	2	50						307.584	8.445	4.159	0.658
142*	346	U1425	D	38	H	3	54	B	43	H	1	104	309.432	8.482	4.926	0.649
143	346	U1425	D	39	H	1	50						311.281	8.520	4.926	0.767
144	346	U1425	D	39	H	2	50						312.781	8.552	4.742	0.527
145	346	U1425	D	39	H	3	54						314.321	8.584	4.699	0.550
146	346	U1425	D	40	H	1	50						317.760	8.671	3.950	0.675
147	346	U1425	D	40	H	2	51						319.270	8.715	3.501	0.807
148	346	U1425	D	40	H	3	100						321.260	8.768	3.716	0.587
149*	346	U1425	D	41	H	1	50	B	46	H	1	39	321.714	8.780	3.751	0.532
150	346	U1425	D	41	H	2	50						323.255	8.821	3.751	0.532
151	346	U1425	D	41	H	3	50						324.755	8.855	4.501	0.619
152*	346	U1425	D	42	H	1	50	B	47	H	1	50	326.423	8.891	4.543	0.687
153*	346	U1425	D	42	H	2	50	B	47	H	2	50	327.923	8.921	4.970	0.687
154*	346	U1425	D	42	H	3	54	B	47	H	3	54	329.463	8.946	6.270	0.821
155	346	U1425	D	43	H	1	50						330.563	8.964	6.270	0.588
156	346	U1425	D	43	H	2	50						332.063	8.987	6.270	0.578
157	346	U1425	D	43	H	3	54						333.603	9.012	6.292	0.637
158	346	U1425	D	43	H	5	1						336.073	9.051	6.402	0.634
159	346	U1425	D	43	H	6	50						338.063	9.082	6.402	0.727
160*	346	U1425	D	44	H	1	50	B	49	H	3	50	340.542	9.121	6.222	0.824
161	346	U1425	D	44	H	2	50						342.031	9.147	5.779	0.714
162	346	U1425	D	44	H	3	50						343.531	9.173	5.779	0.647
163	346	U1425	D	45	H	1	0	B	50	H	3	24	345.891	9.214	5.778	0.692
Based on tie point of Kamikuri et al. (2017) for the late Miocene (9.22-9.7 Ma)																
164	346	U1425	D	45	H	2	51						347.937	9.254	5.144	0.773
165	346	U1425	D	45	H	3	54						349.467	9.284	5.144	0.878
166*	346	U1425	D	46	H	1	50	B	51	H	2	140	351.155	9.316	5.144	0.702
167*	346	U1425	D	46	H	2	50	B	51	H	4	60	352.855	9.349	5.144	0.853
168	346	U1425	D	46	H	3	50						354.127	9.374	5.144	0.963
169	346	U1425	D	47	H	1	0						355.327	9.397	5.144	0.938
170	346	U1425	D	47	H	2	49						357.317	9.436	5.144	1.034
171	346	U1425	D	47	H	3	54						358.867	9.466	5.144	0.969
172	346	U1425	D	48	H	1	50						360.527	9.499	5.144	0.853
173	346	U1425	D	48	H	2	51						362.037	9.528	5.144	0.880
175	346	U1425	D	49	H	1	23						362.257	9.532	5.144	0.884
174	346	U1425	D	48	H	3	54						363.567	9.558	5.144	0.904
176	346	U1425	D	49	H	2	50						364.027	9.567	5.144	0.985
177	346	U1425	D	49	H	3	99						366.017	9.605	5.144	1.022
178	346	U1425	D	50	H	1	50						367.227	9.629	5.144	1.098
179	346	U1425	D	50	H	2	48						368.707	9.658	5.144	1.124
180	346	U1425	D	50	H	3	50						370.227	9.687	5.144	1.092

*Projection age model from Hole B, U1425.

#Slump samples, not include in the age model calculation

Table S2: List of potential detrital source materials from the Taklimakan Desert, Mongolian Gobi Desert, Ordos Plateau, and Japanese islands.

Region	Sample number	Latitude	Longitude
Gobi Desert			
	GB07-51	41°16′08.9″N	99°28′19.2″E
	GB07-52	40°53′20.2″N	99°23′15.5″E
	HT07-125	43°03′39.9″N	90°45′38.9″E
	HT07-124	42°55′03.5″N	89°46′08.5″E
	HT07-129	42°58′38.5″N	93°15′54.3″E
TG-Tengger Desert			
	TG07-36	39°08′17.1″N	105°39′17.6″E
Ordos Plateau			
	MU07-05	38°28′05.7″N	108°48′31.4″E
	MU07-10	39°24′44.9″N	108°57′30.9″E
	HB07-17	40°41′19.2″N	108°32′30.8″E
	HB07-18	40°47′46.5″N	108°15′18.8″E
	UB07-27	40°48′01.7″N	106°33′38.6″E
Jingyuan (JY)			
	JY1	36°21'00.0"N	104°36'00.0"E
	JY7	36°21'00.0"N	104°36'00.0"E
	JY13	36°21'00.0"N	104°36'00.0"E
Qilian Mountains			
	GL07-143	37°27′06.4″N	102°53′19.7″E
Taklimakan			
	TK07-116	38°45′21.9″N	87°30′21.1″E
	TK07-119	39°59′30.3″N	88°21′51.1″E
	TAK06-12	37°25'21.4"N	77°13'29.0"E
	TAK06-17	38°52'08.7"N	76°14'18.2"E
	TAK06-29	39°48'54.3"N	77°27'48.4"E
	TAK06-35	41°21'27.1"N	80°43'42.2"E
	KL10-03	37°16'07.8"N	77°51'41.4"E
	KKR10-02	37°00'57.8"N	79°43'46.3"E
Tian Shan Mountains			
	TS10-09	41°51'33.4"N	82°45'17.6"E
	TS10-11	41°29'18.5"N	84°05'32.1"E
	TS10-12	41°44'23.9"N	85°04'17.4"E
	TS10-13	42°10'04.7"N	86°11'56.7"E
Japan Island			
	MC02	36°12'15.82"N	135°29'16.69"E
	MC04	35°49'50.17"N	134°59'58.05"E
	MC05	36° 3'15.12"N	135°40'20.91"E
	MC07	35°46'3.18"N	135°24'33.08"E
	MC08	35°51'2.23"N	135°28'2.28"E
	KT94-15 PC9	39°34'21.60"N	139°26'24.69"E

Table S3: Peak intensities (cps) of minerals, illite FWHM (Δ °2θ) and illite chemical index ratio of 5 Å/10 Å peak areas identified by powder X-ray diffraction (XRD) in the silt and clay fractions.

Samples Number	Exp	Site	Hole	Core	Type	Sect	Offset (cm)	Silt Quartz	Silt Albite	Silt Anorthite	Silt K-feldspar	Silt Illite	Silt Chlorite	Silt Kaolinite	Silt Smectite	Silt Pyrite	Silt Dolomite	Silt Diatomaceous	Silt Calcite	Silt illite FWHM (Δ °2θ)	Silt_illite 5A/10A (area)
1	346	U1425	D	1	H	1	2	1115	699	258	155	227	55	39	57	16	118	66	0	0.17	0.36
2	346	U1425	D	1	H	2	57	1060	512	257	122	252	60	20	59	130	169	21	1382	0.20	0.31
3	346	U1425	D	1	H	3	101	1278	913	388	328	245	77	18	87	82	149	26	206	0.21	0.34
4	346	U1425	D	2	H	1	1	810	592	165	147	180	82	15	79	85	103	27	1996	0.13	0.34
5	346	U1425	D	2	H	2	54	1297	878	497	265	261	84	30	78	153	112	26	0	0.21	0.30
6	346	U1425	D	2	H	3	100	1140	658	247	153	209	75	44	76	79	66	44	0	0.19	0.33
7	346	U1425	D	2	H	5	0	997	684	296	233	325	129	33	112	35	72	47	0	0.19	0.29
8	346	U1425	D	2	H	6	52	1441	778	296	156	284	103	21	93	33	127	29	0	0.20	0.33
9	346	U1425	D	3	H	1	88	1014	660	187	124	300	101	22	122	157	205	22	735	0.17	0.30
10	346	U1425	D	3	H	2	50	1210	533	264	176	281	43	15	82	199	159	26	0	0.21	0.27
11	346	U1425	D	3	H	3	101	1012	745	246	215	493	144	35	145	179	19	40	0	0.19	0.35
12	346	U1425	D	3	H	5	1	737	474	161	126	246	63	0	89	276	37	82	110	0.19	0.30
13	346	U1425	D	3	H	6	50	725	597	164	179	246	86	0	80	159	95	30	1346	0.21	0.31
14	346	U1425	D	4	H	1	18	1121	815	393	257	272	111	16	87	155	59	39	0	0.21	0.31
15	346	U1425	D	4	H	2	51	892	488	188	134	177	67	12	72	104	129	34	1347	0.23	0.29
16	346	U1425	D	4	H	3	100	892	478	318	213	223	57	39	59	155	136	35	678	0.21	0.31
17	346	U1425	D	4	H	5	0	918	495	347	253	142	53	13	55	82	94	53	0	0.22	0.30
18	346	U1425	D	4	H	6	51	673	327	158	114	148	55	9	33	86	113	20	2440	0.19	0.29
19	346	U1425	D	5	H	1	28	694	381	198	107	261	90	21	75	111	146	30	1911	0.22	0.29
20	346	U1425	D	5	H	2	50	772	429	288	194	133	49	26	43	103	109	62	0	0.20	0.32
21	346	U1425	D	5	H	3	100	567	282	219	101	102	65	16	65	181	21	63	0	0.29	0.23
22	346	U1425	D	5	H	5	0	1071	667	196	182	329	108	35	92	168	73	32	0	0.20	0.32
23	346	U1425	D	5	H	6	50	1239	771	217	432	313	84	24	67	132	197	26	0	0.19	0.32
24	346	U1425	D	6	H	1	0	474	275	139	89	133	61	9	56	42	25	130	0	0.16	0.43
25	346	U1425	D	6	H	2	50	942	652	300	207	243	86	16	88	62	88	55	0	0.22	0.30
26	346	U1425	D	6	H	3	100	1037	590	345	157	262	89	22	76	121	168	16	890	0.21	0.38
27	346	U1425	D	6	H	5	0	1042	478	342	139	242	72	22	50	150	41	55	0	0.18	0.35
28	346	U1425	D	6	H	6	50	1087	552	297	147	286	101	17	102	161	87	28	0	0.20	0.30
29	346	U1425	D	7	H	1	0	1095	677	200	188	280	97	25	85	93	109	30	381	0.22	0.34
30	346	U1425	D	7	H	2	50	587	459	131	92	98	45	17	49	126	68	90	0	0.31	0.27
31	346	U1425	D	7	H	3	100	1099	749	319	199	419	139	33	116	73	136	37	0	0.18	0.34
32	346	U1425	D	7	H	5	4	1394	966	336	213	300	99	29	94	28	125	28	0	0.19	0.38
33	346	U1425	D	7	H	6	50	573	409	368	397	268	50	15	60	51	55	50	266	0.15	0.22
34	346	U1425	D	8	H	1	100	1298	682	397	200	262	92	24	98	136	126	33	0	0.17	0.41
35	346	U1425	D	8	H	2	50	1148	698	316	235	311	114	21	105	132	112	34	0	0.20	0.33
36	346	U1425	D	8	H	3	101	1445	907	232	165	329	102	29	89	44	183	22	0	0.19	0.36
37	346	U1425	D	8	H	5	2	1303	584	283	160	236	75	17	64	106	76	40	0	0.18	0.35
38	346	U1425	D	8	H	6	50	1316	710	279	211	229	93	19	95	93	107	40	0	0.19	0.35
39	346	U1425	D	9	H	1	0	930	514	233	163	195	54	46	62	76	197	42	0	0.21	0.32
40	346	U1425	D	9	H	2	50	1061	594	148	134	186	66	21	62	100	131	46	0	0.22	0.34
41	346	U1425	D	9	H	3	101	903	424	239	10	165	55	44	50	68	14	66	0	0.17	0.34
42	346	U1425	D	9	H	5	1	1103	612	279	133	200	70	27	65	82	38	57	0	0.19	0.33
43	346	U1425	D	9	H	6	50	1329	600	328	114	307	108	26	103	88	176	28	0	0.19	0.33
44	346	U1425	D	10	H	1	100	970	429	268	114	122	43	16	37	58	31	79	0	0.21	0.26
45	346	U1425	D	10	H	2	51	1098	560	287	164	136	48	24	45	37	11	70	0	0.22	0.33
46	346	U1425	D	10	H	3	101	1260	658	247	153	301	113	22	88	131	31	43	0	0.16	0.44
47	346	U1425	D	10	H	5	1	998	491	246	99	144	56	20	65	120	43	69	0	0.22	0.31
48	346	U1425	D	10	H	6	51	832	393	235	91	79	35	20	54	82	11	94	0	0.33	0.33
49	346	U1425	D	11	H	1	30	655	294	208	102	145	33	16	50	65	17	92	0	0.18	0.33
50	346	U1425	D	11	H	2	50	256	100	74	35	46	19	31	10	16	0	249	0	0.05	0.10
51	346	U1425	D	11	H	3	101	584	237	192	57	129	90	21	42	71	0	92	0	0.26	0.41
52	346	U1425	D	11	H	5	1	362	205	126	92	88	28	24	70	42	13	181	0	0.21	0.27
53	346	U1425	D	11	H	6	51	697	421	195	120	132	53	17	36	99	48	74	0	0.22	0.31
54	346	U1425	D	12	H	1	0	421	235	119	39	77	26	27	32	51	32	167	0	0.27	0.28
55	346	U1425	D	12	H	2	51	775	441	139	120	160	62	21	61	64	11	79	0	0.24	0.33
56	346	U1425	D	12	H	3	96	628	272	174	77	107	59	21	41	47	23	75	0	0.22	0.41
57	346	U1425	D	13	X	1	51	474	232	119	59	158	79	40	76	59	59	96	0	0.21	0.34
58	346	U1425	D	13	X	3	51	317	227	112	43	74	46	28	36	60	23	133	0	0.24	0.53
59	346	U1425	D	13	X	5	50	444	266	98	48	83	65	34	50	47	67	69	0	0.31	0.37
60	346	U1425	D	13	X	7	50	428	258	142	70	62	32	34	52	57	0	94	0	0.03	0.28
61	346	U1425	D	14	H	1	50	431	184	184	57	84	39	50	51	34	15	101	0	0.21	0.44
62	346	U1425	D	14	H	3	50	528	300	201	93	59	60	21	53	58	34	108	0	0.36	0.46
63	346	U1425	D	15	H	1	50	323	194	132	64	70	36	56	42	23	20	108	0	0.25	0.39
64	346	U1425	D	15	H	3	50	441	272	137	59	98	108	30	72	38	34	108	0	0.22	0.25
65	346	U1425	D	15	H	5	50	572	360	140	104	154	59	33	40	28	33	80	0	0.18	0.30
66	346	U1425	D	15	H	7	50	343	303	328	128	119	62	0	36	53	30	103	0	0.20	0.34
67	346	U1425	D	16	H	1	50	355	191	112	56	84	28	18	49	19	34	137	0	0.19	0.40
68	346	U1425	D	16	H	3	53	410	212	132	62	79	51	29	45	34	37	105	0	0.29	0.36
69	346	U1425	D	16	H	5	53	333	130	134	64	54	33	32	28	36	21	170	0	0.25	0.61
70	346	U1425	D	16	H	7	50	322	121	91	63	74	18	28	37	44	19	171	0	0.22	0.52
71	346	U1425	D	18	H	1	50	256	117	124	40	46	41	30	52	26	0	244	0	0.28	0.41
72	346	U1425	D	18	H	3	50	290	117	58	36	79	26	32	48	37	17	211	0	0.16	0.24
73	346	U1425	D	18	H	5	50	241	50	44	40	14	15	34	45	25	14	289	0	0.08	0.17
74	346	U1425	D	18	H	7	50	449	219	84	34	58	41	33	34	39	3	223	0	0.28	0.31
75	346	U1425	D	19	H	1	50	259	79	31	26	19	18	25	36	26	14	325	0	0.24	0.31
76	346	U1425	D	19	H	3	50	359	178	110	31	52	31	25	64	37	29	217	0	0.32	0.29
77	346	U1425	D	19	H	5	50	838	433	232	109	124	55	32	59	53	36	101	0	0.22	0.44
78	346	U1425	D	19	H	7	50	480	253	187	52	84	59	20	48	29	36	112	0	0.24	0.35
79	346	U1425	D	20	H	1	50	506	297	145	67	72	36	46	68	44	15	141	0	0.23	0.32
80	346	U1425	D	20	H	3	50	271	136	71	67	114	23	40	42	13	2	274	0	0.15	0.35
81	346	U1425	D	20	H	5	51	295	116	138	42	65	48	25	56	24	26	171	0	0.24	0.41
82	346	U1425	D	20	H	7	50	289	146	88	23	26	18	27	53	50	41	212	0	0.21	0.38
83	346	U1425	D	21	H	1	70	749	344	157	67	104	30	16	71	53	18	108	0	0.18	0.37
84	346	U1425	D	21	H	3	50	368	191	107	30	41	25	38	27	48	108	135	0	0.39	0.14
85	346	U1425	D	21	H	5	50	370	178	95	29	50	21	23	21	43	15	240	0	0.19	0.13
86	346	U1425	D	22	H	1	50	230	96	34	44	34	16	30	51	25	0	315	0	0.11	0.28
87	346	U1425	D	22	H	3	50	191	75	61	80	41	0	25	39	37	24	287	0	0.08	0.44
88	346	U1425	D	22	H	5	51	399	202	97	49	53	22	0	37	34	16	218	0	0.22	0.26
89	346	U1425	D	22	H	7	50	321	213	90	50	68	40	18	52	55	20	133	0	0.32	0.19
90	346	U1425	D	23	H	1	50	655	389	169	78	130	42	49	52	71	15	114	0	0.17	0.31

91	346	U1425	D	23	H	3	50	402	275	266	114	74	20	21	59	44	0	144	0	0.19	0.37
92	346	U1425	D	23	H	5	50	563	280	193	81	93	20	21	55	78	19	141	0	0.22	0.30
93	346	U1425	D	23	H	7	50	282	120	57	42	46	16	29	29	25	12	290	0	0.21	0.26
94	346	U1425	D	24	H	1	50	204	67	68	40	36	30	43	31	21	19	262	0	0.08	0.05
95	346	U1425	D	24	H	3	50	452	266	132	62	98	35	20	66	112	23	100	0	0.13	0.66
96	346	U1425	D	24	H	5	51	212	72	64	19	31	14	30	49	33	0	373	0	0.11	0.02
97	346	U1425	D	24	H	7	54	358	204	132	51	51	36	32	37	87	15	111	0	0.46	0.22
98	346	U1425	D	25	H	1	50	213	70	44	20	34	14	24	30	34	17	285	0	0.19	0.25
99	346	U1425	D	25	H	3	50	255	209	147	41	28	24	20	38	34	18	245	0	0.45	0.11
100	346	U1425	D	26	X	1	50	512	248	281	56	82	66	0	53	39	0	106	0	0.26	0.64
101	346	U1425	D	26	X	3	50	430	226	83	35	55	37	33	55	73	17	154	0	0.26	0.36
102	346	U1425	D	26	X	5	50	282	129	103	80	85	32	30	47	68	10	162	0	0.06	0.36
103	346	U1425	D	26	X	7	50	325	198	55	23	50	41	17	34	67	18	130	0	0.21	0.47
104	346	U1425	D	27	H	1	50	490	204	201	40	62	48	15	39	99	10	114	0	0.28	0.30
105	346	U1425	D	27	H	3	50	425	196	178	40	85	64	23	64	87	24	85	0	0.19	0.42
106	346	U1425	D	28	H	1	50	312	164	162	34	70	16	19	34	93	0	157	0	0.05	0.53
107	346	U1425	D	28	H	3	51	452	221	145	57	81	37	31	61	130	0	109	0	0.18	0.35
108	346	U1425	D	28	H	5	51	410	194	250	41	64	73	48	48	105	15	122	0	0.37	0.20
109	346	U1425	D	28	H	7	50	260	135	66	29	48	36	39	58	95	23	212	0	0.15	0.07
110	346	U1425	D	29	H	1	50	578	211	268	47	86	29	59	51	191	15	98	0	0.16	0.42
111	346	U1425	D	29	H	3	50	198	81	69	25	34	0	0	50	66	0	252	0	0.22	0.15
112	346	U1425	D	30	H	1	50	303	172	138	48	56	35	17	50	149	28	132	0	0.26	0.49
113	346	U1425	D	30	H	3	50	676	315	308	82	124	29	23	69	190	17	104	0	0.21	0.36
114	346	U1425	D	30	H	5	51	602	310	243	112	87	33	15	45	131	23	103	0	0.20	0.22
115	346	U1425	D	30	H	7	50	387	208	213	94	48	65	26	42	149	28	177	0	0.33	0.40
116	346	U1425	D	31	H	1	0	269	139	92	47	103	31	25	38	92	14	191	0	0.42	0.45
117	346	U1425	D	31	H	2	50	456	217	181	49	64	29	23	44	199	17	120	0	0.19	0.60
118	346	U1425	D	31	H	3	100	352	199	150	74	75	73	20	53	121	14	87	0	0.44	0.38
119	346	U1425	D	31	H	5	0	595	278	173	70	92	58	26	50	137	40	72	0	0.25	0.41
120	346	U1425	D	31	H	6	50	448	260	194	67	57	69	17	39	159	27	89	0	0.38	0.35
121	346	U1425	D	32	H	1	50	380	258	144	57	17	37	22	38	189	0	198	0	0.12	0.33
122	346	U1425	D	32	H	2	51	321	217	91	61	44	34	31	51	193	26	234	0	0.22	0.40
123	346	U1425	D	32	H	3	50	473	318	238	67	24	36	16	61	198	27	105	0	0.22	0.63
124	346	U1425	D	32	H	5	49	330	153	134	33	56	31	40	29	79	26	254	0	0.21	0.32
125	346	U1425	D	32	H	6	51	421	205	115	37	91	39	37	36	178	4	177	0	0.18	0.34
126	346	U1425	D	33	H	1	50	414	223	126	79	62	45	14	50	117	22	80	0	0.29	0.35
127	346	U1425	D	33	H	2	50	478	277	186	61	55	64	0	71	150	11	83	0	0.46	0.26
128	346	U1425	D	33	H	4	50	320	228	134	45	32	20	23	40	271	23	142	0	0.46	0.47
129	346	U1425	D	35	H	1	6	217	54	38	19	75	29	50	30	58	15	284	0	0.14	0.20
130	346	U1425	D	35	H	2	50	380	204	138	67	73	118	14	86	49	18	69	0	0.36	0.22
131	346	U1425	D	35	H	3	54	329	170	106	38	45	53	25	61	95	0	107	0	0.14	0.68
132	346	U1425	D	36	H	1	50	292	152	118	29	50	56	17	47	101	12	122	0	0.47	0.19
133	346	U1425	D	36	H	2	50	344	179	141	48	74	120	19	76	107	16	92	0	0.39	0.20
134	346	U1425	D	36	H	3	50	345	185	108	62	59	77	21	61	79	18	81	0	0.23	0.45
135	346	U1425	D	37	H	1	0	377	218	144	78	108	138	26	110	72	16	80	0	0.19	0.27
136	346	U1425	D	37	H	2	51	485	276	146	78	76	71	34	62	204	3	79	0	0.28	0.24
137	346	U1425	D	37	H	4	50	335	168	110	102	63	152	21	66	73	12	104	0	0.19	0.64
138	346	U1425	D	37	H	5	50	333	200	135	49	57	38	35	40	103	18	214	0	0.23	0.39
139	346	U1425	D	37	H	7	54	399	88	94	50	65	101	27	76	145	14	100	0	0.39	0.25
140	346	U1425	D	38	H	1	50	282	132	97	75	41	56	27	43	88	0	142	0	0.51	0.67
141	346	U1425	D	38	H	2	50	268	173	119	41	43	104	25	66	62	7	133	0	0.39	0.47
142	346	U1425	D	38	H	3	54	396	193	146	55	66	82	30	72	79	11	81	0	0.38	0.31
143	346	U1425	D	39	H	1	50	351	207	80	49	49	84	22	50	41	13	79	0	0.66	0.43
144	346	U1425	D	39	H	2	50	225	108	54	41	30	30	32	22	51	21	217	0	0.58	0.48
145	346	U1425	D	39	H	3	54	262	110	69	31	35	25	34	50	131	0	140	0	0.14	0.20
146	346	U1425	D	40	H	1	50	311	176	136	70	97	85	29	64	127	3	92	0	0.14	0.70
147	346	U1425	D	40	H	2	51	405	206	143	70	68	93	18	67	58	17	82	0	0.39	0.18
148	346	U1425	D	40	H	3	100	305	155	136	66	57	33	40	65	111	25	119	0	0.45	0.44
149	346	U1425	D	41	H	1	50	223	89	97	43	35	32	31	71	97	13	165	0	0.26	0.45
150	346	U1425	D	41	H	2	50	327	158	150	59	58	24	35	61	101	19	91	0	0.64	0.17
151	346	U1425	D	41	H	3	50	248	174	78	37	39	76	28	66	90	0	115	0	0.17	0.30
152	346	U1425	D	42	H	1	50	318	137	161	59	67	69	28	85	92	15	96	0	0.25	0.27
153	346	U1425	D	42	H	2	50	322	172	178	66	76	50	8	59	109	0	84	0	0.32	0.25
154	346	U1425	D	42	H	3	54	425	217	168	104	73	57	0	42	119	27	86	0	0.32	0.25
155	346	U1425	D	43	H	1	50	283	135	102	32	45	41	40	65	66	21	222	0	0.29	0.40
156	346	U1425	D	43	H	2	50	329	118	154	25	40	69	25	55	116	15	140	0	0.25	0.69
157	346	U1425	D	43	H	3	54	245	138	105	43	34	67	23	50	65	15	162	0	0.44	0.53
158	346	U1425	D	43	H	5	1	280	194	117	40	66	46	15	58	120	16	129	0	0.17	0.17
159	346	U1425	D	43	H	6	50	313	158	132	56	49	79	24	65	107	2	106	0	0.49	0.59
160	346	U1425	D	44	H	1	50	437	269	291	95	58	59	52	72	223	0	84	0	0.40	0.25
161	346	U1425	D	44	H	2	50	341	222	219	50	47	55	27	32	209	17	133	0	0.22	0.70
162	346	U1425	D	44	H	3	50	253	119	122	25	38	48	36	26	101	24	186	0	0.25	0.31
163	346	U1425	D	45	H	1	0	539	271	214	61	76	47	19	51	148	8	135	0	0.15	0.58
164	346	U1425	D	45	H	2	51	432	218	195	63	51	49	18	49	84	32	133	0	0.28	0.42
165	346	U1425	D	45	H	3	54	411	257	168	82	50	94	35	45	66	8	81	0	0.74	0.19
166	346	U1425	D	46	H	1	50	299	222	150	50	79	110	0	37	118	49	137	0	0.09	0.05
167	346	U1425	D	46	H	2	50	389	190	172	101	76	118	14	81	23	0	75	0	0.37	0.29
168	346	U1425	D	46	H	3	50	363	210	154	78	73	64	0	76	29	43	75	0	0.45	0.27
169	346	U1425	D	47	H	1	0	357	186	196	88	92	153	23	72	21	18	75	0	0.22	0.31
170	346	U1425	D	47	H	2	49	345	222	144	94	75	59	33	77	54	14	148	0	0.52	0.20
171	346	U1425	D	47	H	3	54	491	153	111	37	41	61	0	66	26	0	204	0	0.30	0.48
172	346	U1425	D	48	H	1	50	466	205	139	69	85	85	15	69	27	0	143	0	0.30	0.29
173	346	U1425	D	48	H	2	51	436	262	223	88	117	102	16	105	52	16	118	0	0.34	0.28
174	346	U1425	D	49	H	1	23	464	151	129	53	75	64	15	55	74	16	219	0	0.28	0.05
175	346	U1425	D	48	H	3	54	395	258	129	99	97	97	27	64	40	21	115	0	0.39	0.48
176	346	U1425	D	49	H	2	50	341	202	107	47	56	64	0	62	62	0	215	0	0.18	0.31
177	346	U1425	D	49	H	3	99	484	245	136	100	67	63	4	56	64	18	126	0	0.26	0.31
178	346	U1425	D	50	H	1	50	420	248	214	105	73	141	20	92	46	7	61	0	0.43	0.14
179	346	U1425	D	50	H	2	48	408	291	173	112	99	136	18	70	81	11	64	0	0.16	0.28
180	346	U1425	D	50	H	3	50	449	264	178	84	100	54	0	65	117	11	61	0	0.49	0.24

Samples Number	Exp	Site	Hole	Core	Type	Sect	Offset (cm)	Clay Quartz	Clay Albite	Clay Anorthite	Clay K-feldspar	Clay Illite	Clay Chlorite	Clay Kaolinite	Clay Smectite	Clay Pyrite	Clay Dolomite	Clay Diatomaceous	Clay Calcite	Clay illite FWHM (Δ °2θ)	Clay_illite 5A/10A (area)
1	346	U1425	D	1	H	1	2	399	264	161	63	215	139	44	104	0	34	76	0	0.29	0.53
2	346	U1425	D	1	H	2	57	509	349	151	96	457	281	108	217	44	90	46	235	0.18	0.30
3	346	U1425	D	1	H	3	101	442	342	153	119	335	164	51	161	26	57	52	0	0.28	0.26
4	346	U1425	D	2	H	1	1	433	252	121	110	317	161	49	161	13	62	52	840	0.26	0.29
5	346	U1425	D	2	H	2	54	522	330	179	126	384	273	67	174	43	32	50	0	0.30	0.29
6	346	U1425	D	2	H	3	100	465	276	196	95	277	106	40	130	30	10	68	525	0.26	0.27
7	346	U1425	D	2	H	5	0	437	255	166	121	255	148	37	124	19	36	69	0	0.32	0.24
8	346	U1425	D	2	H	6	52	622	345	196	131	567	394	91	167	15	50	52	0	0.10	0.73
9	346	U1425	D	3	H	1	88	495	306	147	100	396	227	87	124	11	78	47	742	0.28	0.26
10	346	U1425	D	3	H	2	50	505	349	153	123	418	284	103	162	18	41	56	0	0.33	0.27
11	346	U1425	D	3	H	3	101	394	273	121	109	265	134	65	100	219	47	50	0	0.26	0.30
12	346	U1425	D	3	H	5	1	284	164	111	59	239	120	71	113	0	28	119	0	0.26	0.26
13	346	U1425	D	3	H	6	50	351	229	119	78	329	159	67	91	49	51	59	748	0.23	0.36
14	346	U1425	D	4	H	1	18	345	224	147	82	231	156	53	123	303	0	55	0	0.37	0.26
15	346	U1425	D	4	H	2	51	423	266	143	121	329	173	66	158	0	5	53	527	0.33	0.27
16	346	U1425	D	4	H	3	100	423	236	156	88	373	218	90	100	19	63	61	179	0.24	0.33
17	346	U1425	D	4	H	5	0	469	261	172	96	421	222	53	182	14	42	63	0	0.28	0.20
18	346	U1425	D	4	H	6	51	347	236	98	93	338	175	54	100	20	70	55	1149	0.35	0.30
19	346	U1425	D	5	H	1	28	345	234	113	88	367	208	60	135	0	59	54	1442	0.25	0.71
20	346	U1425	D	5	H	2	50	428	305	176	127	503	259	104	98	11	41	68	0	0.31	0.28
21	346	U1425	D	5	H	3	100	335	231	164	92	140	92	14	53	24	20	82	0	0.31	0.27
22	346	U1425	D	5	H	5	0	424	306	163	113	318	201	62	124	36	30	58	0	0.33	0.27
23	346	U1425	D	5	H	6	50	496	285	190	124	388	205	96	198	18	73	51	0	0.34	0.27
24	346	U1425	D	6	H	1	0	185	127	74	47	93	75	40	27	0	4	146	0	0.32	0.29
25	346	U1425	D	6	H	2	50	423	293	161	103	371	198	41	118	0	16	78	0	0.30	0.29
26	346	U1425	D	6	H	3	100	503	297	144	132	407	212	83	129	0	73	46	720	0.25	0.34
27	346	U1425	D	6	H	5	0	425	253	160	105	429	218	82	139	41	34	88	0	0.27	0.35
28	346	U1425	D	6	H	6	50	548	300	183	110	585	287	101	186	14	45	48	0	0.26	0.33
29	346	U1425	D	7	H	1	0	465	280	161	109	310	154	56	98	0	54	53	537	0.32	0.27
30	346	U1425	D	7	H	2	50	326	240	132	104	221	109	49	109	0	43	78	0	0.32	0.27
31	346	U1425	D	7	H	3	100	391	237	151	87	281	154	56	93	0	54	64	0	0.20	0.22
32	346	U1425	D	7	H	5	4	566	392	176	121	561	341	110	153	8	26	52	0	0.28	0.29
33	346	U1425	D	7	H	6	50	401	235	119	110	280	134	33	93	0	49	59	197	0.35	0.29
34	346	U1425	D	8	H	1	100	535	316	170	153	474	271	73	178	0	40	56	0	0.29	0.28
35	346	U1425	D	8	H	2	50	453	297	147	86	319	176	64	137	18	217	62	0	0.32	0.26
36	346	U1425	D	8	H	3	101	564	289	179	100	547	337	105	203	12	71	51	0	0.28	0.31
37	346	U1425	D	8	H	5	2	412	271	149	104	416	219	79	130	6	24	91	0	0.27	0.30
38	346	U1425	D	8	H	6	50	458	278	145	92	357	192	65	129	0	32	75	0	0.28	0.27
39	346	U1425	D	9	H	1	0	357	255	122	86	307	146	41	141	0	72	78	0	0.30	0.28
40	346	U1425	D	9	H	2	50	389	94	137	100	346	188	62	161	4	59	67	0	0.34	0.27
41	346	U1425	D	9	H	3	101	329	238	114	78	277	141	54	92	13	15	92	0	0.28	0.31
42	346	U1425	D	9	H	5	1	327	204	145	85	301	147	61	100	9	24	85	0	0.35	0.29
43	346	U1425	D	9	H	6	50	480	279	182	107	466	227	73	176	0	47	51	0	0.25	0.28
44	346	U1425	D	10	H	1	100	269	189	70	43	257	117	56	108	30	21	113	0	0.27	0.23
45	346	U1425	D	10	H	2	51	292	165	95	70	262	136	50	84	0	31	117	0	0.28	0.26
46	346	U1425	D	10	H	3	101	426	234	136	76	377	204	89	140	10	22	75	0	0.28	0.30
47	346	U1425	D	10	H	5	1	356	201	103	72	224	144	63	76	14	35	110	0	0.32	0.30
48	346	U1425	D	10	H	6	51	207	124	99	46	119	80	51	21	11	26	136	0	0.40	0.29
49	346	U1425	D	11	H	1	30	315	197	108	78	239	119	42	91	23	13	91	0	0.31	0.28
50	346	U1425	D	11	H	2	50	191	76	109	49	119	61	20	41	0	17	210	0	0.23	0.30
51	346	U1425	D	11	H	3	101	276	152	104	44	186	118	84	89	3	28	103	0	0.33	0.30
52	346	U1425	D	11	H	5	1	365	258	107	109	89	57	27	71	37	18	122	0	0.22	0.27
53	346	U1425	D	11	H	6	51	378	228	112	88	236	127	33	101	20	0	78	0	0.31	0.32
54	346	U1425	D	12	H	1	0	306	217	111	69	256	124	53	82	0	30	104	0	0.31	0.26
55	346	U1425	D	12	H	2	51	401	218	117	79	327	206	141	95	15	0	83	0	0.30	0.24
56	346	U1425	D	12	H	3	96	389	242	123	70	195	107	42	106	0	21	76	0	0.33	0.29
57	346	U1425	D	13	X	1	51	334	180	87	68	226	82	46	90	12	49	102	0	0.27	0.12
58	346	U1425	D	13	X	3	51	301	153	110	51	156	143	86	43	0	12	94	0	0.35	0.27
59	346	U1425	D	13	X	5	50	355	168	98	58	196	97	53	96	0	33	72	0	0.32	0.25
60	346	U1425	D	13	X	7	50	305	168	94	64	177	100	81	78	0	19	90	0	0.33	0.29
61	346	U1425	D	14	H	1	50	350	160	113	61	180	92	47	96	0	16	99	0	0.34	0.26
62	346	U1425	D	14	H	3	50	357	170	111	57	188	135	93	79	0	72	94	0	0.38	0.30
63	346	U1425	D	15	H	1	50	349	211	107	76	194	104	57	62	0	17	83	0	0.29	0.30
64	346	U1425	D	15	H	3	50	319	177	92	48	207	130	104	71	0	88	89	0	0.27	0.30
65	346	U1425	D	15	H	5	50	325	143	114	59	177	129	73	68	54	61	78	0	0.39	0.25
66	346	U1425	D	15	H	7	50	325	143	114	59	177	129	73	38	0	61	78	0	0.39	0.25
67	346	U1425	D	16	H	1	50	283	149	119	67	180	73	58	50	0	18	94	0	0.28	0.37
68	346	U1425	D	16	H	3	53	329	145	120	85	185	122	81	79	0	19	85	0	0.37	0.23
69	346	U1425	D	16	H	5	53	235	107	71	42	152	91	67	87	15	39	125	0	0.18	0.35
70	346	U1425	D	16	H	7	50	292	209	74	55	155	127	24	91	12	56	108	0	0.44	0.23
71	346	U1425	D	18	H	1	50	251	145	76	82	107	71	21	72	0	60	107	0	0.33	0.26
72	346	U1425	D	18	H	3	50	265	100	89	57	134	34	41	37	0	0	115	0	0.26	0.24
73	346	U1425	D	18	H	5	50	218	105	108	41	116	120	95	54	0	0	138	0	0.48	0.23
74	346	U1425	D	18	H	7	50	233	61	85	44	128	88	32	39	52	17	134	0	0.27	0.28
75	346	U1425	D	19	H	1	50	220	86	40	31	102	95	55	44	21	34	166	0	0.25	0.49
76	346	U1425	D	19	H	3	50	294	97	100	64	168	89	63	60	36	0	105	0	0.32	0.27
77	346	U1425	D	19	H	5	50	334	158	85	69	183	130	72	80	29	59	84	0	0.41	0.30
78	346	U1425	D	19	H	7	50	282	153	87	66	131	85	50	70	16	33	97	0	0.41	0.30
79	346	U1425	D	20	H	1	50	271	144	95	39	110	66	43	60	26	13	103	0	0.45	0.32
80	346	U1425	D	20	H	3	50	261	128	71	59	137	91	52	31	13	22	147	0	0.28	0.28
81	346	U1425	D	20	H	5	51	241	118	107	40	105	109	62	74	0	0	125	0	0.37	0.23
82	346	U1425	D	20	H	7	50	234	124	75	50	146	87	63	50	38	0	116	0	0.25	0.37
83	346	U1425	D	21	H	1	70	257	147	64	51	135	41	40	65	47	0	107	0	0.49	0.28
84	346	U1425	D	21	H	3	50	218	81	100	54	96	91	74	74	23	73	124	0	0.45	0.19
85	346	U1425	D	21	H	5	50	245	128	99	58	149	66	32	69	55	22	115	0	0.44	0.23
86	346	U1425	D	22	H	1	50	188	71	51	38	73	38	22	52	12	0	163	0	0.49	0.26
87	346	U1425	D	22	H	3	50	204	104	57	43	111	72	59	71	13	31	183	0	0.28	0.28
88	346	U1425	D	22	H	5	51	225	130	65	46	124	43	26	30	24	0	166	0	0.16	0.15
89	346	U1425	D	22	H	7	50	222	83	70	23	56	102	30	31	23	40	137	0	0.22	0.26
90	346	U1425	D	23	H	1	50	241	115	59	49	150	43	36	38	30	23	111	0	0.28	0.19

91	346	U1425	D	23	H	3	50	260	136	76	58	124	62	18	40	25	23	115	0	0.44	0.31
92	346	U1425	D	23	H	5	50	271	160	68	55	130	81	39	43	64	0	105	0	0.57	0.33
93	346	U1425	D	23	H	7	50	234	122	60	40	106	98	63	40	57	59	132	0	0.49	0.24
94	346	U1425	D	24	H	1	50	254	114	93	35	163	69	34	40	55	61	120	0	0.30	0.25
95	346	U1425	D	24	H	3	50	300	191	110	68	152	75	0	49	23	13	78	0	0.47	0.20
96	346	U1425	D	24	H	5	51	234	77	79	44	95	91	63	50	46	45	163	0	0.20	0.58
97	346	U1425	D	24	H	7	54	301	164	85	56	165	64	73	49	30	22	90	0	0.26	0.19
98	346	U1425	D	25	H	1	50	273	122	51	36	91	70	50	55	18	31	143	0	0.43	0.33
99	346	U1425	D	25	H	3	50	267	128	97	48	108	65	57	47	63	50	93	0	0.49	0.21
100	346	U1425	D	26	X	1	50	329	200	132	68	184	62	32	73	22	18	80	0	0.27	0.26
101	346	U1425	D	26	X	3	50	297	128	107	43	161	90	63	82	42	15	91	0	0.40	0.23
102	346	U1425	D	26	X	5	50	270	156	63	52	129	73	35	54	21	0	92	0	0.31	0.33
103	346	U1425	D	26	X	7	50	319	129	82	49	139	83	53	57	13	45	94	0	0.38	0.22
104	346	U1425	D	27	H	1	50	305	170	72	47	177	113	49	59	34	51	85	0	0.33	0.30
105	346	U1425	D	27	H	3	50	319	159	113	70	162	75	31	61	28	13	72	0	0.45	0.29
106	346	U1425	D	28	H	1	50	312	160	99	66	141	86	58	55	39	43	103	0	0.32	0.22
107	346	U1425	D	28	H	3	51	294	148	63	51	135	79	42	32	59	0	94	0	0.47	0.17
108	346	U1425	D	28	H	5	51	284	178	100	57	138	68	42	50	78	0	91	0	0.57	0.18
109	346	U1425	D	28	H	7	50	279	77	90	60	115	70	57	57	42	18	111	0	0.35	0.25
110	346	U1425	D	29	H	1	50	270	151	90	59	137	93	63	56	79	0	90	0	0.66	0.14
111	346	U1425	D	29	H	3	50	239	120	73	50	58	41	31	32	31	0	145	0	0.36	0.78
112	346	U1425	D	30	H	1	50	288	133	90	46	137	84	60	72	42	0	103	0	0.20	0.31
113	346	U1425	D	30	H	3	50	270	145	86	44	147	108	53	43	62	1	123	0	0.46	0.19
114	346	U1425	D	30	H	5	51	333	145	118	58	193	119	62	24	62	15	89	0	0.27	0.12
115	346	U1425	D	30	H	7	50	312	158	101	70	136	51	40	43	124	0	99	0	0.39	0.17
116	346	U1425	D	31	H	1	0	269	127	85	39	103	70	48	21	92	37	125	0	0.42	0.25
117	346	U1425	D	31	H	2	50	288	148	108	56	131	102	52	67	99	42	111	0	0.54	0.25
118	346	U1425	D	31	H	3	100	341	204	117	89	100	39	34	43	81	12	80	0	0.39	0.12
119	346	U1425	D	31	H	5	0	343	197	98	79	160	95	53	24	69	21	73	0	0.47	0.18
120	346	U1425	D	31	H	6	50	354	187	129	76	156	97	46	72	109	26	80	0	0.46	0.31
121	346	U1425	D	32	H	1	50	315	176	97	71	116	58	57	44	89	17	102	0	0.44	0.13
122	346	U1425	D	32	H	2	51	279	170	115	70	81	72	31	45	91	19	116	0	0.49	0.11
123	346	U1425	D	32	H	3	50	333	210	68	78	164	69	61	47	79	26	84	0	0.49	0.18
124	346	U1425	D	32	H	5	49	238	139	81	54	90	89	60	52	83	42	131	0	0.42	0.27
125	346	U1425	D	32	H	6	51	241	114	61	50	97	84	55	33	82	20	109	0	0.43	0.09
126	346	U1425	D	33	H	1	50	374	201	113	72	120	51	36	54	89	23	74	0	0.24	0.22
127	346	U1425	D	33	H	2	50	339	219	72	82	144	99	88	90	65	14	75	0	0.55	0.17
128	346	U1425	D	33	H	4	50	285	112	94	69	100	65	59	65	65	0	100	0	0.58	0.22
129	346	U1425	D	35	H	1	6	207	58	28	0	32	34	39	23	28	4	192	0	0.47	0.08
130	346	U1425	D	35	H	2	50	350	167	123	59	132	47	35	53	22	30	68	0	0.40	0.16
131	346	U1425	D	35	H	3	54	270	163	103	81	77	47	25	61	60	16	97	0	0.40	0.38
132	346	U1425	D	36	H	1	50	255	109	102	40	86	52	34	34	33	22	101	0	0.57	0.16
133	346	U1425	D	36	H	2	50	322	165	105	60	94	60	38	73	73	0	83	0	0.55	0.21
134	346	U1425	D	36	H	3	50	335	162	89	60	54	43	26	71	79	0	75	0	0.51	0.17
135	346	U1425	D	37	H	1	0	328	178	92	59	126	57	63	132	43	31	77	0	0.47	0.52
136	346	U1425	D	37	H	2	51	280	156	72	64	91	40	29	61	137	12	78	0	0.19	0.26
137	346	U1425	D	37	H	4	50	308	138	102	49	97	41	44	81	43	18	98	0	0.31	0.20
138	346	U1425	D	37	H	5	50	278	127	108	57	88	59	17	44	16	21	126	0	0.55	0.14
139	346	U1425	D	37	H	7	54	259	182	90	103	84	41	30	46	94	28	88	0	0.44	0.24
140	346	U1425	D	38	H	1	50	262	129	85	58	86	55	48	51	23	20	110	0	0.53	0.73
141	346	U1425	D	38	H	2	50	256	167	91	57	86	59	27	35	35	0	104	0	0.35	0.37
142	346	U1425	D	38	H	3	54	317	192	118	67	101	69	51	68	45	54	79	0	0.67	0.20
143	346	U1425	D	39	H	1	50	295	143	102	62	135	66	39	67	44	0	78	0	0.37	0.64
144	346	U1425	D	39	H	2	50	216	108	70	42	65	90	71	52	24	24	154	0	0.68	0.23
145	346	U1425	D	39	H	3	54	204	87	71	22	60	36	28	64	191	11	121	0	0.18	0.16
146	346	U1425	D	40	H	1	50	274	146	61	56	109	56	24	41	110	0	100	0	0.19	0.40
147	346	U1425	D	40	H	2	51	297	177	94	58	106	63	41	102	55	23	80	0	0.81	0.13
148	346	U1425	D	40	H	3	100	239	117	95	41	88	30	31	39	20	16	158	0	0.46	0.20
149	346	U1425	D	41	H	1	50	232	124	60	48	86	88	50	44	45	0	128	0	0.21	0.33
150	346	U1425	D	41	H	2	50	288	149	98	52	125	61	53	47	119	27	93	0	0.33	0.26
151	346	U1425	D	41	H	3	50	204	100	78	40	58	41	44	49	83	0	128	0	0.37	0.40
152	346	U1425	D	42	H	1	50	274	109	96	53	88	74	56	39	121	40	100	0	0.38	0.23
153	346	U1425	D	42	H	2	50	313	151	105	60	85	75	45	42	92	18	79	0	0.54	0.29
154	346	U1425	D	42	H	3	54	249	168	83	54	113	51	40	77	71	15	83	0	0.45	0.21
155	346	U1425	D	43	H	1	50	233	126	62	51	84	81	58	65	109	29	119	0	0.31	0.62
156	346	U1425	D	43	H	2	50	235	132	95	49	82	69	38	82	82	0	106	0	0.43	0.33
157	346	U1425	D	43	H	3	54	256	142	71	70	105	67	62	71	41	20	107	0	0.26	0.31
158	346	U1425	D	43	H	5	1	264	167	96	73	92	76	79	70	126	28	94	0	0.17	0.28
159	346	U1425	D	43	H	6	50	276	149	98	57	98	38	41	72	63	21	99	0	0.52	0.37
160	346	U1425	D	44	H	1	50	363	167	106	65	97	77	38	66	93	15	83	0	0.49	0.32
161	346	U1425	D	44	H	2	50	247	140	79	45	85	58	40	57	134	28	94	0	0.37	0.31
162	346	U1425	D	44	H	3	50	249	131	79	83	91	34	25	63	39	14	105	0	0.47	0.18
163	346	U1425	D	45	H	1	0	291	176	72	76	128	64	25	48	65	16	95	0	0.42	0.18
164	346	U1425	D	45	H	2	51	308	181	126	74	110	71	59	35	64	14	91	0	0.43	0.27
165	346	U1425	D	45	H	3	54	383	196	156	95	132	28	20	53	33	0	74	0	0.66	0.13
166	346	U1425	D	46	H	1	50	262	150	86	57	84	54	34	100	52	6	106	0	0.41	0.30
167	346	U1425	D	46	H	2	50	350	220	110	90	126	72	47	99	0	25	83	0	0.41	0.27
168	346	U1425	D	46	H	3	50	331	160	122	83	125	72	49	59	32	15	74	0	0.39	0.26
169	346	U1425	D	47	H	1	0	308	206	84	102	138	55	27	59	33	19	80	0	0.32	0.24
170	346	U1425	D	47	H	2	49	322	122	100	65	71	36	15	57	62	21	104	0	0.19	0.11
171	346	U1425	D	47	H	3	54	434	92	73	45	92	37	0	58	47	14	143	0	0.06	0.68
172	346	U1425	D	48	H	1	50	363	143	64	62	85	34	0	48	46	16	121	0	0.37	0.26
173	346	U1425	D	48	H	2	51	342	179	102	59	139	52	22	69	50	22	88	0	0.61	0.21
174	346	U1425	D	49	H	1	23	424	178	98	71	111	29	0	60	64	0	103	0	0.35	0.26
175	346	U1425	D	48	H	3	54	347	160	131	58	144	64	35	81	40	21	82	0	0.45	0.31
176	346	U1425	D	49	H	2	50	429	92	61	75	73	42	17	55	45	30	129	0	0.11	0.24
177	346	U1425	D	49	H	3	99	408	136	67	53	79	24	48	42	59	54	121	0	0.55	0.26
178	346	U1425	D	50	H	1	50	361	197	148	90	158	79	47	117	58	2	63	0	0.60	0.20
179	346	U1425	D	50	H	2	48	386	187	130	90	152	71	46	77	72	15	63	0	0.49	0.17
180	346	U1425	D	50	H	3	50	356	209	140	83	160	64	28	96	53	0	59	0	0.32	0.25

Table S4: Contents (%) of silt (>4 μm) and clay (<4 μm) in dry sediment sample, and contribution (%) of each end-member in silt and clay fractions estimated by PARAFAC modelling. End-member contributions are expressed as the average and standard deviation of 20 times trial of PARAFAC calculation.

Sample Number	Exp	Site	Hole	Core	Type	Sect	Offset (cm)	Silt (%) >4μm	Silt EM1% (Tak)	Silt EM2% (Gobi)	Silt EM3% (Japan)	Silt EM4% (Diatomaceous)	Silt EM5% (Ordos)	Silt EM6% (Opal-CT)
1	346	U1425	D	1	H	1	2	26.55	13.85 ± 0.23	49.56 ± 0.26	23.41 ± 2.37	14.69 ± 2.20	0.00 ± 0.00	2.46 ± 0.65
2	346	U1425	D	1	H	2	57	43.37	19.55 ± 6.10	33.13 ± 1.24	8.49 ± 1.79	1.58 ± 0.41	33.34 ± 4.91	3.23 ± 0.38
3	346	U1425	D	1	H	3	101	34.87	42.05 ± 1.15	40.56 ± 0.31	6.24 ± 0.43	3.02 ± 0.41	5.92 ± 0.92	4.13 ± 0.59
4	346	U1425	D	2	H	1	1	33.01	22.36 ± 8.91	20.48 ± 1.77	3.78 ± 2.63	2.72 ± 1.42	48.30 ± 7.04	5.45 ± 0.82
5	346	U1425	D	2	H	2	54	39.35	51.56 ± 0.63	37.86 ± 0.21	6.23 ± 0.23	1.71 ± 0.42	0.79 ± 0.21	4.14 ± 0.83
6	346	U1425	D	2	H	3	100	28.77	42.91 ± 0.66	26.99 ± 0.35	16.06 ± 1.37	4.93 ± 0.71	1.68 ± 0.26	7.29 ± 0.82
7	346	U1425	D	2	H	5	0	34.77	15.83 ± 0.27	44.90 ± 0.40	32.64 ± 1.76	5.27 ± 2.27	0.00 ± 0.00	3.37 ± 0.91
8	346	U1425	D	2	H	6	52	35.36	67.18 ± 0.86	31.17 ± 0.18	0.00 ± 0.00	0.00 ± 0.00	1.12 ± 0.28	5.19 ± 0.85
9	346	U1425	D	3	H	1	88	36.72	42.56 ± 3.58	20.99 ± 0.77	10.85 ± 1.13	2.08 ± 0.58	19.83 ± 2.96	3.70 ± 0.62
10	346	U1425	D	3	H	2	50	33.85	56.95 ± 0.66	13.91 ± 0.11	16.34 ± 1.87	6.02 ± 2.21	1.31 ± 0.27	1.05 ± 0.93
11	346	U1425	D	3	H	3	101	53.02	32.18 ± 0.50	36.28 ± 0.41	27.85 ± 1.50	2.28 ± 2.04	2.26 ± 0.42	4.25 ± 1.16
12	346	U1425	D	3	H	5	1	34.70	33.07 ± 0.80	15.49 ± 0.29	20.54 ± 3.36	19.74 ± 2.45	4.90 ± 0.50	6.53 ± 2.02
13	346	U1425	D	3	H	6	50	49.02	20.18 ± 6.36	14.76 ± 1.33	18.45 ± 2.22	6.37 ± 0.84	35.25 ± 5.12	3.92 ± 0.50
14	346	U1425	D	4	H	1	18	37.03	54.76 ± 0.62	20.89 ± 0.12	14.48 ± 1.88	8.35 ± 1.92	1.39 ± 0.24	1.75 ± 0.61
15	346	U1425	D	4	H	2	51	40.42	29.29 ± 6.35	17.60 ± 1.28	6.46 ± 1.86	5.96 ± 0.97	34.80 ± 5.05	4.53 ± 0.73
16	346	U1425	D	4	H	3	100	39.24	21.14 ± 3.14	31.96 ± 0.74	17.22 ± 1.45	4.50 ± 0.61	17.39 ± 2.54	4.91 ± 0.57
17	346	U1425	D	4	H	5	0	37.46	20.72 ± 0.21	37.69 ± 0.19	17.94 ± 2.05	12.63 ± 1.85	1.20 ± 0.09	2.40 ± 0.54
18	346	U1425	D	4	H	6	51	33.02	24.43 ± 10.73	1.93 ± 2.13	6.13 ± 2.81	5.83 ± 0.95	58.90 ± 8.57	2.52 ± 0.61
19	346	U1425	D	5	H	1	28	48.00	19.37 ± 9.08	13.55 ± 1.84	11.22 ± 2.69	4.24 ± 0.75	49.62 ± 7.22	4.78 ± 0.72
20	346	U1425	D	5	H	2	50	25.84	37.76 ± 0.44	14.71 ± 0.13	16.82 ± 3.04	17.21 ± 2.30	1.89 ± 0.13	3.80 ± 1.20
21	346	U1425	D	5	H	3	100	36.97	19.84 ± 0.51	15.69 ± 0.55	38.37 ± 3.22	9.71 ± 2.14	2.58 ± 0.32	8.60 ± 1.30
22	346	U1425	D	5	H	5	0	33.39	43.05 ± 0.64	30.65 ± 0.33	17.62 ± 1.05	1.54 ± 1.17	2.06 ± 0.39	5.09 ± 0.93
23	346	U1425	D	5	H	6	50	40.11	45.27 ± 0.94	38.43 ± 0.32	8.78 ± 0.48	0.12 ± 0.17	4.16 ± 0.70	4.90 ± 0.88
24	346	U1425	D	6	H	1	0	46.72	13.57 ± 0.19	19.05 ± 0.24	26.18 ± 5.56	35.63 ± 4.51	1.93 ± 0.23	8.87 ± 4.42
25	346	U1425	D	6	H	2	50	30.24	42.37 ± 0.54	22.03 ± 0.24	20.09 ± 2.09	9.96 ± 1.76	1.86 ± 0.25	4.43 ± 0.51
26	346	U1425	D	6	H	3	100	35.85	23.05 ± 4.08	38.50 ± 0.88	11.06 ± 1.36	0.00 ± 0.00	22.27 ± 3.33	3.60 ± 0.69
27	346	U1425	D	6	H	5	0	22.15	39.96 ± 0.57	24.21 ± 0.27	15.63 ± 1.76	9.57 ± 1.22	1.84 ± 0.21	6.24 ± 0.92
28	346	U1425	D	6	H	6	50	33.22	42.79 ± 0.65	23.11 ± 0.36	20.59 ± 1.39	1.10 ± 1.39	1.86 ± 0.36	5.73 ± 0.95
29	346	U1425	D	7	H	1	0	34.80	31.32 ± 1.75	37.44 ± 0.50	17.55 ± 1.00	2.07 ± 0.94	9.78 ± 1.50	4.07 ± 0.81
30	346	U1425	D	7	H	2	50	37.89	18.98 ± 0.45	21.21 ± 0.19	18.18 ± 3.74	24.00 ± 3.05	3.39 ± 0.21	5.19 ± 2.50
31	346	U1425	D	7	H	3	100	39.85	17.85 ± 0.25	49.84 ± 0.38	31.48 ± 1.32	2.43 ± 2.52	0.27 ± 0.16	1.67 ± 1.45
32	346	U1425	D	7	H	5	4	33.81	45.30 ± 0.60	47.60 ± 0.28	6.37 ± 0.35	0.83 ± 0.16	0.61 ± 0.18	5.40 ± 0.82
33	346	U1425	D	7	H	6	50	44.01	12.20 ± 1.30	27.18 ± 0.37	26.20 ± 2.91	17.16 ± 2.97	8.74 ± 1.15	0.00 ± 0.00
34	346	U1425	D	8	H	1	100	31.41	44.13 ± 0.65	39.16 ± 0.34	8.73 ± 0.76	0.00 ± 0.01	0.94 ± 0.22	6.94 ± 0.90
35	346	U1425	D	8	H	2	50	28.57	31.94 ± 0.47	40.91 ± 0.37	19.29 ± 0.99	0.79 ± 1.01	1.03 ± 0.24	5.08 ± 0.96
36	346	U1425	D	8	H	3	101	33.39	38.01 ± 0.51	52.87 ± 0.30	6.61 ± 0.47	0.56 ± 0.25	0.49 ± 0.15	5.19 ± 0.81
37	346	U1425	D	8	H	5	2	26.79	49.56 ± 0.68	31.02 ± 0.24	5.33 ± 0.67	4.69 ± 0.65	1.11 ± 0.17	6.73 ± 0.75
38	346	U1425	D	8	H	6	50	27.57	54.63 ± 0.68	26.55 ± 0.19	8.15 ± 1.00	5.67 ± 0.78	1.17 ± 0.20	4.98 ± 0.51
39	346	U1425	D	9	H	1	0	29.50	39.48 ± 0.59	24.43 ± 0.32	18.32 ± 1.51	5.75 ± 1.10	1.91 ± 0.29	5.91 ± 0.67
40	346	U1425	D	9	H	2	50	32.21	46.10 ± 0.59	22.87 ± 0.20	12.57 ± 1.56	8.46 ± 1.18	1.62 ± 0.22	4.81 ± 0.56
41	346	U1425	D	9	H	3	101	24.24	28.17 ± 0.49	31.33 ± 0.40	19.73 ± 1.95	10.12 ± 1.18	1.10 ± 0.09	8.85 ± 1.56
42	346	U1425	D	9	H	5	1	27.56	35.70 ± 0.56	38.22 ± 0.35	11.77 ± 1.13	6.66 ± 0.91	0.84 ± 0.09	8.33 ± 1.21
43	346	U1425	D	9	H	6	50	32.19	65.49 ± 0.77	16.10 ± 0.12	13.83 ± 1.46	4.17 ± 2.00	0.94 ± 0.25	1.83 ± 1.18
44	346	U1425	D	10	H	1	100	26.51	47.74 ± 0.56	7.19 ± 0.08	17.31 ± 4.11	23.19 ± 2.99	1.14 ± 0.07	4.69 ± 1.92
45	346	U1425	D	10	H	2	51	27.52	60.64 ± 0.75	8.75 ± 0.02	14.33 ± 3.60	18.63 ± 2.67	0.07 ± 0.06	2.72 ± 0.87
46	346	U1425	D	10	H	3	101	31.74	32.55 ± 0.51	45.90 ± 0.36	13.38 ± 0.80	2.44 ± 0.30	1.01 ± 0.19	6.50 ± 0.78
47	346	U1425	D	10	H	5	1	28.20	16.46 ± 0.20	48.58 ± 0.23	16.22 ± 2.17	15.06 ± 2.01	0.00 ± 0.00	3.52 ± 1.11
48	346	U1425	D	10	H	6	51	22.39	47.68 ± 0.69	0.00 ± 0.00	21.35 ± 5.61	30.28 ± 4.15	0.01 ± 0.04	1.56 ± 1.96
49	346	U1425	D	11	H	1	30	35.27	17.54 ± 0.25	26.21 ± 0.32	25.56 ± 3.55	21.55 ± 2.67	1.11 ± 0.12	7.82 ± 2.53
50	346	U1425	D	11	H	2	50	34.58	9.61 ± 0.15	4.05 ± 0.11	19.89 ± 8.03	53.87 ± 7.20	2.20 ± 0.51	11.51 ± 7.44
51	346	U1425	D	11	H	3	101	39.97	3.92 ± 0.14	28.40 ± 0.42	39.96 ± 3.87	19.44 ± 2.90	0.69 ± 0.14	6.33 ± 1.80
52	346	U1425	D	11	H	5	1	36.92	0.72 ± 0.18	21.68 ± 0.11	25.57 ± 6.27	40.41 ± 5.20	1.58 ± 0.34	5.71 ± 4.58
53	346	U1425	D	11	H	6	51	31.85	24.90 ± 0.44	20.95 ± 0.37	25.72 ± 2.81	14.37 ± 1.82	2.03 ± 0.16	7.81 ± 1.69
54	346	U1425	D	12	H	1	0	39.81	16.06 ± 0.30	10.97 ± 0.26	23.47 ± 5.67	36.87 ± 4.73	2.19 ± 0.24	11.00 ± 5.11
55	346	U1425	D	12	H	2	51	32.77	26.28 ± 0.37	26.08 ± 0.31	22.99 ± 2.82	16.24 ± 2.05	1.52 ± 0.08	6.83 ± 1.68
56	346	U1425	D	12	H	3	96	33.31	24.36 ± 0.52	16.63 ± 0.51	32.63 ± 3.17	12.50 ± 1.72	1.95 ± 0.19	10.00 ± 1.84
57	346	U1425	D	13	X	1	51	50.93	8.19 ± 0.34	19.54 ± 0.55	41.67 ± 4.05	18.06 ± 2.49	2.22 ± 0.16	9.85 ± 2.34
58	346	U1425	D	13	X	3	51	53.08	6.92 ± 0.22	15.18 ± 0.30	29.49 ± 5.44	34.13 ± 4.26	2.32 ± 0.18	9.53 ± 4.44
59	346	U1425	D	13	X	5	50	52.31	10.25 ± 0.41	16.95 ± 0.63	44.71 ± 3.59	9.35 ± 2.39	2.18 ± 0.28	9.25 ± 1.43
60	346	U1425	D	13	X	7	50	32.61	17.12 ± 0.45	10.75 ± 0.51	37.26 ± 4.03	18.31 ± 2.37	2.37 ± 0.17	10.34 ± 2.50
61	346	U1425	D	14	H	1	50	34.33	13.17 ± 0.34	15.84 ± 0.48	35.09 ± 4.17	21.69 ± 2.63	1.78 ± 0.11	10.63 ± 3.01
62	346	U1425	D	14	H	3	50	29.97	27.74 ± 0.36	6.92 ± 0.24	26.29 ± 4.90	28.73 ± 3.55	1.74 ± 0.13	8.08 ± 3.31
63	346	U1425	D	15	H	1	50	61.66	13.06 ± 0.36	9.58 ± 0.44	35.67 ± 4.67	25.05 ± 3.06	2.40 ± 0.11	10.18 ± 3.30
64	346	U1425	D	15	H	3	50	49.00	16.06 ± 0.50	9.97 ± 0.59	41.66 ± 4.61	20.89 ± 2.59	2.48 ± 0.16	12.48 ± 3.11
65	346	U1425	D	15	H	5	50	41.73	24.63 ± 0.53	11.91 ± 0.53	37.29 ± 3.56	13.18 ± 2.12	2.32 ± 0.24	9.76 ± 1.76
66	346	U1425	D	15	H	7	50	59.06	0.00 ± 0.00	19.33 ± 0.40	42.96 ± 4.79	24.47 ± 3.36	1.63 ± 0.32	7.35 ± 2.67
67	346	U1425	D	16	H	1	50	45.24	15.37 ± 0.34	9.66 ± 0.37	30.15 ± 5.16	30.95 ± 3.78	2.15 ± 0.17	11.21 ± 4.30
68	346	U1425	D	16	H	3	53	43.59	21.79 ± 0.36	4.25 ± 0.38	36.17 ± 5.05	26.77 ± 3.35	2.07 ± 0.12	9.52 ± 3.21
69	346	U1425	D	16	H	5	53	54.30	7.69 ± 0.30	9.83 ± 0.34	27.47 ± 6.05	39.28 ± 5.04	2.29 ± 0.29	12.88 ± 5.80
70	346	U1425	D	16	H	7	50	48.47	14.25 ± 0.24	6.36 ± 0.28	28.65 ± 6.19	38.77 ± 4.85	2.05 ± 0.28	10.94 ± 5.20
71	346	U1425	D	18	H	1	50	50.35	2.85 ± 0.13	10.50 ± 0.23	23.33 ± 7.38	50.26 ± 6.75	1.77 ± 0.54	13.42 ± 7.37
72	346	U1425	D	18	H	3	50	44.54	8.95 ± 0.24	9.24 ± 0.26	23.45 ± 6.74	45.19 ± 5.99	2.10 ± 0.41	13.20 ± 6.65
73	346	U1425	D	18	H	5	50	44.18	7.69 ± 0.11	1.08 ± 0.07	17.00 ± 9.11	61.61 ± 8.37	1.68 ± 0.71	11.76 ± 8.54
74	346	U1425	D	18	H	7	50	35.45	21.17 ± 0.25	3.46 ± 0.09	16.94 ± 7.28	48.44 ± 6.45	1.22 ± 0.55	10.98 ± 6.61
75	346	U1425	D	19	H	1	50	50.79	5.28 ± 0.05	4.51 ± 0.10	10.47 ± 9.63	67.95 ± 9.76	1.56 ± 0.88	14.75 ± 10.11
76	346	U1425	D	19	H	3	50	41.49	12.19 ± 0.20	13.24 ± 0.18	17.41 ± 6.50	44.86 ± 6.13	1.63 ± 0.47	12.23 ± 6.53
77	346	U1425	D	19	H	5	50	29.67	28.40 ± 0.42	21.43 ± 0.29	18.53 ± 3.64	23.75 ± 3.02	1.24 ± 0.15	9.88 ± 3.26
78	346	U1425	D	19	H	7	50	34.97	21.97 ± 0.38	14.27 ± 0.33	24.14 ± 4.54	28.38 ± 3.54	1.70 ± 0.18	11.03 ± 4.01
79	346	U1425	D	20	H	1	50	29.25	23.55 ± 0.28	9.83 ± 0.14	17.11 ± 5.76	38.12 ± 5.00	1.22 ± 0.38	9.80 ± 5.09
80	346	U1425	D	20	H	3	50	31.93	16.68 ± 0.17	5.31 ± 0.07	10.97 ± 8.18	56.52 ± 7.90	1.23 ± 0.70	12.11 ± 8.03
81	346	U1425	D	20	H	5	51	44.84	2.08 ± 0.09	16.54 ± 0.32	29.19 ± 6.17	40.30 ± 5.17	1.18 ± 0.45	12.10 ± 5.75
82	346	U1425	D	20	H	7	50	38.38	7.06 ± 0.19	13.34 ± 0.25	21.51 ± 6.32	43.06 ± 5.78	1.71 ± 0.43	12.59 ± 6.36
83	346	U1425	D	21	H	1	70	29.47	41.67 ± 0.56	3.74 ± 0.02	19.96 ± 5.47	31.72 ± 4.05	0.34 ± 0.26	4.78 ± 2.96
84	346	U1425	D	21	H	3	50	32.64	17.16 ± 0.25	3.61 ± 0.22	26.09 ± 5.94	36.84 ± 4.60	2.04 ± 0.24	9.50 ± 4.76
85	346	U1425	D	21	H	5	50	33.16	19.76 ± 0.24	3.09 ± 0.06	14.77 ± 7.91	52.71 ± 7.08	1.16 ± 0.62	10.07 ± 7.02
86	346	U1425	D	22	H	1	50	35.66	1.61 ± 0.07	7.01 ± 0.09	10.54 ± 9.19	65.23 ± 9.41	1.69 ± 0.82	14.29 ± 9.75
87	346	U1425	D	22	H	3	50	48.19	5.89 ± 0.11	4.42 ± 0.08	15.47 ± 8.56	58.67 ± 8.07	2.01 ± 0.63	11.77 ± 8.27
88	346	U1425	D	22	H	5	51	31.69	19.32 ± 0.25	0.01 ± 0.02	25.14 ± 7.75	48.89 ± 6.25	1.35 ± 0.52	9.20 ± 6.10
89	346	U1425	D	22	H	7	50	35.05	17.58 ± 0.24	4.54 ± 0.24	29.33 ± 6.23	38.11 ± 4.73	1.92 ± 0.27	9.71 ± 4.81
90	346	U1425	D	23	H	1	50	34.05	34.40 ± 0.43	4.84 ± 0.17	24.45 ± 5.17	30.33 ± 3.77	1.08 ± 0.22	7.62 ± 3.35

91	346	U1425	D	23	H	3	50	36.13	9.58	±	0.14	17.15	±	0.15	19.74	±	6.14	41.52	±	5.49	1.83	±	0.36	9.47	± 5.51
92	346	U1425	D	23	H	5	50	34.59	24.79	±	0.35	12.67	±	0.19	14.96	±	5.35	36.52	±	4.94	1.42	±	0.35	11.38	± 5.25
93	346	U1425	D	23	H	7	50	43.48	9.82	±	0.09	4.43	±	0.09	9.66	±	9.01	63.49	±	9.12	1.25	±	0.84	14.28	± 9.45
94	346	U1425	D	24	H	1	50	49.84	6.57	±	0.07	4.33	±	0.10	12.01	±	9.11	64.03	±	9.13	1.56	±	0.81	14.59	± 9.56
95	346	U1425	D	24	H	3	50	49.15	19.63	±	0.39	8.78	±	0.41	34.67	±	4.41	22.81	±	2.86	2.35	±	0.12	9.38	± 2.80
96	346	U1425	D	24	H	5	51	57.60	0.00	±	0.00	6.27	±	0.13	7.04	±	10.04	71.98	±	10.66	1.43	±	1.09	15.89	± 11.08
97	346	U1425	D	24	H	7	54	51.20	17.39	±	0.31	6.41	±	0.34	33.93	±	5.20	29.25	±	3.61	2.35	±	0.11	9.06	± 3.52
98	346	U1425	D	25	H	1	50	50.60	5.38	±	0.13	2.23	±	0.13	20.71	±	8.52	57.59	±	7.76	2.22	±	0.59	12.85	± 8.21
99	346	U1425	D	25	H	3	50	36.45	10.34	±	0.11	7.18	±	0.09	15.33	±	7.81	53.73	±	7.39	1.63	±	0.61	11.99	± 7.63
100	346	U1425	D	26	X	1	50	55.59	20.58	±	0.54	9.31	±	0.55	37.16	±	4.47	21.61	±	2.56	2.45	±	0.15	12.80	± 3.31
101	346	U1425	D	26	X	3	50	37.40	11.20	±	0.27	13.62	±	0.32	24.91	±	5.59	36.68	±	4.75	1.77	±	0.32	12.38	± 5.39
102	346	U1425	D	26	X	5	50	52.31	9.80	±	0.31	6.18	±	0.33	29.13	±	6.19	39.13	±	4.93	2.53	±	0.25	12.18	± 5.57
103	346	U1425	D	26	X	7	50	50.02	14.77	±	0.27	3.20	±	0.36	35.83	±	5.88	33.79	±	4.12	2.04	±	0.20	10.63	± 4.36
104	346	U1425	D	27	H	1	50	39.82	18.68	±	0.34	9.41	±	0.31	27.69	±	5.05	30.62	±	3.76	2.25	±	0.14	10.14	± 4.05
105	346	U1425	D	27	H	3	50	57.98	15.86	±	0.50	10.58	±	0.60	42.18	±	4.16	16.06	±	2.29	2.49	±	0.22	11.38	± 2.40
106	346	U1425	D	28	H	1	50	30.65	14.18	±	0.18	9.58	±	0.11	15.76	±	6.64	45.22	±	6.12	1.79	±	0.43	10.58	± 6.28
107	346	U1425	D	28	H	3	51	34.40	14.34	±	0.39	13.70	±	0.41	28.76	±	4.61	27.77	±	3.40	2.13	±	0.14	11.74	± 4.09
108	346	U1425	D	28	H	5	51	36.18	18.39	±	0.32	7.58	±	0.33	29.28	±	5.48	33.29	±	4.09	1.96	±	0.21	11.18	± 4.53
109	346	U1425	D	28	H	7	50	40.65	9.61	±	0.14	6.92	±	0.18	21.11	±	7.04	47.28	±	6.29	1.61	±	0.50	12.13	± 6.75
110	346	U1425	D	29	H	1	50	37.21	25.45	±	0.38	6.78	±	0.32	28.75	±	4.50	25.23	±	3.08	1.73	±	0.11	9.16	± 3.12
111	346	U1425	D	29	H	3	50	50.56	1.88	±	0.20	8.04	±	0.23	22.51	±	7.36	50.11	±	6.76	2.18	±	0.49	13.39	± 7.42
112	346	U1425	D	30	H	1	50	42.23	10.60	±	0.40	10.53	±	0.45	30.30	±	5.22	31.95	±	3.98	2.06	±	0.23	13.87	± 5.04
113	346	U1425	D	30	H	3	50	21.11	27.56	±	0.39	16.85	±	0.22	15.10	±	4.14	27.91	±	3.68	1.31	±	0.21	9.93	± 3.90
114	346	U1425	D	30	H	5	51	23.11	25.65	±	0.36	12.87	±	0.22	19.33	±	4.42	28.27	±	3.56	1.79	±	0.15	9.03	± 3.68
115	346	U1425	D	30	H	7	50	19.41	17.17	±	0.21	9.74	±	0.14	15.31	±	6.20	42.29	±	5.73	1.35	±	0.45	10.95	± 5.98
116	346	U1425	D	31	H	1	0	15.05	20.14	±	0.24	6.17	±	0.08	15.90	±	6.72	44.67	±	5.93	0.98	±	0.52	9.74	± 5.96
117	346	U1425	D	31	H	2	50	17.92	15.64	±	0.22	15.27	±	0.21	18.21	±	5.12	34.60	±	4.58	1.05	±	0.37	10.32	± 4.87
118	346	U1425	D	31	H	3	100	40.85	12.65	±	0.52	9.99	±	0.68	47.52	±	4.45	15.25	±	2.44	2.68	±	0.26	12.07	± 2.39
119	346	U1425	D	31	H	5	0	33.64	30.71	±	0.50	7.67	±	0.44	35.57	±	3.71	15.20	±	2.41	1.89	±	0.18	8.56	± 1.66
120	346	U1425	D	31	H	6	50	22.22	20.48	±	0.45	8.93	±	0.48	34.55	±	4.03	19.12	±	2.35	1.93	±	0.12	10.71	± 2.70
121	346	U1425	D	32	H	1	50	16.63	18.61	±	0.23	4.62	±	0.13	18.76	±	6.34	41.65	±	5.44	1.32	±	0.43	10.20	± 5.65
122	346	U1425	D	32	H	2	51	24.75	11.33	±	0.19	7.47	±	0.19	17.54	±	6.76	46.57	±	6.39	1.42	±	0.54	13.19	± 6.97
123	346	U1425	D	32	H	3	50	22.39	24.89	±	0.35	8.11	±	0.27	25.30	±	4.67	27.92	±	3.41	1.11	±	0.23	9.48	± 3.59
124	346	U1425	D	32	H	5	49	24.06	14.62	±	0.18	7.74	±	0.11	11.21	±	7.55	53.21	±	7.59	1.14	±	0.69	13.64	± 7.98
125	346	U1425	D	32	H	6	51	24.50	20.12	±	0.26	5.80	±	0.18	20.77	±	6.00	38.95	±	5.02	1.45	±	0.37	10.45	± 5.29
126	346	U1425	D	33	H	1	50	43.31	9.82	±	0.39	15.67	±	0.60	42.09	±	3.92	14.91	±	2.19	1.95	±	0.17	10.77	± 2.24
127	346	U1425	D	33	H	2	50	31.70	15.02	±	0.53	15.70	±	0.61	38.05	±	3.77	14.70	±	1.86	2.22	±	0.19	12.08	± 2.51
128	346	U1425	D	33	H	4	50	25.17	15.40	±	0.23	4.73	±	0.23	24.38	±	5.83	37.06	±	4.68	1.52	±	0.33	10.51	± 5.06
129	346	U1425	D	35	H	1	6	45.50	1.66	±	0.19	5.79	±	0.24	21.96	±	8.16	56.32	±	7.77	1.93	±	0.65	15.87	± 8.67
130	346	U1425	D	35	H	2	50	69.01	12.66	±	0.58	11.90	±	0.82	53.34	±	4.45	7.42	±	2.62	2.28	±	0.33	12.80	± 1.86
131	346	U1425	D	35	H	3	54	53.74	7.47	±	0.41	10.55	±	0.61	42.15	±	4.87	23.49	±	2.78	1.99	±	0.15	13.47	± 3.73
132	346	U1425	D	36	H	1	50	51.29	7.99	±	0.40	10.57	±	0.54	38.28	±	5.23	28.82	±	3.43	2.31	±	0.16	13.58	± 4.43
133	346	U1425	D	36	H	2	50	62.22	13.55	±	0.53	5.99	±	0.75	53.60	±	4.98	15.79	±	2.78	2.51	±	0.26	13.20	± 2.54
134	346	U1425	D	36	H	3	50	70.93	7.98	±	0.57	11.91	±	0.82	53.43	±	4.60	10.19	±	2.44	2.50	±	0.31	13.38	± 2.19
135	346	U1425	D	37	H	1	0	65.83	12.12	±	0.67	10.31	±	0.90	55.15	±	4.82	7.62	±	2.41	2.34	±	0.33	14.99	± 2.27
136	346	U1425	D	37	H	2	51	38.63	20.06	±	0.46	11.04	±	0.51	37.26	±	3.79	15.84	±	2.24	2.25	±	0.19	9.83	± 2.10
137	346	U1425	D	37	H	4	50	66.10	7.64	±	0.52	10.38	±	0.71	47.56	±	4.91	20.03	±	2.50	2.51	±	0.18	14.22	± 3.38
138	346	U1425	D	37	H	5	50	23.61	10.30	±	0.22	10.14	±	0.26	20.83	±	6.59	45.12	±	6.13	1.21	±	0.55	14.12	± 6.88
139	346	U1425	D	37	H	7	54	41.82	8.62	±	0.20	17.57	±	0.45	37.51	±	4.45	23.63	±	2.96	1.30	±	0.16	9.49	± 2.97
140	346	U1425	D	38	H	1	50	44.51	8.98	±	0.36	7.69	±	0.49	36.36	±	5.77	33.84	±	4.10	2.18	±	0.24	14.01	± 5.12
141	346	U1425	D	38	H	2	50	46.72	5.80	±	0.28	11.33	±	0.49	39.06	±	5.37	30.07	±	3.62	2.08	±	0.18	12.12	± 4.26
142	346	U1425	D	38	H	3	54	58.69	12.53	±	0.48	11.11	±	0.66	47.54	±	4.34	14.84	±	2.54	2.54	±	0.25	11.22	± 2.17
143	346	U1425	D	39	H	1	50	71.68	11.56	±	0.54	8.89	±	0.76	53.28	±	4.60	11.81	±	2.76	2.70	±	0.32	12.11	± 2.02
144	346	U1425	D	39	H	2	50	41.33	5.93	±	0.20	4.31	±	0.27	26.73	±	7.47	49.37	±	6.47	2.12	±	0.48	13.92	± 7.25
145	346	U1425	D	39	H	3	54	53.51	5.85	±	0.32	8.04	±	0.39	32.45	±	5.93	36.60	±	4.54	2.49	±	0.23	12.61	± 5.33
146	346	U1425	D	40	H	1	50	67.13	5.29	±	0.38	12.58	±	0.64	49.80	±	4.77	19.34	±	2.89	2.61	±	0.21	11.03	± 2.59
147	346	U1425	D	40	H	2	51	63.28	10.54	±	0.52	12.78	±	0.73	49.79	±	4.45	13.90	±	2.46	2.63	±	0.27	12.29	± 2.28
148	346	U1425	D	40	H	3	100	53.95	12.19	±	0.49	6.60	±	0.44	36.20	±	5.71	33.06	±	4.00	3.53	±	0.13	11.84	± 4.54
149	346	U1425	D	41	H	1	50	36.69	6.69	±	0.23	6.39	±	0.35	30.03	±	6.61	42.40	±	5.40	1.89	±	0.40	13.62	± 6.26
150	346	U1425	D	41	H	2	50	61.51	10.83	±	0.46	9.34	±	0.67	48.19	±	4.74	18.32	±	2.62	2.39	±	0.20	12.44	± 2.77
151	346	U1425	D	41	H	3	50	48.70	5.54	±	0.41	9.50	±	0.56	42.48	±	5.34	28.02	±	3.35	2.70	±	0.14	12.89	± 4.11
152	346	U1425	D	42	H	1	50	48.14	12.88	±	0.49	5.40	±	0.59	44.94	±	5.13	23.86	±	3.01	3.04	±	0.19	12.26	± 3.36
153	346	U1425	D	42	H	2	50	52.20	12.05	±	0.57	8.74	±	0.72	50.22	±	4.66	15.33	±	2.56	3.03	±	0.31	12.55	± 2.45
154	346	U1425	D	42	H	3	54	37.96	16.74	±	0.45	9.78	±	0.56	40.62	±	4.35	19.20	±	2.49	2.21	±	0.15	11.42	± 2.74
155	346	U1425	D	43	H	1	50	42.72	7.94	±	0.17	7.89	±	0.24	22.65	±	7.23	48.91	±	6.56	1.63	±	0.54	13.84	± 7.25
156	346	U1425	D	43	H	2	50	41.80	7.42	±	0.29	11.12	±	0.37	27.13	±	5.85	38.18	±	4.96	1.75	±	0.36	13.98	± 5.91
157	346	U1425	D	43	H	3	54	55.39	8.88	±	0.34	4.99	±	0.45	35.15	±	6.14	36.91	±	4.53	2.22	±	0.27	13.99	± 5.52
158	346	U1425	D	43	H	5	1	50.94	10.44	±	0.33	5.37	±	0.48	38.81	±	5.60	31.09	±	3.73	2.19	±	0.18	12.57	± 4.43
159	346	U1425	D	43	H	6	50	45.42	12.98	±	0.38	4.93	±	0.54	43.17	±	5.33	26.68	±	3.27	2.30	±	0.14	12.18	± 3.69
160	346	U1425	D	44	H	1	50	20.93	22.91	±	0.34	2.45	±	0.36	36.25	±	4.69	23.47	±	3.13	1.79	±	0.11	8.10	± 2.55
161	346	U1425	D	44	H	2	50	36.27	16.95	±	0.26	3.91	±	0.26	26.59	±	5.76	35.74	±	4.45	1.73	±	0.28	10.43	± 4.80
162	346	U1425	D	44	H	3	50	40.14	8.85	±	0.19	4.31	±	0.28	28.53	±	6.78	43.47	±	5.53	1.88	±	0.40	12.35	± 6.15
163	346	U1425	D	45	H	1	0	17.07	26.41	±	0.36	5.96	±	0.20	21.07	±	5.55	35.38	±	4.49	0.97	±	0.37	10.53	± 4.77
164	346	U1425	D	45	H	2	51	20.41	21.11	±	0.34	4.79	±	0.31	27.54	±	5.54	33.88	±	4.18	1.30	±	0.31	11.71	± 4.74
165	346	U1425	D	45	H	3	54	35.87	19.16	±	0.60	4.80	±	0.75	51.18	±	4.62	11.71	±	2.60	2.39	±	0.29	12.89	± 2.13
166	346	U1425	D	46	H	1	50	43.98	7.36	±	0.46	10.85	±	0.59	37.75	±	5.10	27.61	±	3.28	2.13	±	0.19	15.12	± 4.65
167	346	U1425	D	46	H	2	50	77.52	13.00	±	0.76	9.40	±	1.00	59.89	±	5.20	4.82	±	2.76	2.61	±	0.41	16.01	± 2.24
168	346	U1425	D	46	H	3	50	54.96	9.93	±	0.69	13.09	±	0.94	56.76	±	4.84	5.18	±	2.55	2.43	±	0.37	14.96	± 2.13
169	346	U1425	D	47	H	1	0	66.66	4.24	±	0.65	16.67	±	0.97	56.75	±	4.91	5.89	±	2.24	2.01	±	0.31	15.84	± 2.38
170	346	U1425	D	47	H	2	49	58.64	12.85	±	1.36	5.79	±	1.20	40.32	±	5.91	10.92	±	2.65	2.44	±	0.29	29.18	± 5.89
171	346	U1425	D	47	H	3	54	62.26	11.83	±	2.37	5.01	±	1.60	11.34	±	7.65	17.29	±	9.81	2.01	±	0.61	50.37	± 11.97
172	346	U1425	D	48	H	1	50	62.11	11.59	±	2.24	10.48	±	1.60	19.76	±	7.62	10.77	±	7.97	2.14	±	0.48	46.42	± 10.18
173	346	U1425	D	48	H	2	51	46.89	16.30	±	1.37	10.78	±	1.23	46.80	±	5.91	2.73	±	1.47	3.10	±	0.42	26.00	± 4.25
174	346	U1425	D	49	H	1	23	48.98	12.69	±	2.30	7.35	±	1.64	19.44	±	7.86	10.18	±	8.17	2.08	±	0.50	47.65	± 10.40
175	346	U1425	D	48	H	3	54	75.45	7.16	±	1.19	15.89	±	1.26	52.86	±	6.03	1.38	±	1.39	2.45	±	0.37	24.63	± 3.86
176	346	U1425	D	49	H	2	50	50.55	12.80	±	2.65	6.91	±	1.74	4.54	±	8.34	14.48	±	11.38	1.63	±	0.69	55.61	± 12.98
177	346	U1425	D	49	H	3	99	49.14	12.76	±	2.61	8.58	±	1.73	6.03	±	8.32	12.82	±	10.88	1.72	±	0.66	54.41	± 12.48
178	346	U1425	D	50	H	1	50	53.86	17.30	±	0.83	8.96	±	0.95	53.32	±	4.80	2.00	±	2.38	2.59	±	0.43	15.80	± 2.11
179	346	U1425	D	50	H	2	48	48.05	13.07	±	0.87	11.13	±	1.00	54.22	±	4.97	2.74	±	2.17	2.77	±	0.43	16.82	± 2.34
180	346	U1425	D	50	H	3	50	57.52	10.30	±	0.70	16.31	±	0.87	50.96	±	4.35	5.02	±	2.13	2.59	±	0.38	14.09	± 2.01

Sample Number	Exp	Site	Hole	Core	Type	Sect	Offset (cm)	Clay (%) <4µm	Clay EM1% (Tak)	Clay EM2% (Gobi)	Clay EM3% (Japan)	Clay EM4% (Diatomaceous)	Clay EM5% (Ordos)	Clay EM6% (Opal-CT)
1	346	U1425	D	1	H	1	2	54.43	31.09 ± 0.74	0.00 ± 0.00	35.14 ± 1.00	24.43 ± 0.51	0.45 ± 0.36	0.04 ± 0.09
2	346	U1425	D	1	H	2	57	44.08	33.12 ± 0.96	26.60 ± 1.46	31.96 ± 0.76	2.36 ± 0.80	8.35 ± 0.86	1.87 ± 0.48
3	346	U1425	D	1	H	3	101	51.18	31.94 ± 0.62	13.91 ± 0.41	38.46 ± 0.45	9.06 ± 0.27	1.81 ± 0.21	1.02 ± 0.42
4	346	U1425	D	2	H	1	1	51.84	27.84 ± 2.09	2.41 ± 3.04	35.69 ± 1.94	10.08 ± 2.06	19.01 ± 1.95	0.44 ± 0.46
5	346	U1425	D	2	H	2	54	43.80	42.51 ± 0.62	24.40 ± 0.28	26.24 ± 0.65	2.91 ± 0.27	0.42 ± 0.09	1.05 ± 0.30
6	346	U1425	D	2	H	3	100	54.44	31.05 ± 0.47	17.81 ± 0.16	33.58 ± 0.39	10.11 ± 0.56	0.00 ± 0.00	3.36 ± 0.75
7	346	U1425	D	2	H	5	0	47.69	26.01 ± 0.37	22.37 ± 0.30	33.22 ± 0.33	11.01 ± 0.73	1.03 ± 0.13	3.86 ± 0.84
8	346	U1425	D	2	H	6	52	47.07	52.01 ± 0.69	31.06 ± 0.33	12.70 ± 1.01	2.78 ± 0.54	0.54 ± 0.19	0.03 ± 0.12
9	346	U1425	D	3	H	1	88	53.79	29.90 ± 2.22	19.77 ± 3.33	24.15 ± 1.99	1.84 ± 2.13	20.44 ± 2.07	2.39 ± 0.56
10	346	U1425	D	3	H	2	50	50.69	32.93 ± 0.41	40.09 ± 0.59	16.58 ± 0.31	8.73 ± 0.40	1.88 ± 0.24	2.07 ± 0.35
11	346	U1425	D	3	H	3	101	35.61	25.04 ± 0.57	7.97 ± 0.34	45.45 ± 0.29	13.33 ± 0.37	1.45 ± 0.18	1.74 ± 0.62
12	346	U1425	D	3	H	5	1	52.77	22.89 ± 0.45	13.41 ± 0.60	19.00 ± 0.39	38.40 ± 1.19	2.35 ± 0.61	4.70 ± 1.09
13	346	U1425	D	3	H	6	50	40.09	20.25 ± 2.26	16.29 ± 3.40	25.66 ± 2.09	11.56 ± 2.32	21.02 ± 2.09	2.98 ± 0.65
14	346	U1425	D	4	H	1	18	52.03	11.54 ± 0.15	36.46 ± 0.55	25.49 ± 0.44	14.63 ± 0.97	1.52 ± 0.28	3.44 ± 0.76
15	346	U1425	D	4	H	2	51	50.21	19.90 ± 1.72	31.06 ± 2.70	22.81 ± 1.59	7.86 ± 1.82	16.10 ± 1.57	2.85 ± 0.58
16	346	U1425	D	4	H	3	100	50.90	11.17 ± 0.60	51.66 ± 1.27	11.82 ± 0.57	17.45 ± 1.19	5.75 ± 0.56	1.94 ± 0.45
17	346	U1425	D	4	H	5	0	48.93	26.13 ± 0.29	42.99 ± 0.62	19.68 ± 0.28	9.10 ± 0.68	1.78 ± 0.28	3.05 ± 0.58
18	346	U1425	D	4	H	6	51	57.71	15.41 ± 3.36	27.17 ± 5.09	19.81 ± 3.19	4.93 ± 3.43	31.14 ± 3.10	1.82 ± 0.75
19	346	U1425	D	5	H	1	28	44.01	8.60 ± 4.58	25.27 ± 6.86	14.92 ± 4.40	7.07 ± 4.71	42.26 ± 4.20	2.42 ± 1.05
20	346	U1425	D	5	H	2	50	59.36	14.55 ± 0.23	64.80 ± 0.99	0.00 ± 0.00	21.94 ± 1.03	1.46 ± 0.57	0.15 ± 0.46
21	346	U1425	D	5	H	3	100	51.79	6.92 ± 0.06	35.22 ± 0.57	19.94 ± 0.41	27.23 ± 1.39	0.82 ± 0.36	4.63 ± 1.03
22	346	U1425	D	5	H	5	0	56.44	17.39 ± 0.15	49.50 ± 0.66	16.09 ± 0.28	12.54 ± 0.85	1.10 ± 0.35	2.61 ± 0.53
23	346	U1425	D	5	H	6	50	50.45	24.28 ± 0.32	45.91 ± 0.75	20.60 ± 0.34	7.11 ± 0.71	2.56 ± 0.35	2.83 ± 0.55
24	346	U1425	D	6	H	1	0	39.68	14.69 ± 0.49	3.03 ± 0.91	13.99 ± 0.51	61.31 ± 1.87	2.28 ± 1.06	6.54 ± 1.72
25	346	U1425	D	6	H	2	50	58.31	26.20 ± 0.26	39.67 ± 0.56	17.80 ± 0.30	12.60 ± 0.87	1.48 ± 0.25	3.97 ± 0.76
26	346	U1425	D	6	H	3	100	49.34	18.17 ± 2.13	42.64 ± 3.36	13.44 ± 2.00	3.71 ± 2.28	19.85 ± 1.93	2.61 ± 0.57
27	346	U1425	D	6	H	5	0	60.71	14.35 ± 0.20	60.26 ± 0.90	0.85 ± 0.08	23.98 ± 1.10	1.06 ± 0.56	1.89 ± 0.62
28	346	U1425	D	6	H	6	50	50.86	40.66 ± 0.54	35.51 ± 0.47	28.77 ± 0.44	0.00 ± 0.00	1.02 ± 0.26	1.86 ± 0.46
29	346	U1425	D	7	H	1	0	52.61	28.54 ± 1.52	14.49 ± 2.29	34.13 ± 1.34	4.89 ± 1.43	14.06 ± 1.44	2.54 ± 0.59
30	346	U1425	D	7	H	2	50	50.66	21.75 ± 0.41	16.74 ± 0.39	36.09 ± 0.20	17.76 ± 0.69	2.05 ± 0.17	3.30 ± 0.75
31	346	U1425	D	7	H	3	100	49.06	0.00 ± 0.00	52.09 ± 0.72	19.99 ± 0.55	20.33 ± 1.21	0.47 ± 0.51	2.34 ± 0.62
32	346	U1425	D	7	H	5	4	47.15	24.95 ± 0.22	70.73 ± 0.91	0.00 ± 0.00	7.20 ± 0.91	1.19 ± 0.50	1.38 ± 0.32
33	346	U1425	D	7	H	6	50	46.21	22.29 ± 0.75	24.58 ± 1.21	28.93 ± 0.63	10.63 ± 0.90	6.96 ± 0.67	3.05 ± 0.62
34	346	U1425	D	8	H	1	100	47.09	39.43 ± 0.43	38.47 ± 0.45	16.65 ± 0.45	3.07 ± 0.22	0.85 ± 0.18	2.26 ± 0.37
35	346	U1425	D	8	H	2	50	57.10	12.17 ± 0.05	55.55 ± 0.71	15.83 ± 0.45	13.36 ± 1.04	0.54 ± 0.45	2.79 ± 0.59
36	346	U1425	D	8	H	3	101	46.61	31.70 ± 0.28	62.17 ± 0.84	0.08 ± 0.21	4.55 ± 0.72	1.74 ± 0.40	1.96 ± 0.33
37	346	U1425	D	8	H	5	2	52.53	16.01 ± 0.25	52.65 ± 0.87	7.80 ± 0.24	22.31 ± 1.23	2.12 ± 0.45	3.62 ± 0.79
38	346	U1425	D	8	H	6	50	53.38	27.34 ± 0.32	32.67 ± 0.46	21.17 ± 0.24	13.24 ± 0.65	1.34 ± 0.19	3.26 ± 0.63
39	346	U1425	D	9	H	1	0	55.63	5.90 ± 0.14	51.64 ± 0.79	12.49 ± 0.30	23.96 ± 1.12	1.32 ± 0.45	2.14 ± 0.57
40	346	U1425	D	9	H	2	50	53.64	12.10 ± 0.17	51.26 ± 0.77	16.30 ± 0.30	16.97 ± 0.97	1.76 ± 0.39	2.30 ± 0.51
41	346	U1425	D	9	H	3	101	58.68	1.25 ± 0.24	49.56 ± 0.83	5.76 ± 0.33	35.31 ± 1.13	0.62 ± 0.62	0.75 ± 0.65
42	346	U1425	D	9	H	5	1	53.62	10.14 ± 0.16	51.94 ± 0.76	7.20 ± 0.13	24.71 ± 0.98	0.64 ± 0.50	1.53 ± 0.53
43	346	U1425	D	9	H	6	50	51.22	20.79 ± 0.17	58.70 ± 0.79	9.38 ± 0.27	8.93 ± 0.85	1.42 ± 0.41	2.24 ± 0.42
44	346	U1425	D	10	H	1	100	60.16	13.32 ± 0.28	29.79 ± 0.71	17.88 ± 0.27	32.74 ± 1.58	2.46 ± 0.44	5.73 ± 1.24
45	346	U1425	D	10	H	2	51	54.16	13.44 ± 0.24	34.35 ± 0.76	13.08 ± 0.26	34.07 ± 1.69	1.96 ± 0.51	6.04 ± 1.32
46	346	U1425	D	10	H	3	101	49.63	14.56 ± 0.16	54.15 ± 0.78	10.34 ± 0.19	18.36 ± 0.98	1.37 ± 0.42	2.27 ± 0.52
47	346	U1425	D	10	H	5	1	51.78	17.50 ± 0.23	37.99 ± 0.76	6.56 ± 0.13	30.52 ± 1.45	1.55 ± 0.53	5.23 ± 1.16
48	346	U1425	D	10	H	6	51	65.05	8.18 ± 0.26	24.34 ± 0.76	16.02 ± 0.25	42.77 ± 1.93	1.97 ± 0.60	6.77 ± 1.54
49	346	U1425	D	11	H	1	30	53.11	5.54 ± 0.11	44.50 ± 0.72	16.35 ± 0.37	28.30 ± 1.34	1.12 ± 0.43	3.72 ± 0.87
50	346	U1425	D	11	H	2	50	53.50	12.32 ± 0.43	13.83 ± 1.05	7.55 ± 0.13	56.60 ± 2.59	2.73 ± 0.98	9.49 ± 2.18
51	346	U1425	D	11	H	3	101	49.39	5.52 ± 0.16	31.01 ± 0.61	32.82 ± 0.58	29.08 ± 1.56	2.15 ± 0.28	5.37 ± 1.20
52	346	U1425	D	11	H	5	1	49.96	19.45 ± 0.30	23.69 ± 0.67	14.06 ± 0.14	34.21 ± 1.54	2.07 ± 0.53	6.02 ± 1.31
53	346	U1425	D	11	H	6	51	57.26	14.36 ± 0.15	36.52 ± 0.52	27.32 ± 0.53	14.99 ± 1.16	1.28 ± 0.27	4.55 ± 0.97
54	346	U1425	D	12	H	1	0	48.68	16.21 ± 0.28	29.56 ± 0.62	20.57 ± 0.15	28.97 ± 1.23	2.15 ± 0.37	4.53 ± 0.98
55	346	U1425	D	12	H	2	51	54.60	19.16 ± 0.26	36.67 ± 0.64	21.64 ± 0.29	18.91 ± 1.06	2.25 ± 0.28	4.15 ± 0.84
56	346	U1425	D	12	H	3	96	54.38	1.18 ± 0.07	51.57 ± 0.73	18.43 ± 0.50	23.98 ± 1.25	0.53 ± 0.48	2.70 ± 0.67
57	346	U1425	D	13	X	1	51	39.54	8.37 ± 0.15	37.58 ± 0.67	19.22 ± 0.39	28.81 ± 1.46	1.65 ± 0.38	4.85 ± 1.07
58	346	U1425	D	13	X	3	51	37.19	13.61 ± 0.23	21.97 ± 0.42	30.49 ± 0.26	25.36 ± 1.16	1.52 ± 0.21	4.54 ± 1.00
59	346	U1425	D	13	X	5	50	38.07	19.16 ± 0.31	20.87 ± 0.31	35.78 ± 0.30	15.41 ± 0.85	1.08 ± 0.13	3.89 ± 0.89
60	346	U1425	D	13	X	7	50	55.56	5.94 ± 0.07	41.06 ± 0.61	18.74 ± 0.32	26.31 ± 1.17	0.53 ± 0.40	3.23 ± 0.77
61	346	U1425	D	14	H	1	50	53.38	7.03 ± 0.10	39.41 ± 0.66	20.15 ± 0.44	27.73 ± 1.44	1.31 ± 0.37	4.64 ± 1.03
62	346	U1425	D	14	H	3	50	59.49	7.99 ± 0.09	39.05 ± 0.62	24.70 ± 0.51	24.45 ± 1.39	1.39 ± 0.33	4.65 ± 1.02
63	346	U1425	D	15	H	1	50	29.13	20.04 ± 0.35	15.84 ± 0.29	36.96 ± 0.23	20.77 ± 0.95	1.36 ± 0.12	4.29 ± 0.95
64	346	U1425	D	15	H	3	50	41.35	7.45 ± 0.09	35.60 ± 0.56	27.41 ± 0.58	22.95 ± 1.42	1.34 ± 0.29	4.95 ± 1.08
65	346	U1425	D	15	H	5	50	46.99	2.41 ± 0.07	37.65 ± 0.59	31.15 ± 0.65	22.13 ± 1.33	1.39 ± 0.33	4.14 ± 0.96
66	346	U1425	D	15	H	7	50	31.87	2.41 ± 0.07	37.65 ± 0.59	31.15 ± 0.65	22.13 ± 1.33	1.39 ± 0.33	4.14 ± 0.96
67	346	U1425	D	16	H	1	50	44.79	6.28 ± 0.12	32.49 ± 0.59	25.32 ± 0.47	28.46 ± 1.48	1.56 ± 0.31	5.03 ± 1.11
68	346	U1425	D	16	H	3	53	45.51	10.48 ± 0.17	28.67 ± 0.47	33.51 ± 0.46	21.38 ± 1.19	1.43 ± 0.22	4.44 ± 1.00
69	346	U1425	D	16	H	5	53	37.09	13.07 ± 0.32	6.22 ± 0.48	31.97 ± 0.11	41.57 ± 1.59	1.96 ± 0.49	6.08 ± 1.37
70	346	U1425	D	16	H	7	50	43.37	16.91 ± 0.28	15.31 ± 0.44	28.19 ± 0.15	32.12 ± 1.37	1.67 ± 0.35	5.53 ± 1.20
71	346	U1425	D	18	H	1	50	39.44	11.49 ± 0.23	12.10 ± 0.36	37.86 ± 0.36	31.63 ± 1.56	1.61 ± 0.23	6.11 ± 1.35
72	346	U1425	D	18	H	3	50	45.35	10.19 ± 0.16	19.47 ± 0.52	27.51 ± 0.43	34.31 ± 1.83	1.60 ± 0.36	6.97 ± 1.50
73	346	U1425	D	18	H	5	50	43.98	13.51 ± 0.32	3.35 ± 0.50	34.89 ± 0.12	45.43 ± 1.82	1.82 ± 0.54	7.05 ± 1.58
74	346	U1425	D	18	H	7	50	52.83	13.74 ± 0.27	12.63 ± 0.67	19.72 ± 0.13	43.64 ± 1.92	1.83 ± 0.63	7.30 ± 1.63
75	346	U1425	D	19	H	1	50	39.08	13.65 ± 0.30	6.97 ± 0.74	18.79 ± 0.12	51.02 ± 1.98	1.48 ± 0.80	7.42 ± 1.72
76	346	U1425	D	19	H	3	50	47.55	12.11 ± 0.20	22.98 ± 0.51	28.72 ± 0.41	29.60 ± 1.58	1.92 ± 0.29	6.07 ± 1.30
77	346	U1425	D	19	H	5	50	56.39	11.76 ± 0.19	28.85 ± 0.52	30.54 ± 0.46	22.84 ± 1.31	1.90 ± 0.23	4.94 ± 1.07
78	346	U1425	D	19	H	7	50	53.07	11.48 ± 0.23	16.94 ± 0.42	35.93 ± 0.38	29.15 ± 1.46	1.95 ± 0.22	5.66 ± 1.25
79	346	U1425	D	20	H	1	50	58.04	7.54 ± 0.14	24.55 ± 0.54	26.29 ± 0.40	32.67 ± 1.61	1.59 ± 0.34	5.80 ± 1.28
80	346	U1425	D	20	H	3	50	53.47	16.43 ± 0.26	14.68 ± 0.74	15.25 ± 0.16	44.21 ± 2.05	1.48 ± 0.70	7.94 ± 1.75
81	346	U1425	D	20	H	5	51	45.38	11.01 ± 0.22	12.98 ± 0.53	30.26 ± 0.34	39.56 ± 1.93	1.83 ± 0.43	7.39 ± 1.61
82	346	U1425	D	20	H	7	50	51.19	8.86 ± 0.20	18.41 ± 0.55	30.62 ± 0.48	35.65 ± 1.90	2.11 ± 0.35	7.14 ± 1.55
83	346	U1425	D	21	H	1	70	58.03	9.86 ± 0.21	17.99 ± 0.48	32.64 ± 0.37	32.41 ± 1.56	1.97 ± 0.28	5.88 ± 1.29
84	346	U1425	D	21	H	3	50	55.66	10.30 ± 0.24	13.97 ± 0.59	26.21 ± 0.38	38.61 ± 1.99	2.20 ± 0.46	7.56 ± 1.64
85	346	U1425	D	21	H	5	50	53.73	11.97 ± 0.22	16.65 ± 0.50	30.38 ± 0.34	34.29 ± 1.69	1.93 ± 0.34	6.53 ± 1.42
86	346	U1425	D	22	H	1	50	53.30	8.70 ± 0.30	12.90 ± 0.88	16.80 ± 0.26	53.79 ± 2.53	1.96 ± 0.82	9.28 ± 2.09
87	346	U1425	D	22	H	3	50	42.33	11.16 ± 0.32	9.77 ± 0.85	17.40 ± 0.18	52.70 ± 2.42	2.13 ± 0.82	9.03 ± 2.03
88	346	U1425	D	22	H	5	51	58.27	9.81 ± 0.30	12.16 ± 0.83	17.86 ± 0.21	51.60 ± 2.37	2.08 ± 0.77	8.73 ± 1.97
89	346	U1425	D	22	H	7	50	55.11	10.92 ± 0.28	5.07 ± 0.69	24.34 ± 0.10	50.74 ± 2.12	1.69 ± 0.72	7.93 ± 1.80
90	346	U1425	D	23	H	1	50	54.55	11.90 ± 0.26	9.49 ± 0.47	36.12 ± 0.44	35.20 ± 1.90	2.42 ± 0.33	7.49 ± 1.61

91	346	U1425	D	23	H	3	50	51.80	11.44	±	0.16	23.19	±	0.57	21.05	±	0.22	35.85	±	1.60	1.14	±	0.45	5.89	± 1.31
92	346	U1425	D	23	H	5	50	54.77	15.83	±	0.31	9.67	±	0.33	34.81	±	0.14	31.79	±	1.27	1.50	±	0.29	5.14	± 1.14
93	346	U1425	D	23	H	7	50	45.38	15.25	±	0.25	13.70	±	0.65	18.98	±	0.10	42.56	±	1.80	1.41	±	0.63	6.91	± 1.55
94	346	U1425	D	24	H	1	50	39.31	12.14	±	0.20	23.07	±	0.65	18.38	±	0.29	37.03	±	1.84	1.66	±	0.50	6.87	± 1.50
95	346	U1425	D	24	H	3	50	42.06	11.46	±	0.21	23.31	±	0.44	38.38	±	0.54	20.19	±	1.27	1.79	±	0.20	5.00	± 1.13
96	346	U1425	D	24	H	5	51	35.14	14.58	±	0.30	8.34	±	0.88	13.07	±	0.11	53.46	±	2.34	1.42	±	0.91	8.88	± 2.02
97	346	U1425	D	24	H	7	54	40.15	5.05	±	0.10	32.28	±	0.58	25.74	±	0.48	28.46	±	1.45	1.46	±	0.31	4.80	± 1.08
98	346	U1425	D	25	H	1	50	41.03	12.57	±	0.23	7.52	±	0.59	29.01	±	0.18	46.69	±	2.04	1.28	±	0.60	7.82	± 1.74
99	346	U1425	D	25	H	3	50	53.84	5.69	±	0.14	23.51	±	0.48	33.99	±	0.49	28.80	±	1.45	1.70	±	0.23	5.15	± 1.17
100	346	U1425	D	26	X	1	50	35.29	13.64	±	0.32	12.45	±	0.31	48.02	±	0.44	22.01	±	1.22	1.58	±	0.15	5.05	± 1.21
101	346	U1425	D	26	X	3	50	52.90	1.76	±	0.06	31.97	±	0.54	33.96	±	0.71	27.91	±	1.62	1.36	±	0.29	5.44	± 1.24
102	346	U1425	D	26	X	5	50	39.03	11.25	±	0.19	15.86	±	0.31	36.93	±	0.42	28.05	±	1.48	0.89	±	0.17	5.82	± 1.29
103	346	U1425	D	26	X	7	50	41.15	13.74	±	0.29	10.28	±	0.26	42.93	±	0.34	28.11	±	1.38	1.31	±	0.14	5.63	± 1.27
104	346	U1425	D	27	H	1	50	50.62	13.70	±	0.26	16.35	±	0.35	39.19	±	0.39	25.44	±	1.33	1.62	±	0.15	5.37	± 1.20
105	346	U1425	D	27	H	3	50	32.88	16.05	±	0.34	12.93	±	0.28	45.77	±	0.37	21.30	±	1.13	1.37	±	0.12	4.80	± 1.13
106	346	U1425	D	28	H	1	50	58.00	5.72	±	0.11	29.58	±	0.57	27.19	±	0.53	31.60	±	1.68	1.48	±	0.33	5.90	± 1.30
107	346	U1425	D	28	H	3	51	56.22	3.90	±	0.13	29.47	±	0.59	30.60	±	0.64	30.11	±	1.72	1.92	±	0.29	5.96	± 1.32
108	346	U1425	D	28	H	5	51	54.03	9.99	±	0.17	24.30	±	0.48	31.40	±	0.43	27.16	±	1.42	1.70	±	0.23	5.32	± 1.17
109	346	U1425	D	28	H	7	50	50.67	11.69	±	0.17	16.32	±	0.48	28.66	±	0.39	34.26	±	1.79	1.46	±	0.35	6.96	± 1.50
110	346	U1425	D	29	H	1	50	52.86	7.15	±	0.13	29.90	±	0.56	27.71	±	0.48	29.02	±	1.51	1.65	±	0.29	5.31	± 1.17
111	346	U1425	D	29	H	3	50	41.63	9.24	±	0.20	9.83	±	0.67	24.50	±	0.27	47.46	±	2.22	1.37	±	0.63	8.32	± 1.85
112	346	U1425	D	30	H	1	50	48.67	7.73	±	0.11	24.34	±	0.50	30.29	±	0.52	31.71	±	1.72	1.38	±	0.29	6.34	± 1.39
113	346	U1425	D	30	H	3	50	62.88	17.21	±	0.20	20.52	±	0.66	15.38	±	0.24	37.73	±	1.90	1.21	±	0.57	7.48	± 1.61
114	346	U1425	D	30	H	5	51	59.20	9.49	±	0.10	31.81	±	0.57	22.42	±	0.50	27.49	±	1.60	1.30	±	0.32	5.83	± 1.25
115	346	U1425	D	30	H	7	50	62.14	15.30	±	0.17	18.31	±	0.47	22.08	±	0.24	31.47	±	1.53	0.95	±	0.39	6.08	± 1.30
116	346	U1425	D	31	H	1	0	65.68	13.99	±	0.20	16.08	±	0.68	16.06	±	0.21	41.24	±	1.97	1.13	±	0.62	7.57	± 1.66
117	346	U1425	D	31	H	2	50	62.52	6.81	±	0.16	33.82	±	0.72	14.84	±	0.46	35.18	±	1.87	1.23	±	0.49	6.47	± 1.43
118	346	U1425	D	31	H	3	100	44.34	13.37	±	0.18	22.90	±	0.31	31.98	±	0.42	21.83	±	1.24	0.34	±	0.18	4.96	± 1.09
119	346	U1425	D	31	H	5	0	52.27	9.72	±	0.10	29.51	±	0.47	27.15	±	0.47	23.95	±	1.36	1.10	±	0.25	5.03	± 1.09
120	346	U1425	D	31	H	6	50	62.03	10.62	±	0.08	31.57	±	0.47	26.26	±	0.65	20.99	±	1.56	0.87	±	0.25	5.98	± 1.26
121	346	U1425	D	32	H	1	50	64.88	6.49	±	0.09	31.57	±	0.62	17.89	±	0.48	32.49	±	1.76	0.73	±	0.43	6.17	± 1.36
122	346	U1425	D	32	H	2	51	60.09	6.89	±	0.13	25.78	±	0.67	17.46	±	0.48	38.05	±	2.06	0.77	±	0.51	7.47	± 1.64
123	346	U1425	D	32	H	3	50	60.58	10.52	±	0.19	26.00	±	0.36	39.03	±	0.56	21.32	±	1.30	0.64	±	0.21	5.01	± 1.15
124	346	U1425	D	32	H	5	49	60.51	9.40	±	0.22	23.30	±	0.85	8.98	±	0.22	47.01	±	2.16	0.79	±	0.77	7.74	± 1.78
125	346	U1425	D	32	H	6	51	62.60	7.41	±	0.14	22.84	±	0.66	17.12	±	0.28	40.32	±	1.84	0.79	±	0.56	6.54	± 1.48
126	346	U1425	D	33	H	1	50	43.75	13.29	±	0.24	19.81	±	0.30	37.78	±	0.39	20.03	±	1.07	0.83	±	0.14	4.35	± 1.01
127	346	U1425	D	33	H	2	50	52.35	14.99	±	0.27	19.55	±	0.29	38.92	±	0.37	18.95	±	1.01	0.84	±	0.13	4.24	± 0.99
128	346	U1425	D	33	H	4	50	58.75	11.84	±	0.13	19.26	±	0.46	25.67	±	0.31	33.10	±	1.60	0.63	±	0.37	6.12	± 1.34
129	346	U1425	D	35	H	1	6	44.15	9.10	±	0.51	5.40	±	1.39	0.00	±	0.00	74.33	±	3.36	2.14	±	1.41	12.14	± 2.88
130	346	U1425	D	35	H	2	50	22.36	15.22	±	0.43	7.44	±	0.22	53.17	±	0.36	20.23	±	1.02	0.20	±	0.13	4.26	± 1.13
131	346	U1425	D	35	H	3	54	37.71	5.96	±	0.10	21.14	±	0.40	34.01	±	0.55	32.22	±	1.73	0.33	±	0.28	6.36	± 1.42
132	346	U1425	D	36	H	1	50	40.39	8.52	±	0.14	14.25	±	0.38	35.15	±	0.42	34.39	±	1.71	0.85	±	0.28	6.49	± 1.44
133	346	U1425	D	36	H	2	50	28.76	12.75	±	0.33	9.75	±	0.18	44.81	±	0.29	27.24	±	1.18	0.15	±	0.10	4.69	± 1.12
134	346	U1425	D	36	H	3	50	20.45	13.69	±	0.48	1.17	±	0.20	54.04	±	0.19	25.38	±	0.91	0.00	±	0.00	3.56	± 1.00
135	346	U1425	D	37	H	1	0	25.30	10.72	±	0.44	8.44	±	0.33	60.92	±	0.48	19.93	±	1.07	0.35	±	0.25	4.12	± 1.22
136	346	U1425	D	37	H	2	51	51.46	0.00	±	0.00	26.35	±	0.50	36.12	±	0.68	28.82	±	1.50	1.55	±	0.27	4.90	± 1.16
137	346	U1425	D	37	H	4	50	24.65	9.65	±	0.23	13.80	±	0.26	41.77	±	0.42	29.61	±	1.44	0.39	±	0.16	5.56	± 1.28
138	346	U1425	D	37	H	5	50	64.85	7.65	±	0.07	23.62	±	0.56	26.19	±	0.56	37.24	±	2.08	0.41	±	0.43	7.71	± 1.68
139	346	U1425	D	37	H	7	54	49.25	0.15	±	0.06	30.00	±	0.56	29.37	±	0.59	32.99	±	1.65	1.23	±	0.33	5.32	± 1.22
140	346	U1425	D	38	H	1	50	46.69	9.47	±	0.15	16.48	±	0.47	31.30	±	0.34	38.42	±	1.78	0.85	±	0.39	6.66	± 1.48
141	346	U1425	D	38	H	2	50	44.13	8.59	±	0.13	18.31	±	0.44	32.70	±	0.41	35.29	±	1.72	1.01	±	0.32	6.42	± 1.42
142	346	U1425	D	38	H	3	54	31.77	14.30	±	0.35	10.60	±	0.20	45.49	±	0.26	25.10	±	1.07	0.60	±	0.07	4.39	± 1.06
143	346	U1425	D	39	H	1	50	18.59	13.96	±	0.46	4.36	±	0.19	50.02	±	0.15	27.08	±	0.80	0.00	±	0.01	3.08	± 0.86
144	346	U1425	D	39	H	2	50	48.97	10.95	±	0.24	13.82	±	0.83	16.89	±	0.19	51.97	±	2.36	1.24	±	0.80	8.74	± 1.98
145	346	U1425	D	39	H	3	54	35.36	6.80	±	0.25	8.01	±	0.65	23.08	±	0.11	48.23	±	1.86	1.63	±	0.65	6.63	± 1.56
146	346	U1425	D	40	H	1	50	24.13	12.24	±	0.29	5.95	±	0.29	37.40	±	0.11	35.60	±	1.30	0.88	±	0.32	5.04	± 1.16
147	346	U1425	D	40	H	2	51	28.52	11.56	±	0.42	4.88	±	0.22	56.76	±	0.31	26.22	±	1.09	0.53	±	0.08	4.26	± 1.15
148	346	U1425	D	40	H	3	100	35.74	13.61	±	0.26	13.91	±	0.76	17.91	±	0.08	49.57	±	2.06	1.32	±	0.76	7.71	± 1.76
149	346	U1425	D	41	H	1	50	54.77	6.78	±	0.19	18.09	±	0.78	18.18	±	0.40	48.01	±	2.39	1.12	±	0.68	8.72	± 1.95
150	346	U1425	D	41	H	2	50	30.78	10.60	±	0.20	14.73	±	0.33	35.96	±	0.31	31.49	±	1.43	0.91	±	0.23	5.50	± 1.24
151	346	U1425	D	41	H	3	50	42.19	5.26	±	0.16	19.49	±	0.71	19.32	±	0.28	46.76	±	2.04	0.82	±	0.64	7.13	± 1.65
152	346	U1425	D	42	H	1	50	42.63	8.85	±	0.13	17.70	±	0.44	29.95	±	0.34	34.91	±	1.63	0.92	±	0.34	6.05	± 1.35
153	346	U1425	D	42	H	2	50	37.20	10.01	±	0.23	14.22	±	0.26	41.62	±	0.42	26.26	±	1.32	0.83	±	0.12	5.14	± 1.19
154	346	U1425	D	42	H	3	54	52.29	6.13	±	0.13	22.50	±	0.39	35.71	±	0.47	27.86	±	1.38	0.93	±	0.21	4.92	± 1.13
155	346	U1425	D	43	H	1	50	48.42	8.65	±	0.18	16.64	±	0.61	23.36	±	0.21	43.11	±	1.83	1.20	±	0.55	6.65	± 1.51
156	346	U1425	D	43	H	2	50	49.53	3.45	±	0.10	24.63	±	0.58	24.75	±	0.38	38.85	±	1.73	0.96	±	0.44	5.83	± 1.34
157	346	U1425	D	43	H	3	54	35.96	8.76	±	0.11	19.14	±	0.48	30.28	±	0.43	36.68	±	1.84	0.68	±	0.37	6.88	± 1.52
158	346	U1425	D	43	H	5	1	40.48	9.24	±	0.19	12.85	±	0.33	36.16	±	0.31	33.20	±	1.48	0.74	±	0.26	5.60	± 1.27
159	346	U1425	D	43	H	6	50	44.92	10.77	±	0.16	16.91	±	0.37	34.49	±	0.40	32.83	±	1.65	0.61	±	0.28	6.35	± 1.40
160	346	U1425	D	44	H	1	50	67.81	6.20	±	0.10	26.34	±	0.42	35.48	±	0.70	24.42	±	1.61	1.03	±	0.22	5.95	± 1.32
161	346	U1425	D	44	H	2	50	54.15	6.42	±	0.14	18.93	±	0.47	30.49	±	0.42	32.47	±	1.59	1.59	±	0.29	5.77	± 1.29
162	346	U1425	D	44	H	3	50	50.03	0.01	±	0.03	30.62	±	0.60	26.38	±	0.52	38.03	±	1.81	0.44	±	0.44	5.86	± 1.36
163	346	U1425	D	45	H	1	0	70.72	2.02	±	0.05	33.87	±	0.59	24.54	±	0.50	32.77	±	1.58	0.64	±	0.39	5.02	± 1.16
164	346	U1425	D	45	H	2	51	69.45	2.01	±	0.03	34.01	±	0.55	29.67	±	0.62	30.18	±	1.61	0.71	±	0.34	5.27	± 1.20
165	346	U1425	D	45	H	3	54	50.48	13.08	±	0.27	21.06	±	0.30	45.68	±	0.68	16.53	±	1.35	0.63	±	0.24	5.58	± 1.32
166	346	U1425	D	46	H	1	50	47.22	4.22	±	0.08	22.74	±	0.46	33.15	±	0.77	31.97	±	2.06	0.83	±	0.28	7.64	± 1.66
167	346	U1425	D	46	H	2	50	14.90	12.10	±	0.31	17.36	±	0.26	51.12	±	0.77	18.14	±	1.53	0.31	±	0.24	6.26	± 1.49
168	346	U1425	D	46	H	3	50	36.41	9.91	±	0.29	19.05	±	0.28	47.65	±	0.69	16.84	±	1.31	0.17	±	0.23	5.21	± 1.29
169	346	U1425	D	47	H	1	0	24.77	3.58	±	0.21	26.88	±	0.38	46.17	±	1.12	17.88	±	1.90	0.74	±	0.35	7.19	± 1.66
170	346	U1425	D	47	H	2	49	33.75	3.07	±	0.80	17.35	±	0.53	38.36	±	2.81	18.74	±	5.20	0.75	±	0.31	20.83	± 4.22
171	346	U1425	D	47	H	3	54	29.19	6.98	±	1.90	7.90	±	1.39	21.22	±	5.49	16.84	±	10.45	2.34	±	0.48	42.46	± 8.29
172	346	U1425	D	48	H	1	50	29.52	3.37	±	1.54	11.84	±	0.98	32.59	±	4.71	14.47	±	8.63	2.44	±	0.44	34.98	± 6.90
173	346	U1425	D	48	H	2	51	44.14	1.71	±	0.76	27.44	±	0.51	39.44	±	2.73	13.99	±	4.70	1.82	±	0.44	18.75	± 3.81
174	346	U1425	D	49	H	1	23	42.25	8.70	±	1.11	12.52	±	0.58	41.92	±	3.74	9.96	±	6.68	1.33	±	0.43	27.32	± 5.46
175	346	U1425	D	48	H	3	54	17.04	12.76	±	0.44	0.05	±	0.10	56.59	±	1.79	16.41	±	3.49	0.72	±	0.28	14.54	± 3.08
176	346	U1425	D	49	H	2	50	40.16	5.86	±	2.01	11.88	±	1.31	24.49	±	5.88	9.66	±	10.75	1.82	±	0.52	43.71	± 8.54
177	346	U1425	D	49	H	3	99	42.33	5.22	±	1.92	9.40	±	1.19	30.40	±	5.71	9.69	±	10.38	2.18	±	0.53	42.21	± 8.28
178	346	U1425	D	50	H	1	50	36.72	7.23	±	0.27	24.97	±	0.35	47.50	±	1.23	12.45	±	1.97	0.82	±	0.40	7.85	± 1.79
179	346	U1425	D	50	H	2	48	38.25	11.86	±	0.44	5.59	±	0.37	66.98	±	0.97	13.11	±	1.66	0.67	±	0.41	6.85	± 1.79
180	346	U1425	D	50	H	3	50	33.41	12.46	±	0.28	16.85	±	0.32	50.10	±	0.88	14.05	±	1.59	1.21	±	0.30	6.65	± 1.56

Appendix 1:
The PARAFAC modelling steps, matrix calculation and RSS comparison.

Step 1: Arrange the data as EEMs

Worksheet for arrange XRD data to EEM formats for model processing

The 180 samples XRD data was arrange in a threeway structure as the excitation emission matrices (EEMs) for model processing

mod_silt0	200	300	400	500	600	700	800	900	1000	1100	1200	1300	1400	1500
2.02	932	0	0	0	0	0	0	0	0	0	0	0	0	0
2.04	965	0	0	0	0	0	0	0	0	0	0	0	0	0
2.06	889	0	0	0	0	0	0	0	0	0	0	0	0	0
2.08	865	0	0	0	0	0	0	0	0	0	0	0	0	0
2.1	803	0	0	0	0	0	0	0	0	0	0	0	0	0
2.12	722	0	0	0	0	0	0	0	0	0	0	0	0	0
2.14	680	0	0	0	0	0	0	0	0	0	0	0	0	0
2.16	648	0	0	0	0	0	0	0	0	0	0	0	0	0
2.18	655	0	0	0	0	0	0	0	0	0	0	0	0	0
2.2	585	0	0	0	0	0	0	0	0	0	0	0	0	0
2.22	570	0	0	0	0	0	0	0	0	0	0	0	0	0
2.24	548	0	0	0	0	0	0	0	0	0	0	0	0	0
2.26	545	0	0	0	0	0	0	0	0	0	0	0	0	0
2.28	510	0	0	0	0	0	0	0	0	0	0	0	0	0
2.3	499	0	0	0	0	0	0	0	0	0	0	0	0	0
2.32	474	0	0	0	0	0	0	0	0	0	0	0	0	0
2.34	443	0	0	0	0	0	0	0	0	0	0	0	0	0
2.36	502	0	0	0	0	0	0	0	0	0	0	0	0	0
2.38	446	0	0	0	0	0	0	0	0	0	0	0	0	0
2.4	466	0	0	0	0	0	0	0	0	0	0	0	0	0
2.42	420	0	0	0	0	0	0	0	0	0	0	0	0	0
2.44	407	0	0	0	0	0	0	0	0	0	0	0	0	0
2.46	402	0	0	0	0	0	0	0	0	0	0	0	0	0
2.48	411	0	0	0	0	0	0	0	0	0	0	0	0	0
2.5	406	0	0	0	0	0	0	0	0	0	0	0	0	0
2.52	415	0	0	0	0	0	0	0	0	0	0	0	0	0
2.54	409	0	0	0	0	0	0	0	0	0	0	0	0	0
2.56	370	0	0	0	0	0	0	0	0	0	0	0	0	0
2.58	372	0	0	0	0	0	0	0	0	0	0	0	0	0
2.6	365	0	0	0	0	0	0	0	0	0	0	0	0	0
2.62	412	0	0	0	0	0	0	0	0	0	0	0	0	0
2.64	409	0	0	0	0	0	0	0	0	0	0	0	0	0
2.66	379	0	0	0	0	0	0	0	0	0	0	0	0	0
2.68	393	0	0	0	0	0	0	0	0	0	0	0	0	0

Step 2: Input the data and start model developing

Model development by using **MATLAB software and drEEM toolboxes**

MatLab for PARAFAC analysis commands for U1425 sediment unmixing analysis

(List of commands on MatLab)

Silt 6M_IE8_

```
>> filetype=1;ext='txt';range='A1..AU1901';headers=[1 1];display=0;outdata=0;
>> [X, Emmat, Exmat, filelist_U1425_Silt, outdata] = readineems(filetype, ext, range, headers, display, outdata);
mod_silt001.txt
mod_silt002.txt
mod_silt003.txt
mod_silt004.txt
mod_silt005.txt
mod_silt006.txt
mod_silt007.txt
to
mod_silt180.txt

>> Ex = Exmat(1,:) ;  Em = Emmat(:,1);
>> mydataU1425_Silt=assembledataset(X,Ex,Em,'QSE');
>> mydataU1425_Silt=subdataset(mydataU1425_Silt,[],[],mydataU1425_Silt.Ex>400);
>> TestU1425_Silt=outliertest(mydataU1425_Silt,[],6,'nonnegativity',[1e-8],'atonece');
```

Step 3: Develop preliminary models

PARAFAC Model report

Model development was initiated with a series of 2 to 7 components by using the excitation emission matrices (EEMs) dataset of the 180 samples with the non-negativity constraint and default convergence criterion (0.01) for the outlier tests. **A stricter convergence (10^{-8}) is applied in the 4-7 component.**

PARAFAC Model Report								
Info								
	Toolbox	drEEM 0.3.0						
	Date	31/07/2020 14:56						
Preprocessing								
	nSample - full dataset	180						
	nSample - modeled dat	180						
	No. excluded samples	0						
	Excluded samples -indices							
	Scatter Removal							
	Zapped (Samples,EmRange,ExRange)							
	Fluorescence unit	QSE						
	Scaling							
PARAFAC model								
	No. PARAFAC compone	6						
	No. Ex wavelengths	3						
	OutlierTest_convgcrit	0.00000001						
	OutlierTest_constraints	nonnegativity						
Spectra								
	mode	nm	Comp1	Comp2	Comp3	Comp4	Comp5	Comp6
	Ex	200	1	1	1	1	1	1
	Ex	300	0	0	0	0	0	0
	Ex	400	0	0	0	0	0	0
	Em	2.02	0.039486	0.033532	0.070343	0.11218	0.112119	0.060315
	Em	2.04	0.038537	0.030702	0.067144	0.109392	0.109618	0.055372
	Em	2.06	0.034889	0.030136	0.063539	0.104493	0.105116	0.054163
	Em	2.08	0.033239	0.02814	0.060897	0.099175	0.099986	0.049822
	Em	2.1	0.032502	0.024106	0.05594	0.096556	0.099765	0.049842
	Em	2.12	0.030289	0.02574	0.055006	0.090509	0.094418	0.045178
	Em	2.14	0.028573	0.021403	0.051992	0.087068	0.093391	0.042494
	Em	2.16	0.027273	0.021776	0.048182	0.084001	0.087887	0.040506
	Em	2.18	0.02485	0.019969	0.046249	0.082464	0.082635	0.040008

Step 4: Matrix calculation of actual intensity and score of each end-member

Scaling factors calculation

Fmax is calculated by multiplying the maximum excitation loading and maximum emission loading for each component by its score, producing intensities in the same measurement scale as the original EEMs (Murphy et al., 2013).

To calculate absolute contributions and intensities of spectral loadings for each end-member, (Fmax) and spectral loadings (Em) from model are adjusted by the scaling factors (α1-6) with the definition,
S (samples)=F (spectral loadings, Em)*W (Fmax)).

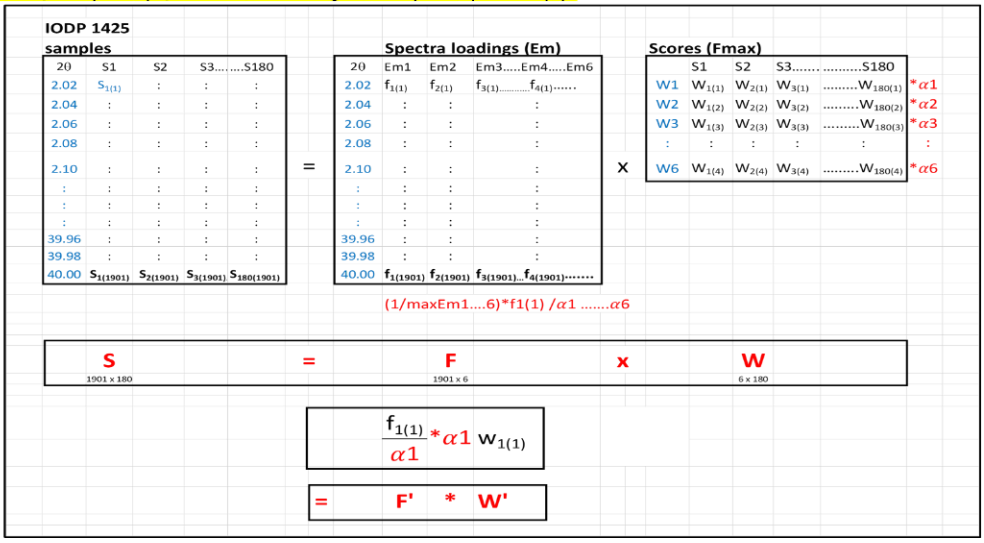

Scaling factors

Scaling factors (α 1-6) for each component/end-member are calculated by the equation (2).

$$\left(W * {}^{t}W\right)^{-1} * \left(W * {}^{t}W\right)\begin{pmatrix}\alpha 1\\ \alpha 2\\ \alpha 3\\ \alpha 4\\ \alpha 5\\ \alpha 6\end{pmatrix} = \left(W * {}^{t}W\right)^{-1} * W * \begin{pmatrix}1\\ .\\ .\\ .\\ 1\end{pmatrix} \quad (2)$$

Where W=(Fmax), ${}^{t}W$=transpose of W

When the scaling factors of each component is calculated, the absolute contribution of each component is estimated by the equation: $({}^{t}W) * (\alpha\ 1\text{-}6)$

Absolute intensity of spectral loading (Em) of each component is calculated by this equation: $[(1/MaxEm)*(Em)]/(\alpha\ 1\text{-}6)$

The absolute contribution of components multiplying the absolute intensity of spectral loading of the components to produce the same intensities as the original samples.

The worksheet presents the arrangement for calculating the scaling factors for each component

Silt_Scaling factor				W_Silt	1	2	3	4	5	6	7
alfa1	0.00011514			Fmax1	1205.16	914.74	3472.32	807.83	4404.27	3641.92	1372.02
alfa2	0.000104058			Fmax2	4		22	1811.65	3625.26	2575.42	4285.43
alfa3	0.0010452			Fmax3	110.85	16.07	24.12	34.58	10.86	38.31	26.63
alfa4	0.000880016			Fmax4	307.11	115.18	79.41	69.54	74.68	197.00	391.61
alfa5	0.000586707			Fmax5	37.83	64.20	81.94	93.66	86.44	132.06	74.32
alfa6	0.00025988			Fmax6	0.00	1588.77	283.22	2297.69	40.94	78.31	0.00
	$(W\ {}^{t}W)^{-1}\ W$*unity										
				$(W\ {}^{t}W)^{-1}\ W$	-1.01E-05	-5.33779E-06	2.1282E-06	-1.98382E-06	6.50017E-06	6.15344E-06	-7.99975E-06
					1.98E-05	8.53313E-06	8.78791E-06	7.97179E-07	5.3779E-06	1.31191E-06	1.59406E-05
					1.25E-05	9.16251E-06	3.38691E-06	1.34753E-05	-4.49783E-06	-1.3622E-05	-1.64618E-05
					-2.56E-06	-1.77973E-05	-2.99604E-05	-2.34503E-05	-2.92081E-05	-1.17925E-05	1.57507E-05
					-3.4E-05	-3.90798E-06	2.04679E-06	1.11985E-05	3.96064E-06	1.02397E-05	-2.72823E-05
					-1.25E-05	4.96226E-05	8.68604E-07	7.8685E-05	-7.15536E-06	-3.76479E-06	-1.20491E-05

${}^{t}W$_Silt	Fmax1	Fmax2	Fmax3	Fmax4	Fmax5	Fmax6	unity	$W\ {}^{t}W$			
1	1205.163185	4740.013	110.849	307.1144	37.83014	0	1		713892419.7	493999299.9	44061971.54
2	914.7307006	3967.116	16.07416	115.1822	64.20485	1588.774186	1		493999299.9	562524462.9	33448185.44
3	347.1041025	1811.652	34.57723	69.53612	81.94117	283.2234076	1		44061971.54	33448185.44	11687409.74
4	807.8299562	1811.652	34.57723	69.53612	93.65735	2297.690551	1		88298679.23	78243119.3	13906427.86
5	4404.271705	3625.263	10.86139	74.67692	86.44186	40.94335614	1		37181810.49	32879581.32	5487058.416
6	3641.923735	2575.422	38.31367	197.0005	132.0584	78.30943861	1		36738401.94	42690784.82	2573509.754
7	1372.021892	4285.435	26.63047	391.6114	74.3196	0	1				
8	5731.484467	2987.354	0	0	104.4797	57.47476393	1				
9	3198.885232	1945.303	13.65458	140.5766	77.09193	947.2573495	1				
10	4868.640817	1321.966	32.92367	211.3096	33.80236	67.30722812	1				
11	2716.59588	3454.016	3.981817	329.6007	94.69674	111.6826366	1				
12	2739.639436	1465.293	159.9813	290.3891	92.7091	221.0411948	1	$(W\ tW)^{-1}$			
13	930.6987194	1295.019	50.37027	246.9537	70.66414	1677.133468	1		3.93879E-09	-2.90576E-09	-3.5755E-09
14	4679.050968	1993.589	55.47653	193.0523	41.27851	68.60210857	1		-2.90576E-09	5.21191E-09	4.93417E-09
15	1717.217094	1577.37	55.10948	104.6025	76.52925	1654.538078	1		-3.5755E-09	4.93417E-09	2.05997E-07
16	1418.382616	3000.686	35.12403	216.6351	90.92135	827.1703226	1		-1.87086E-09	-5.99946E-09	-9.2905E-08
17	1765.448891	3602.886	96.04193	239.7059	38.3382	52.69265648	1		-1.6625E-09	-2.55563E-09	-2.42776E-08
18	751.1669294	0	54.27734	114.7999	41.86524	2803.259113	1		2.21075E-10	-2.52937E-09	3.93259E-09
19	526.3910304	1138.635	41.3979	162.6342	83.11669	2360.921185	1				
20	3213.209343	1401.369	134.8958	241.2489	53.46601	82.16525978	1				
21	1650.909949	1474.59	68.89866	470.54	149.4413	117.688936	1				

W: Scores (Fmax)

^{t}W: Scores (Fmax)

Step 5: Compare the RSS result of different end-member models

The worksheet presents the result of actual scores and intensities of EM

The absolute contribution of components multiplying the absolute intensity of spectral loading of the components to produce the same intensities as the original samples.

Absolute Scores (Fmax)

Absolute Spectra loadings (Em)

tW*alfa1..6	Silt_Cont	New Age	Fmax1_Tak	Fmax2_Gobi	Fmax3_Diatomaceous	Fmax4_JP	Fmax5_Opal-CT	Fmax6_Ordos	Silt_6M1E8_1	score-1_Silt6M1E8_1	F/alfa1...6	Silt_2θ(°)	Em1_Tak	Em2_Gobi	Em3_Diatomaceous	Em4_JP	Em5_Opal-CT	Em6_Ordos
	1	0.00	0.1361	0.4976	0.1147	0.2667	0.0243	0.0000	1.040	0.0395		2.02	805	744	959	1135	1694	809
	2	0.03	0.2337	0.3218	0.0167	0.0691	0.0370	0.3151	0.993	-0.0067		2.04	785	681	916	1107	1657	730
	3	0.07	0.4203	0.4052	0.0252	0.0631	0.0499	0.0556	1.019	0.0192		2.06	711	669	866	1057	1588	735
	4	0.09	0.2797	0.1900	0.0358	0.0152	0.0536	0.4566	1.031	0.0311		2.08	677	624	831	1003	1511	670
	5	0.13	0.5071	0.3797	0.0114	0.0648	0.0529	0.0070	1.023	0.0229		2.1	662	535	762	977	1507	674
	6	0.19	0.4221	0.2708	0.0398	0.1693	0.0808	0.0158	0.999	-0.0013		2.12	617	571	751	915	1425	607
	7	0.24	0.1543	0.4511	0.0274	0.3408	0.0463	0.0000	1.020	0.0199		2.14	582	475	709	881	1410	573
	8	0.30	0.6609	0.3125	0.0000	0.0000	0.0638	0.0096	1.047	0.0468		2.16	555	483	657	850	1328	547
	9	0.38	0.4422	0.2043	0.0141	0.1066	0.0456	0.1874	1.000	0.0003		2.18	505	444	630	834	1251	557
	10	0.41	0.5605	0.1389	0.0339	0.1897	0.0205	0.0125	0.956	-0.0440		2.2	483	424	610	780	1251	487
	11	0.46	0.3176	0.3637	0.0040	0.2861	0.0581	0.0215	1.051	0.0511		2.22	455	387	573	751	1226	479
	12	0.50	0.3296	0.1541	0.1655	0.2492	0.0569	0.0473	1.003	0.0026		2.24	440	352	549	751	1098	440
	13	0.57	0.2414	0.1368	0.0519	0.1846	0.0407	0.3338	0.989	-0.0107		2.26	430	350	540	690	1149	419
	14	0.64	0.5393	0.2090	0.0573	0.1722	0.0252	0.0134	1.016	0.0162		2.28	396	347	507	680	1119	398
	15	0.69	0.3309	0.1654	0.0570	0.0598	0.0442	0.3292	0.987	-0.0135		2.3	394	316	463	675	1055	360
	16	0.74	0.2285	0.3155	0.0363	0.1717	0.0547	0.1646	0.971	-0.0287		2.32	385	307	466	662	1033	355
	17	0.78	0.2048	0.3779	0.0993	0.2077	0.0241	0.0118	0.926	-0.0743		2.34	373	280	448	627	1057	356
	18	0.84	0.3136	0.0000	0.0559	0.0497	0.0209	0.5573	0.997	-0.0025		2.36	343	312	440	623	1001	370
	19	0.87	0.2517	0.1200	0.0427	0.0969	0.0471	0.4695	1.028	0.0279		2.38	352	282	421	623	989	341
	20	0.92	0.3726	0.1470	0.1395	0.2112	0.0330	0.0187	0.922	-0.0781		2.4	338	292	418	608	963	371
	21	0.99	0.1953	0.1574	0.0711	0.4070	0.0918	0.0253	0.948	-0.0521		2.42	347	258	406	601	952	320
	22	1.02	0.4243	0.3072	0.0048	0.1802	0.0642	0.0193	1.000	0.0000		2.44	329	271	414	580	946	348
	23	1.11	0.4492	0.3845	0.0000	0.0827	0.0615	0.0389	1.017	0.0168		2.46	332	257	398	581	922	334
	24	1.16	0.1343	0.1910	0.3072	0.3376	0.0621	0.0202	1.052	0.0523		2.48	316	262	402	585	884	324
	25	1.21	0.4175	0.2206	0.0747	0.2274	0.0492	0.0180	1.007	0.0074		2.5	320	251	369	568	921	347

(score – 1)

The worksheet presents the intensities of samples which calculated from models

Absolute Scores (Fmax) ✕ **Absolute Spectra loadings (Em)** = **actual intensity obtained from PARAFAC**

Silt_2θ(°)	1	2	3	4	5	6	7	8	9	10	11	12
2.02	920	819	837	848	841	876	925	845	846	836	938	924
2.04	873	766	795	792	803	841	882	810	805	808	898	889
2.06	837	740	752	766	754	792	844	754	762	752	852	839
2.08	790	691	709	713	713	750	798	714	717	714	806	796
2.1	729	657	664	691	669	713	744	676	690	686	761	760
2.12	722	630	649	650	652	687	730	653	655	651	737	727
2.14	655	577	590	604	595	637	668	599	609	610	680	683
2.16	640	560	574	581	578	616	653	580	587	587	661	654
2.18	605	535	533	560	534	576	618	531	555	549	624	621
2.2	575	498	508	517	511	550	587	510	521	521	593	591
2.22	541	474	477	496	480	521	554	479	496	494	560	561
2.24	516	443	450	461	454	496	532	452	470	477	537	540
2.26	498	431	442	450	446	484	510	447	457	460	517	521
2.28	484	413	422	427	425	463	498	422	434	437	501	499
2.3	461	388	403	399	409	447	479	408	417	427	484	480
2.32	452	380	394	392	399	438	468	398	408	419	473	473
2.34	426	366	376	384	381	420	443	382	394	401	450	454

actual intensity obtained from PARAFAC − **original samples' intensity 1425** = **Residuals sum of squares (RSS)**

The followings show the example of RSS result by applying a stricter convergence criterion of a minimum tolerance from 1 × 10−2 to 1 × 10−8 with nonnegativity constrained for the 6 endmembers model.

Silt_6M_IE2_Residue

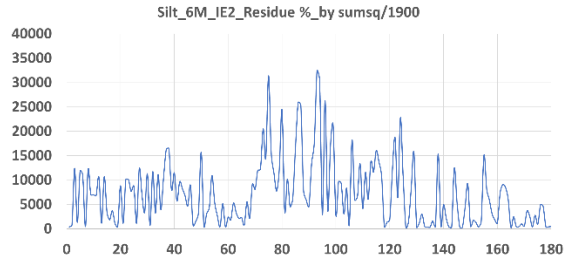

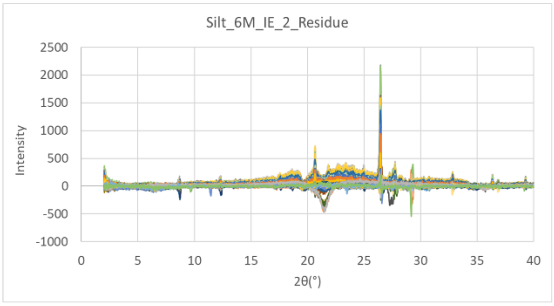

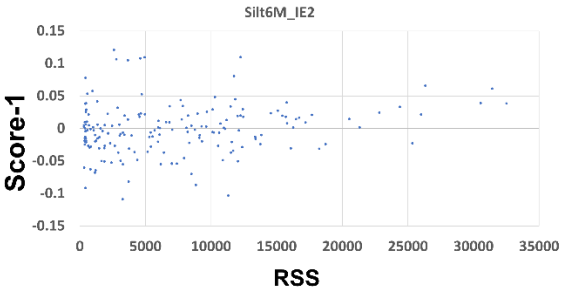

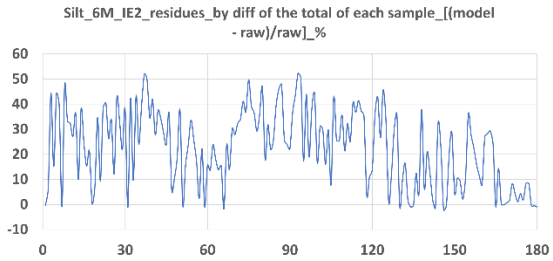

Silt_6M_IE4_Residue

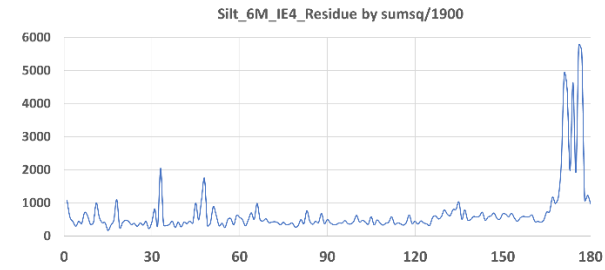

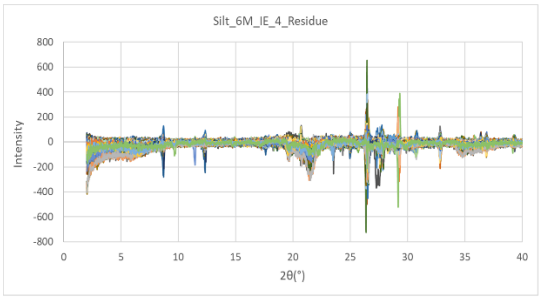

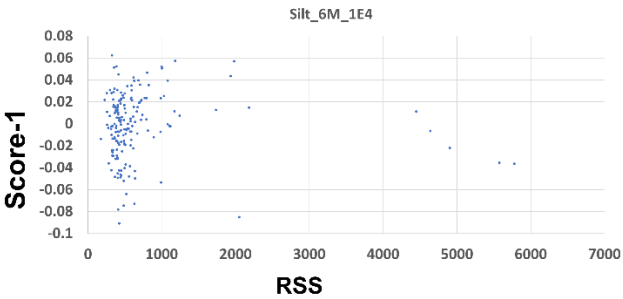

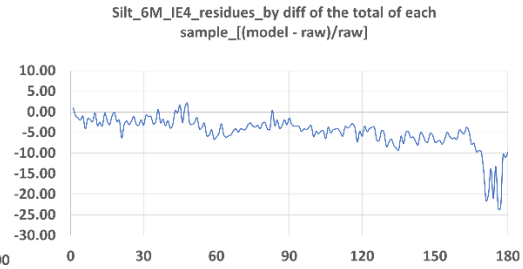

Silt_6M_IE6_Residue

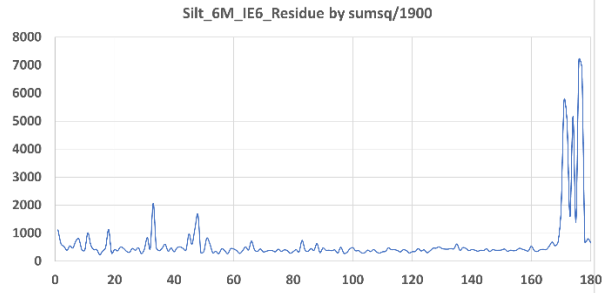

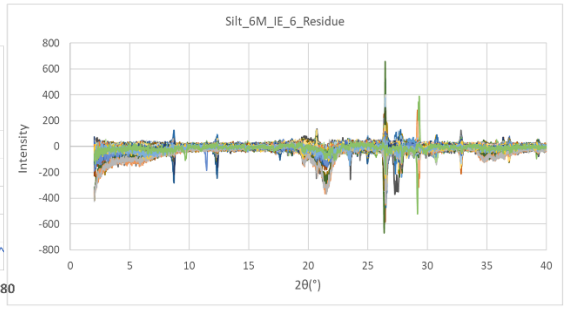

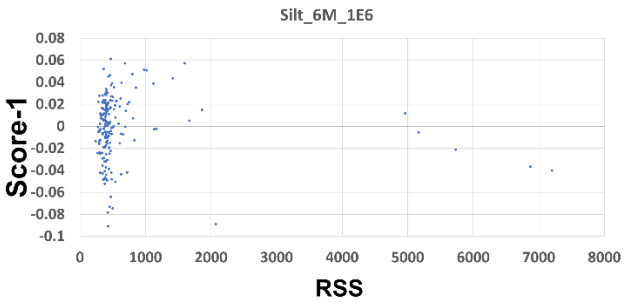

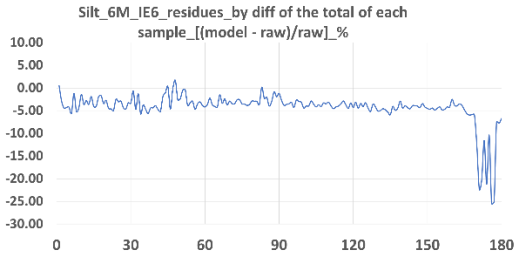

Silt_6M_IE8_Residue